# Rational Control of Hydrothermal Nanowire Synthesis and its Applications

by

JAEBUM JOO

B.S., Materials Science and Engineering
Seoul National University, Korea (2004)



SUBMITTED TO THE DEPARTMENT OF MATERIALS SCIENCE AND EINGINEERING
IN PARTIAL FULFILLMENT OF THE REQUIREMENTS FOR THE DEGREE OF

DOCTOR OF PHILOSOPHY
AT THE
MASSACHUSETTS INSTITUTE OF TECHNOLOGY



JUNE 2010



Signature of Author.....
Jaebum Joo
Department of Materials Science and Engineering
May 03, 2010

Certified by.....
Joseph M. Jacobson
Associate Professor of Media Arts and Sciences
Thesis Supervisor

Accepted by.....
Christine Ortiz
Associate Professor of Materials Science and Engineering
Chair, Departmental Committee on Graduate Studies

# Rational Control of Hydrothermal Nanowire Synthesis and its Applications

by

Jaebum Joo

Submitted to the Department of Materials Science and Engineering on May 03, 2010
In partial fulfillment of the requirements for the degree of
Doctor of Philosophy in Materials Science and Engineering

## Abstract

Hydrothermal nanowire synthesis is a rapidly emerging nanowire discipline that enables low temperature growth and batch process. It has a major impact on the development of novel energy conversion devices, high density electronics, and optical devices. However, detailed growth mechanism is still in early stage of its development. This thesis presents the fundamental understanding of controlled zinc oxide nanowire synthesis in a hydrothermal system based on thermodynamic / kinetic analysis of heterogeneous chemical reactions.

Governing parameters of hydrothermal growth were evaluated with experimental growth rates and calculated solubility plots. Supersaturation was shown to be a key parameter for the hydrothermal nanowire synthesis. Morphology control of the nanowire synthesis was tested with various additional cations during synthesis. Changes in morphology and aspect ratio with different cations were explained by electrostatic competing ion model. Based on experimental results and complex ion charge distribution, the growth direction was biased via electrostatic competition from cation-complexes that adsorb to the crystal in a face-specific manner, thereby reducing zinc ion-complex adsorption and suppressing growth along that face. Dynamic control of nanowire synthesis was investigated under microfluidic environment with continuous flow. Microfluidic growth conditions were analyzed with the parametric experiments and finite element modeling. Nanowire growth under complex geometry was also evaluated.

This rational control of hydrothermal nanowire synthesis was applied to fabricate high efficiency alternative current electroluminescent devices, in-situ fabricated light emitting diodes, photovoltaic devices, and field emission devices.

Thesis Supervisor: Joseph M. Jacobson

Title: Associate Professor of Media Arts and Sciences

# Table of contents

# Figures and Tables

# Acknowledgments

I would like to thank so many people around me for their support through my graduate studies.

First of all, I would like to thank for my parents who provided a strong foundation of love and support for me. I was able to study this far because of you.

I am really grateful to meet my advisor, Prof. Joseph Jacobson, for providing such a creative ideas and lab environment, so I could work on many different topics of research through my Ph.D. I appreciate his insights and now I learned how to pursue a scientific research more effectively.

I also want to thank my thesis committee members, Prof. Carl Thompson and Prof. Silvija Gradecak, for their guidance during my research. They provided me practical suggestions and feedback for my thesis work.

Molecular Machines research group have made my life at MIT to be really exciting. I appreciate all the members I met in the group who taught me what I can do now; David Mosley for general lab work and mentorship, Peter Carr for biology knowledge and interesting ideas, Vikrant Agnihotri for the lithography process and patterning research, SangJun Moon for mechanical engineering knowledge and mentorship, Chris Emig for ideas and software programming, David Kong for microfluidics and lithography, Manu Prakash for simulations and device fabrications. I specially thank Brian Chow for being my mentor, collaborator, and friend who taught me many different aspects of Ph.D. research. I also thank Kimin Jun who always has been in the lab with me from day and night, helping technical issues, and discussed new ideas.

Without Media Lab staff members, my research would not have been successful. I thank Joseph Murphy, Nicole Degnan, Susan Botari, and Sherry Lassiter for following up my every bit of purchase orders, travel, and other administrative issues. John Difrancesco and Tom Lutz taught me how to use several mechanical tools in the machine shop. Kevin Davis made our lab more secure and safe.

I thank for MIT DMSE KGSA members who made my early MIT life more comfortable and easier. I was able to make so many good friends at there, and they have been mentors in every aspect of my research.

I am grateful to meet MTL staff members and CMSE staff members who were willing to spend their time to help fabricating and improving my devices. Especially, I thank for Kurt borderick, Libby Shaw, and Yong Zhang who gave me a handful of technical aids and advice.

People from other Labs helped me many parts of my graduate studies too. I thank for Jennifer Hsieh, Jifa Qi, August Dorn, Hyunil Byun, Sungkeun Lim, Yongjin Sung, Joonah Yoon, JungGon Son, Yoonseog Lee, Keywon Chung, Woochul Jung, and Jungwoo Joh for their time, knowledge, and tool sharing.

Work at Samsung Electronics LCD Research and Development Center for the summer was really a valuable experience for me. From several researchers, I learned many aspects of display technology and frontier research in the real world. I was also

able to see how industry has different point of view from academia.

People I met during architecture class opened my aspects of interest into arts. I always had a dream to be an industrial designer when I was young, and the class taught me what I can contribute to their fields. I was fortunate to meet Prof. Larry Sass who was kind enough to take me with a materials science background to his intensive class, and guided me to work on several architectural prototypes. Working day and night with classmates Kalaya Kovidvisith, Daniel Cardoso, Taro Narahara, Dennis Michaud, and Kenfield Griffith was a really great experience.

I also thank for the people whom I met during Media Lab workshop in Seoul. I am really grateful to be a part of the workshop members who stayed overnight for the preparation, and really made the workshop successful. During preparation and workshop, I learned how to brainstorm in a creative way, work with sponsors for fund raising, and lead people with different ages.

People at First Korean Church in Cambridge supported me to be spiritually strong. Without their support, I would not have gone through this long journey of my studies.

The last and most, I thank for my wife, Janet Cheong, who always have been with me. She supported me in every day of my life at MIT. I was lucky to meet her at Boston, and being with her. I also thank her for guiding me into Christian. She always made me happy. Thank you.

Funding sources: The Korea Foundation for Advanced Studies, The Center for Bits and Atoms.

# Chapter 1 : Introduction

## 1.1. Motivation

Nanowires are of great interest because of their properties such as quantum confinement effect and high surface to volume ratio that can be utilized for several applications. Conventional gas-phase reaction techniques for nanowire growth normally require high temperature, thereby limiting integration with other materials and devices. As an alternative approach, nanowires can be grown at low temperature in supersaturated solutions with different reactive ions and complexing agents, called hydrothermal or solvothermal nanowire synthesis depending on solutions used. Previously, semiconductor nanowires and nanobelts composed of zinc oxide, zinc sulfide, and cadmium hydroxide have been synthesized on substrates at low temperature in bulk solutions [1-3] .

Because of low temperature growth condition and batch process capability, the hydrothermal nanowire synthesis has been a rapidly emerging nanowire discipline that has a major impact on the development of novel energy conversion devices, high density electronics, and optical devices [4] . For liquid phase reactions, growth kinetics and reaction conditions govern the nano-scale structures. However, a detailed growth mechanism for this hydrothermal system is still in early stage of its development.

The goal of this thesis is to explore the mechanism of hydrothermal inorganic nanowire synthesis, especially zinc oxide (ZnO), based on thermodynamic and kinetic analysis. Utilizing the relationship between the ion solubility and heterogeneous nucleation and growth, ZnO nanowire synthesis will be evaluated. This fundamental parametric synthesis study is applied toward the fabrication of optimal morphology of nanowires that can be used as field emission devices, high efficiency electroluminescent devices, and photovoltaic cells.

## 1.2. Overview of Thesis

Chapter 2 will begin with background information of ZnO materials and its properties. Next, different methods of nanowire synthesis will be discussed. Last, detailed thermodynamic description of heterogeneous nucleation and growth will be given, followed by microfluidic nanostructure synthesis.

Chapter 3 discusses the relationship between the ion solubility and heterogeneous nucleation/ growth, and parametric study ZnO nanowire synthesis. Calculated solubility plot and relative supersaturation at specific condition will be compared with experimental results of nanowire synthesis.

Chapter 4 evaluates the mechanism of tunable morphology of ZnO in hydrothermal system with cation addition. Extended from chapter 3, solubility plot with multiple ions and complex ion distributions will be calculated. The growth and morphology behavior with additional cations will be analyzed with the calculated charge distribution. Using several analytic methods, suggested electrostatic competing ion model will be discussed.

Chapter 5 covers the spatial control of nanowire synthesis with block copolymer self assembly. Block copolymer will be used for making templates for the nanowire synthesis in a hydrothermal condition. Detailed self assembly process will be discussed, followed by ZnO nanowire growth with the templates for possible applications.

Chapter 6 will discuss Microfluidic controlled ZnO nanowire synthesis. Within the confined fluidic channel, hydrothermal ZnO nanowire growth will be evaluated in a microfluidic system. Coupled chemical reaction and fluid dynamics will be discussed in a simple geometry. Nanowire synthesis in a complex geometry will also be investigated.

Chapter 7 will discuss several applications using the rational control of hydrothermal nanowire synthesis. First, field emission device with different morphologies will be tested for extraction efficiency change. Next, novel alternative current electroluminescent devices with nanowire embedded structure will be demonstrated. ZnO nanowire light emitting diode with Metal / insulator / semiconductor structure will also be discussed. Finally, possible applications for photovoltaic system will be mentioned.

Chapter 8 covers alternative novel nanoscale fabrication techniques using top down approaches related to position control of nanowire synthesis. Critical energy electron beam lithography will be demonstrated for high resolution e-beam patterning on non conducting substrates, and its mechanism will be discussed. Nanoparticle assembly with electrostatic deposition using electron beam will also be discussed.

Chapter 9 contains concluding remarks, suggestions for improvements of the devices and proposal for future research directions.

Chapter 10 covers Matlab codes and chemical reaction constants used for thermodynamic calculation of solubility plot and complex ion distribution.

# Chapter 2 : Background

## 2.1. ZnO and its nanostructures

Zinc Oxide (ZnO) has been of great interest because of its optical and electrical properties [5]. Direct wide band gap (~3.3eV at 300K) enables ZnO as a possible candidate for the replacement of GaN (~3.4eV at 300K) which is currently used for green, blue-ultraviolet, and white light emitting diode (LED). Wide band gap above visible wavelength also make ZnO to be useful as a transparent conducting oxide or transparent thin film transistors by substitutional doping by Indium or other charge carriers [6]. The large exciton binding energy (60meV) enables near band edge excitonic emission possible at or near room temperature. Piezoelectric properties of ZnO are useful for sensors and energy harvesting devices.

In addition to its bulk properties, ZnO nanostructure research showed interesting properties recently. Several practical applications are demonstrated since Vayssieres et al. [1, 7] successfully synthesized vertically aligned ZnO nanowires on the substrates at low temperature (~90C) by hydrothermal process. By using the high aspect ratio of ZnO nanowires, Lee et al. [8] showed enhanced field emission properties. Yang and coworkers used the high surface area of ZnO nanowires as a charge transport layer for Dye Sensitized Solar Cell [9], showing conversion efficiency of 1.5%, double that of typical ZnO Nanoparticle based solar cells. Wang et al. studied piezoelectric properties of ZnO nanowires [10] and created several energy harvesting applications. Konenkamp and coworkers made flexible ultraviolet LED using low temperature synthesized ZnO nanowires as a n-type active layers [11].

| | ZnO | GaN |
|---|---|---|
| Band gap (eV) | 3.3 | 3.4 |
| $\mu_e$ ($cm^2$/Vsec) | 200 | 220 |
| $\mu_h$ ($cm^2$/Vsec) | 5 ~ 50 | 10 |
| $m_e$ | 0.24 $m_o$ | 0.27 $m_o$ |
| $m_h$ | 0.59 $m_o$ | 0.8 $m_o$ |
| Exciton binding E (meV) | 60 | 28 |

Table 2.1. Comparison of ZnO and GaN electrical and optical properties.

(a)

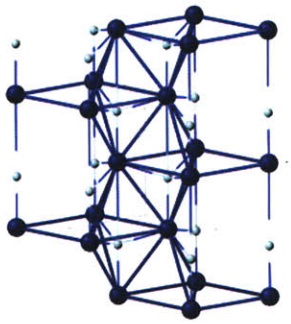

(b)

| Unit cell | ZnO |
|---|---|
| Space group | P $6_3$mc |
| a ($\dot{A}$) | 3.24992 |
| c ($\dot{A}$) | 5.20658 |
| V ($\dot{A}^3$) | 47.625 |
| $\rho$ | 5.675 g/$cm^3$ |

Figure 2.1. ZnO wurtzite structures (a) and its unit cell parameters (b).

## 2.2. Nanowire synthesis

Nanowire Synthesis process can be divided into two different methods by initial material phases; Vapor-Liquid-Solid and hydrothermal synthesis.

### 2.2.1. Vapor Liquid Solid Nanowire synthesis

The Vapor-Liquid-Solid (VLS) synthesis was first described by Wagner and Ellis in 1964 [12]. They synthesized silicon nanowires using gold as a catalyst. Gold forms liquid droplets when the silicon substrate is heated above its Si-Au eutectic temperature at ~360C. When silicon precursor gases ($SiH_4$ or $SiCl_4$) are introduced into the system,

the gold catalyzes the breakdown of precursors, and starts to saturate silicon into gold. When the droplet starts to supersaturate, the silicon starts to precipitate at the interface between the silicon substrate and gold, which is energetically favorable. Since the interface is defined by the area of gold droplets, precipitation only occurs at the local region, forming high aspect nanowires as shown in Figure 2.2. This VLS process has been used for several other nanowire synthesis including gallium nitride, gallium arsenide, indium phosphide, and others. However, this method has major disadvantages of being high temperature, thereby limiting integration of other materials and device processing.

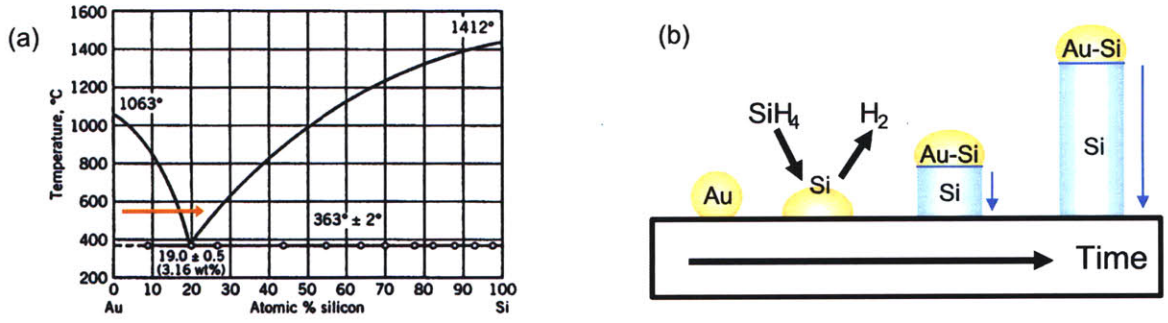


Figure 2.2. Au-Si eutectic phase diagram (a) and a schematic of Vapor-Liquid-Solid nanowire synthesis process. Once liquid Au droplet forms, supersaturated Si precipitates at the interface, forming s nanowire with a diameter defined by the Au droplet size.

### 2.2.2. Hydrothermal Nanowire Synthesis

As an alternative approach, nanowires can be grown at low temperature in supersaturated solutions with different cations, anions, and complexing agents. This is called hydrothermal synthesis. The process is similar to the chemical bath deposition, except that it produces nanowires instead of thin films on the substrates. In case of ZnO nanowires, a substrate is coated with a seed layer, which is generally sol-gel processed

ZnO thin film or sputtered amorphous ZnO. This substrate is introduced in to a water solution supersaturated with zinc salts, amines (complexing agents), and other ions. When the solution is heated up at low temperature (50~90C), micro/nano structured ZnO is formed on the seed layer coated substrates by heterogeneous nucleation and growth from the hydrolysis of zinc salts as shown in Figure 2.3. This low temperature hydrothermal synthesis enables low cost, large area batch process compatible for further integration process. Semiconductor nanowires and nanobelts composed of zinc oxide, zinc sulfide, and cadmium hydroxide have been synthesized on the substrate using hydrothermal mechanism [1-3]. Interestingly, general knowledge of nucleation and growth in supersaturation solution has been known for a while, governing parameters for the hydrothermal nanowire reaction is still not clear, because a detailed synthesis mechanism does not exist yet.

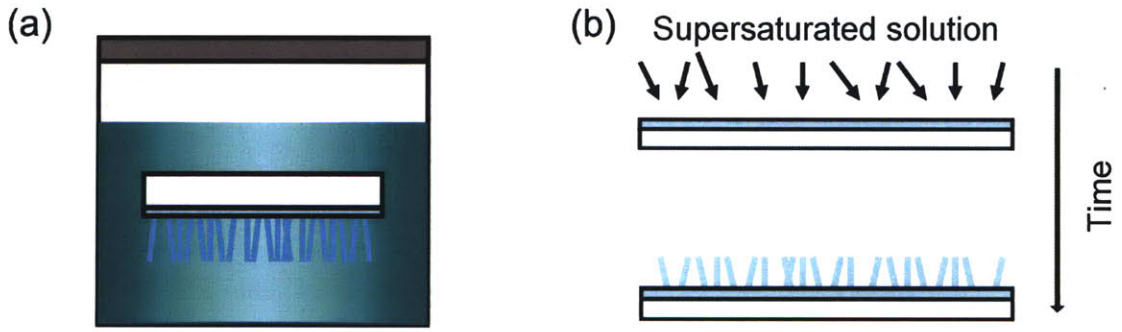


Figure 2.3. A schematic of Hydrothermal Nanowire Synthesis reactor in a bulk solution (a) and a time dependent nanowire growth on the seed layer coated substrate driven by heterogeneous growth.

## 2.3. Heterogeneous Nucleation and growth

Supersaturated solutions form unstable clusters that can form precipitates either on the substrate or in the solutions. If the clusters form into large size enough, it can

precipitate into solid phase, overcoming the new surface energy by free energy change of liquid-solid phase. After this nucleation process started, several other nuclei also form at constant rate.

Heterogeneous nucleation from liquid phase can be simplified by spherical cap shape, as shown in figure 2.4. Since interfacial energies of nuclei must balance at equilibrium, which gives the following Young's Equation

$$\gamma_{ML} = \gamma_{SM} + \gamma_{SL}\cos\theta \tag{1}$$

where $\theta$ is contact angle between the solid and the mould and $\gamma_{ML}$, $\gamma_{SM}$, and $\gamma_{SL}$ are the mould-liquid, solid-mould, and solid-liquid interface energies.

The formation of the nuclei with a spherical cap will be associated with an excess free energy given by

$$\Delta G_{het} = \left\{-\frac{4}{3}\pi r^3 \Delta G_V + 4\pi r^2 \gamma_{SL}\right\} S(\theta) \tag{2}$$

where r is the radius of the full sphere and $\Delta G_V$ is the change in free energy per unit volume that depends on the supersaturation of the solution. The geometry factor is given by

$$S(\theta) = (2+\cos\theta)(1-\cos\theta)^2/4 \tag{3}$$

Minimizing $\Delta G_{het}$ with respect to r gives the critical nucleus size and the energy barrier to proceed to nucleation and growth,

$$r^* = \frac{2\gamma_{SL}}{\Delta G_V},\ \Delta G_{het}{}^* = \frac{16\pi\gamma_{SL}^3}{3\Delta G_V^2}\cdot S(\theta) \tag{4}$$

As shown from the above, the activation energy barrier for heterogeneous nucleation is smaller than $\Delta G^*_{\text{hom}}$ by the geometry factor.

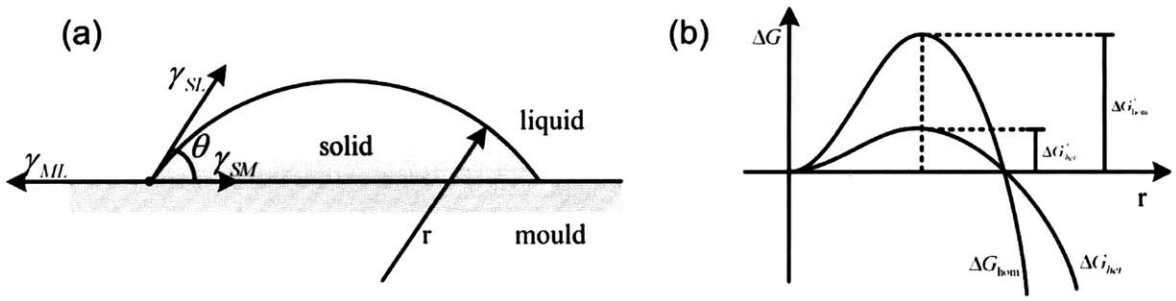


Figure 2.4. (a) Heterogeneous nucleation of spherical solid cap on a flat mould surface. Three interface energies are represented for equilibrium shape formation. (b) Free energy of solid nucleus for homogeneous and heterogeneous nucleation. Activation barrier for heterogeneous process is smaller than homogenous process by a geometry factor defined by the shape of the heterogeneous system.

In case of atomically rough or diffuse interfaces, dominantly metallic systems, atoms migrate by a continuous growth process. Assuming the reaction from liquid to solid follows first order reaction, and the precipitation is a thermally activated process, the reaction constant is given as

$$f = f^0 \exp(-\frac{\Delta G^*}{RT})\left[1 - \exp(\frac{\Delta G_r}{RT})\right] \tag{5}$$

where $f^0$ is attempt frequency, $\Delta G^*$ is activation barrier energy, and $\Delta G_r$ is free energy change between two phase.

The growth rate of solid from liquid solid interface is given by

$$v = s \cdot f \cdot \eta = s \cdot \eta \cdot f^0 \exp(-\frac{\Delta G^*}{RT})\left[1 - \exp(\frac{\Delta G_r}{RT})\right] \tag{6}$$

where s is the fraction of sites available for the attachment of new atoms, and $\eta$ is the distance the interface moves when one atom is attached. As seen from equation 6, growth rate is proportional to $\Delta G_r$, which is supersaturation dependent.

In case of flat or sharply defined interfaces, normally non metals, atoms migrate by a lateral growth process involving ledges. In case of low supersaturation, the rate

would follow a ledge nucleation process, but the growth rate at high saturation condition would be same as continuous growth rate because large ledge nucleation leads to a kinetically rough surface.

## 2.4. Microfluidic synthesis of nanomaterials

A microfluidic device contains channels in a micron scale, normally a few um to mm, which can deliver small amount liquid in and out. It can be considered as a small reaction vessel with the following characteristics. First, the liquid can be rapidly accessible from the outside by external mechanical or pressure pump. Second, the fluid can have a laminar flow with reasonable flow velocity without turbulence. In that case, mixing of liquids in multiple channels only happen by lateral diffusion and this character gives high precision control in liquid reaction. Third, small volume of device enables rapid external control of temperature and other parameters of liquids. Several researchers synthesized different nanomaterials using the microfluidic chemical reactors.

Nanocrystals exhibit size dependent electrical and optical properties. To synthesize custom nanocrystals with tight size distribution is a significant challenge for a bulk synthesis process. General bulk synthesis of nanocrystals is controlled by following processes: rapid nucleation by injection of a precursor into the bulk solution at high temperature, growth at a lower temperature with stabilizing surfactants. Several kinetics including rate of injection and mixing make consistent nanocrystal synthesis to be difficult.

Microfluidic system can create rapid change of temperature and reactant concentration, which is desired for nanocrystal synthesis. Alivisatos *et al.* [13-14] successfully demonstrated cadmium selenide (CdSe) nanocrystal synthesis in a

microfluidic device with different reaction time, temperature, and precursor concentrations. Other groups also demonstrated use of a microfluidic reactor for the synthesis of gold, cobalt, silica, cadmium sulfide, and others [15-18].

Microfluidic device can also be used to deposit or etch materials on the surface exposed to the micro channels. Localized crystal nucleation and growth can happen at the interface between two stream laminar flow. For example, calcite crystals can form on the self assembly monolayer $HS(CH_2)_{15}COOH$ treated surface at the interface between two parallel liquids, one with calcium ions and the other with carbonate ions [19]. By flowing gold etchant or electroless silver solution with guided liquid, localized etching of gold and silver coating were demonstrated also [20].

# Chapter 3 : Nanowire synthesis in a bulk system

## 3.1. Introduction

ZnO has been of great interest because of its broad applications such as ultraviolet laser, piezoelectric generator, dye sensitized solar cell, chemical sensor, and others [5, 9-10, 21-24]. Especially, ZnO nanowire structure has high surface to volume ratio and size dependent optical and electrical properties, many effort has been devoted to develop a method to synthesize nanostructures.

One of the most popular methods of ZnO nanowire synthesis is hydrothermal growth developed by Vayssieres et al.[1, 7, 25-26]. Using solutions with zinc nitrate hydrate and monoethanolamine, nanowires were successfully grown on ZnO seeded substrate. This approach has a huge potential to scale up because of low temperature liquid characteristic of the process. Many researchers have worked to find optimal parameters by changing chemical compositions including zinc nitrate concentration, monoethanolamine concentration, temperature, and others, but no perfect governing parameters that explains the growth behavior exist yet [27-28].

In this chapter, we examined the relationship between supersaturation degree and hydrothermal nanowire synthesis in a bulk condition. Given possible chemical reactions of zinc ion complexes in the solution, solubility plot of the system are given. By analyzing experimental data of ZnO nanowire growth with different supersaturation conditions calculated by solubility plot, we successfully found a general relationship between supersaturation and an optimal condition for ZnO nanowire synthesis.

## 3.2. Experiments

In hydrothermal ZnO nanowire synthesis, a seed layer defines heterogeneous nucleation and growth. Therefore, underlying substrate can be any substrates including

Si, glass, quartz, ITO, flexible polymer, and others as long as the material is compatible with chemical solution. For a typical synthesis, a $1cm^2$ Si substrate was cleaned with acetone, IPA, deionized water, and dried under nitrogen.

ZnO seed layer was deposited either by sputtering or sol-gel spin coating. In case of RF sputtering (AJA International), 30 nm ZnO was deposited using 150W power, 20mTorr, 12 sccm Ar with ZnO target. In case of sol-gel spin coating, 0.7 M zinc acetate dihydrate ($Zn(NO_3)_2 \cdot 6H_2O$, >99.0%, Sigma Aldrich) and 0.7 M monoethanolamine ($NH_2CH_2CH_2OH$, >99.0%, Sigma Aldrich) were dissolved in 2-methoxyethanol ($CH_3OCH_2CH_2OH$, >99.9%, Sigma Aldrich), then stirred at 60 C for 30 minutes. The substrate was then spin coated with the solution at 3000 rpm for 40 seconds and heated at 250 C for 10 minutes on a hot plate, and repeated this coating for 3 times.

In growth solution preparation, various concentrations of zinc sulfate heptahydrate ($ZnSO_4 \cdot 7H_2O$, >99.0%, Sigma Aldrich) and ammonium chloride ($NH_4Cl$, >99.5%, Sigma Aldrich) were dissolved in 100 mL deionized solution, then sodium hydroxide (NaOH, Sigma Aldrich) is added to adjust pH (Mettler Toledo,S40-K) to a desired value.

The substrate was flipped by a chemically inert Teflon holder to make sure ZnO seed layer was facing down. This set was immersed into each bath with a closed lid, heated at various temperatures from 40 C to 60 C in a convection oven (Yamato DX400) for a different period time for the nanowire growth. Once the chemical reaction was done, sample was taken out from the bath, washed with DI water thoroughly, and dried under nitrogen.

Synthesized nanowire length and morphology were evaluated by cross sectional

scanning electron microscopy (Philips-FEI XL30 ESEM). Crystalline structure and orientation of the nanowires was identified by X-ray diffractometry (Panalytical X'pert Pro) using CuK$\alpha$ (1.5406Å) radiation. Photoluminescence of ZnO nanowires was measured with Hitachi F-7000 with 325nm excitation by Xe lamp. JEOL 2010F field emission transmission electron microscope (FE-TEM) was used for lattice image and diffraction pattern measurement.

## 3.3. Results and discussion

In hydrothermal synthesis, nanowire growth changes significantly with chemical composition of growth solutions. Since the reaction happens by heterogeneous nucleation growth, supersaturation would be a good indicator how much the driving force would be for the growth. Figure 3.1 Shows solubility plot with different conditions calculated from the possible chemical reactions in solution containing $ZnSO_4$, $NH_4Cl$, and NaOH. X-axis indicates pH (NaOH dependent), y-axis indicates $NH_4Cl$, and z-axis indicates maximum concentration of zinc ions without forming ZnO. Therefore, if any solution concentration defined by xyz position is below the 3D contour plane shown in Figure 3.1(b), no precipitation will occur and nanowire growth will not happen. If prepared solution condition is above the plane, it would be in a supersaturation condition, amount defined by z-axis difference from the point to the plane, and it is possible that this solution can grow nanowires by condensation reaction.

(a)

| Reaction | Log K |
|---|---|
| $Zn^{2+} + OH^- \rightarrow Zn(OH)^+$ | 5.0 |
| $Zn^{2+} + 2OH^- \rightarrow Zn(OH)_2(aq)$ | 11.1 |
| $Zn^{2+} + 3OH^- \rightarrow Zn(OH)_3^-$ | 13.6 |
| $Zn^{2+} + 4OH^- \rightarrow Zn(OH)_4^{2-}$ | 14.8 |
| $Zn^{2+} + NH_3 \rightarrow Zn(NH_3)^{2+}$ | 2.21 |
| $Zn^{2+} + 2NH_3 \rightarrow Zn(NH_3)_2^{2+}$ | 4.5 |
| $Zn^{2+} + 3NH_3 \rightarrow Zn(NH_3)_3^{2+}$ | 6.86 |
| $Zn^{2+} + 4NH_3 \rightarrow Zn(NH_3)_4^{2+}$ | 8.89 |
| $NH_4^+ + OH^- \leftrightarrow NH_3 + H_2O$ | 4.39 |
| $Zn^{2+} + 2OH^- \leftrightarrow ZnO(s) + H_2O$ | 15.52 |

(b)

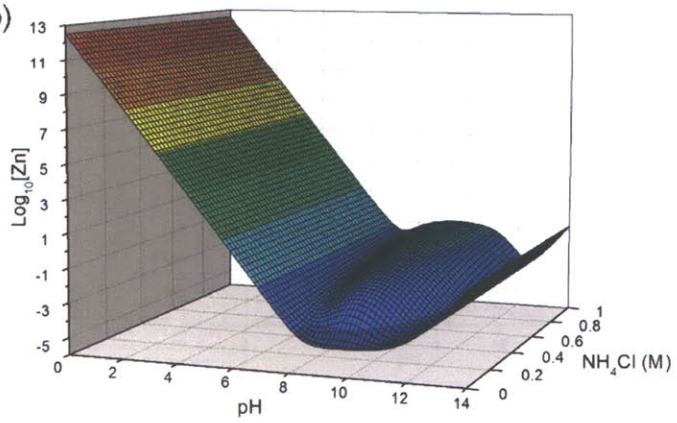


Figure 3.1. Possible chemical reaction in ZnO nanowire bath solution (a) and solubility plot (b) with different pH/NH4Cl concentrations calculated by Matlab code with reaction constants.

Figure 3.2 shows calculated zinc ion complex distribution with different $NH_4Cl$. At low pH, $[OH^-]$ is low, so most of zinc ion complex will remain as $Zn^{2+}$. As pH increases ($[OH^-]$ increases), $Zn^{2+}$ starts to react with hydroxide and forms ZnO, so solubility starts drop. However, increasing pH further will induce $Zn^{2+}$ to form soluble zinc hydroxide complexes (Figure 3.2(a)), thereby increasing solubility again. When $NH_4Cl$ is introduced to the solution, zinc ions can also form soluble zinc amine complexes, raising a solubility at region between pH 8 ~ 12. Figure 3.2(b) shows complex ion distribution at 0.3M $NH_4Cl$ with different pH. At pH 8~12 range, most of zinc ions form $Zn(NH_3)_4^{2+}$ complex, therefore solubility increases.

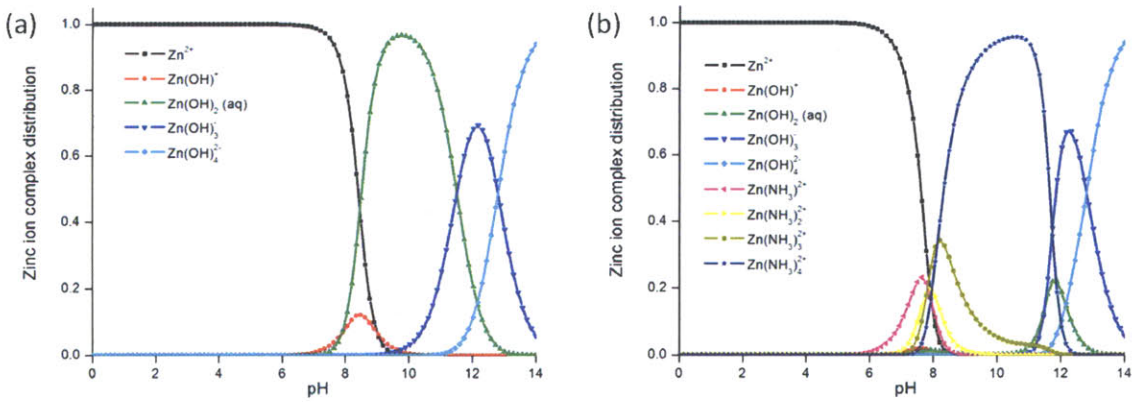


Figure 3.2. Calculated zinc ion complex distribution at different pH with no $NH_4Cl$ (a) and 0.3M $NH_4Cl$ condition.

Nanowire growth was evaluated by cross sectional SEM. Figure 3.3 shows exemplary SEM of time dependent nanowires grown at fixed solution condition. The longer time the substrate was left in the solution, the longer the nanowire grew.

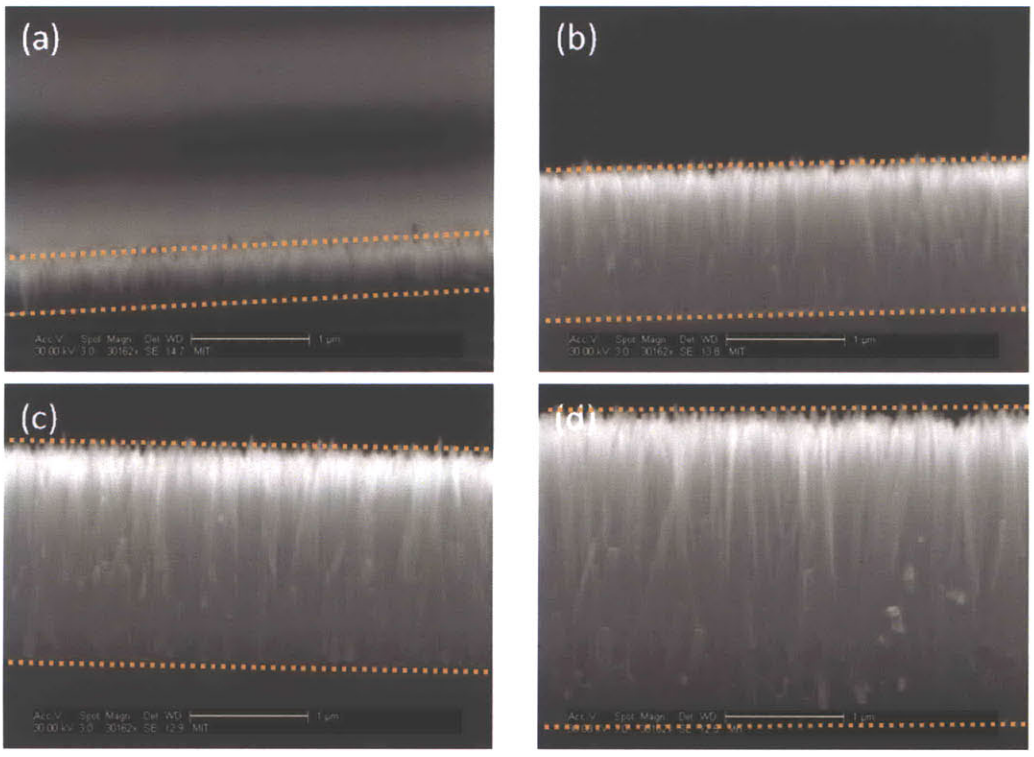


Figure 3.3. SEM cross section of time dependent ZnO nanowires grown in fixed solution condition ($ZnSO_4$ 0.01 M, $NH_4Cl$ 0.3 M, pH 11, 60 C in 100 mL). (a) t= 2 hrs ,(b) t= 4 hrs, (c) t= 6 hrs, (d) t= 8 hrs.

Figure 3.4 shows the growth trend with respect to time. At initial stage (0 ~ 2 hrs), growth was slow because it requires nucleation process at an initial time. At middle stage (2 ~ 15 hrs), heterogeneous growth from the nucleated surface was dominant, so growth was proportional to time. At last stage (15 ~ 30hrs), growth starts to slow down because supersaturated zinc ions are already consumed during active growth at middle stage and real supersaturation concentration decreases. Above this time period, no active growth was observed.

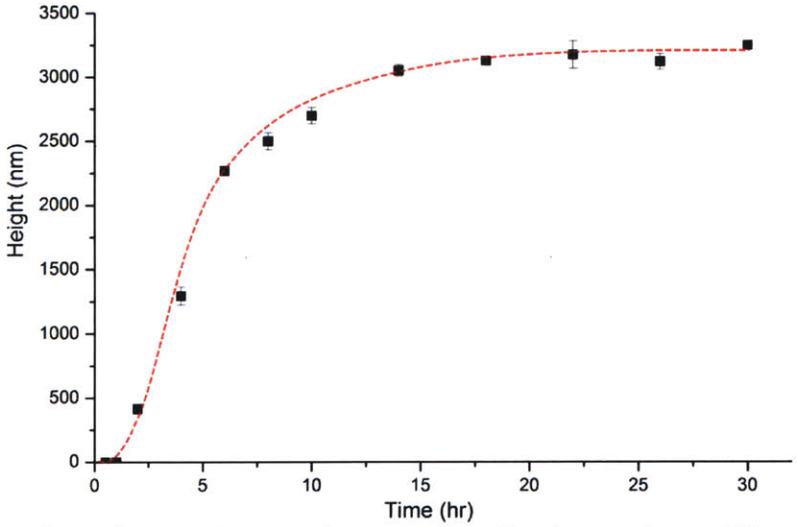


Figure 3.4. Time dependent ZnO nanowire growth at fixed growth condition ($ZnSO_4$ 0.01 M, $NH_4Cl$ 0.3 M, pH 11, 60 C in 100 mL).

pH dependent nanowire growth is shown in Figure 3.5. All other chemical solution parameters ($ZnSO_4$ 0.01M, $NH_4Cl$ 0.3M) were kept same and pH were changed by adding different amount of NaOH. Substrates were introduced at 60 C in 100 mL for 6 hrs. At pH < 10, solution is not in supersaturation condition from the calculated solubility plot. In experiments, there was no nanowire growth observed at this regime. In fact, thin seed layer film got dissolved because the solution was below solubility limit. At 10 < pH <11, nanowire growth increases with pH increase because supersaturation amount increases as pH increases, and growth is proportional to supersaturation amount (driving force). At 11 < pH < 12, the growth was decreased again with pH increase. This happened because of too high supersaturation. At this high pH, supersaturation was too high and ZnO can also form within the solution with homogeneous nucleation and growth in solution itself. The nanowire height decrease indicates that heterogeneous nucleation and growth was slow as it competed with homogeneous nucleation and growth process. During the reaction at 11 < pH < 12, solution color changed from transparent to turbid, indicating homogenous reaction process was active.

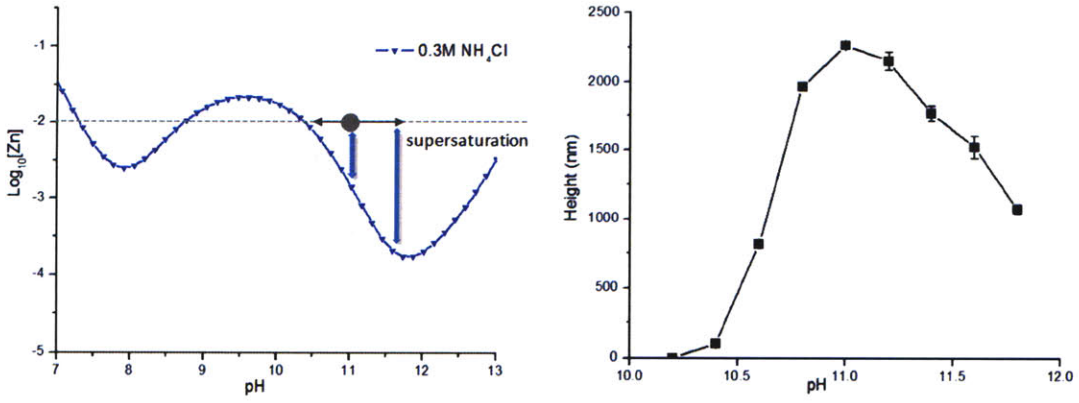


Figure 3.5. pH dependent nanowire growth characteristic. All other parameters were fixed ($ZnSO_4$ 0.01M, $NH_4Cl$ 0.3M, 60 C in 100 mL for 6 hrs) except variable pH. Left graph shows solubility plot and supersaturation amount (↕) at different pH. Right graph shows experimental data of height measurement at different pH.

Similar growth trend was observed at different zinc ion concentration (Figure 3.6). All other chemical solution parameters ($NH_4Cl$ 0.3M, pH 11) were kept same. Substrates were introduced at 60 C in 100 mL for 6 hrs. At $[Zn^{2+}] < 4$ mM, almost no growth was observed. At 4 mM $< [Zn^{2+}] < 10$ mM, heterogeneous nucleation and growth process was dominant. In case of $[Zn^{2+}] > 10$ mM, homogeneous nucleation and growth was competing against heterogeneous process, thereby decreasing nanowire growth on the substrate with higher $[Zn^{2+}]$.

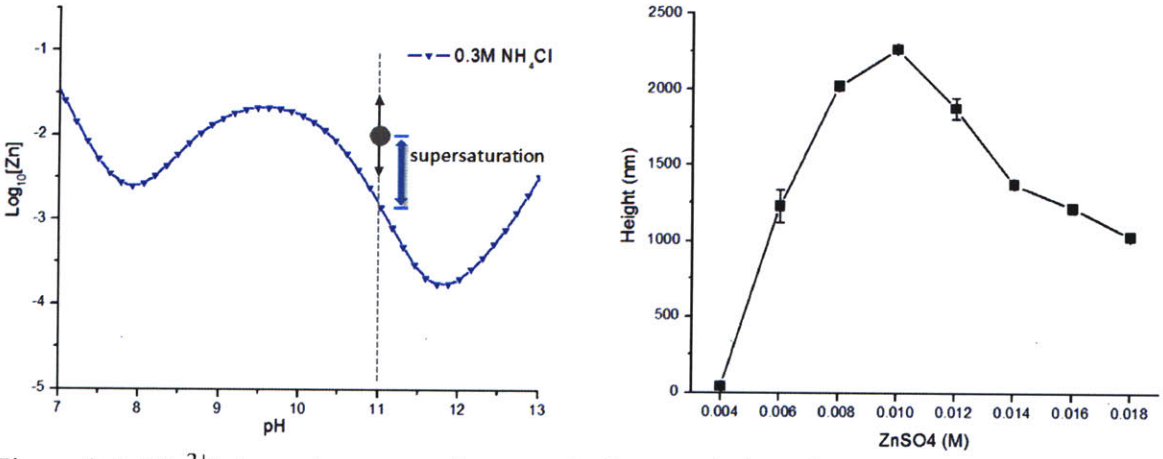


Figure 3.6. $[Zn^{2+}]$ dependent nanowire growth characteristic. All other parameters were fixed ($NH_4Cl$ 0.3M, pH 11, 60 C in 100 mL for 6 hrs) except variable $[Zn^{2+}]$. Left graph shows solubility plot and supersaturation amount (↕) at different $[Zn^{2+}]$. Right graph shows experimental data of height measurement at different $[Zn^{2+}]$.

$NH_4Cl$ dependent nanowire growth is shown in Figure 3.7. All other parameters ($ZnSO_4$ 0.01M, pH 11, 60C in 100 mL for 6 hrs) were kept same. As mentioned previously, zinc ions can form zinc amine complexes around pH ~ 11, thereby increasing solubility limit in $NH_4Cl$ presence. As $[NH_4Cl]$ increases with other parameters kept the same, supersaturation decreases. At 0.3M $< [NH_4Cl] <$ 0.4M, growth decreases with $[NH_4Cl]$ increase (supersaturation decrease), so it would be at heterogeneous growth dominant region. At 0.1M $< [NH_4Cl] <$ 0.3M, growth increases with $[NH_4Cl]$ increase

(supersaturation decrease). In this region, homogenous growth would be a dominant reaction process.

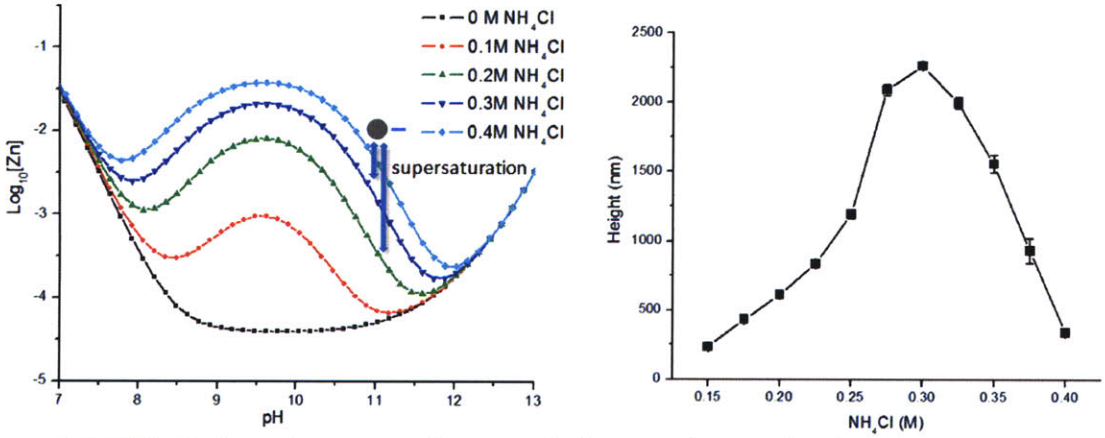


Figure 3.7. $NH_4Cl$ dependent nanowire growth characteristic. All other parameters were fixed ($ZnSO_4$ 0.01 M, pH 11, 60 C in 100 mL for 6 hrs) except variable $NH_4Cl$. Left graph shows solubility plot and supersaturation amount (↕) at different $NH_4Cl$. Right graph shows experimental data of height measurement at different $NH_4Cl$.

Temperature dependent ZnO nanowire growth is shown in Figure 3.8. All other chemical solution parameters ($ZnSO_4$ 0.01M, NH4Cl 0.3M, pH 11 for 5hrs) were kept same. When chemical reaction took below 40 C, no nanowire growth was observed. It is believed that the energy at low temperatures was not enough to overcome the activation barrier. Up to 50 C, growth was enhanced with temperature increase. This can be explained from the fact that the growth process is a thermally activated heterogeneous growth process. Interestingly, the growth was reduced with temperature increase above 50 C. It is possible that the homogeneous nucleation and growth also happens at an elevated temperature > 50 C, so total heterogeneous growth is decreased relatively, as shown at high supersaturation situation.

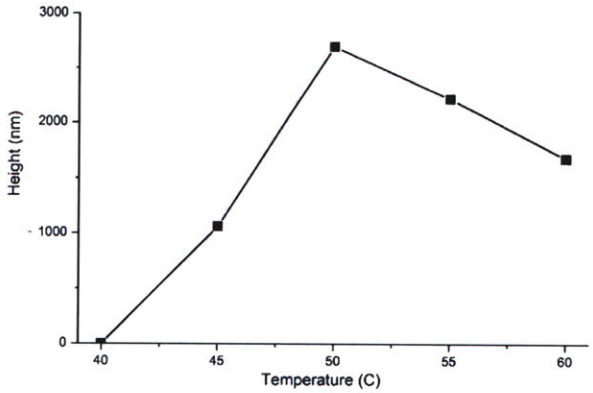


Figure 3.8.Temperature dependent nanowire growth characteristic. All other parameters were fixed ($ZnSO_4$ 0.01M, $NH_4Cl$ 0.3M, pH 11 in 100 mL for 5 hrs) except variable temperature.

Optical properties of ZnO nanowires were investigated using photoluminescent (PL) spectrum (Figure 3.9). Green light at 378 nm is believed to be a band edge emission from ZnO ($E_g \sim 3.3$ eV). Emission at 600 ~ 700 nm is not fully understood, but possibly from interstitial oxygen ions ($O_i^-$) [29]. This orange to red PL was seen at ZnO nanowire grown by hydrothermal system [30], electrochemical system [31], and spray pyrolysis [32]. When the nanowires were annealed at 240 C for 1 hr in air, this defect related emission was decreased and green line band edge emission was enhanced.

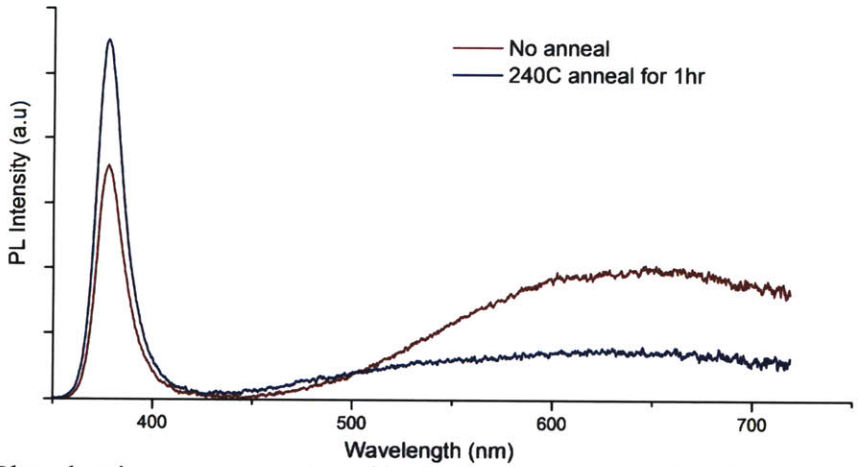


Figure 3.9. Photoluminescence spectra of hydrothermally grown ZnO nanowires with/without anneal at 240C for 1hr at air. Ultraviolet peak at 378 nm corresponds to band edge emission of ZnO, and broad peak at 600 ~ 700 nm corresponds to defect emission.

Figure 3.10 shows X-ray diffraction (XRD) pattern of the hydrothermally grown ZnO nanowires on Si substrate. High intensity of (0002) peak was observed as wurtzite structure ZnO (JCPDS card No. 36-1451), indicating vertically oriented ZnO nanowires in [0001] direction. No characteristic peaks from other impurities were detected except low intensity Si peaks. No specific difference in XRD was observed in samples with different time and chemical solution condition for the growth (data not shown).

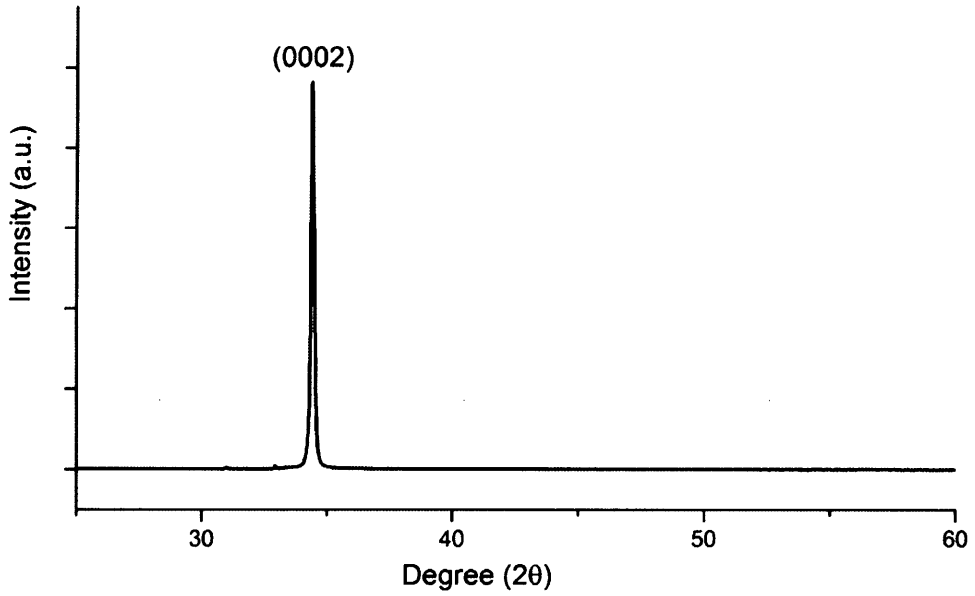


Figure 3.10. X-ray diffraction pattern of hydrothermally synthesized ZnO nanowire on Si (100) substrate. Strong (0002) indicates ZnO peak.

From the TEM image and selective-area diffraction patterns (Figure 3.11), it is seen that the nanowire is single crystalline, with a growth direction along c axis [0001]. The reason for the formation of the high aspect ratio nanowire instead of film can be explained by total free energy of the system. Because a polar (0002) plane has a high surface energy than a non polar lateral plane ($10\bar{1}0$), the crystal growth along the (0002) direction is energetically favorable leading to the formation of wire shaped ZnO crystals [33-36].

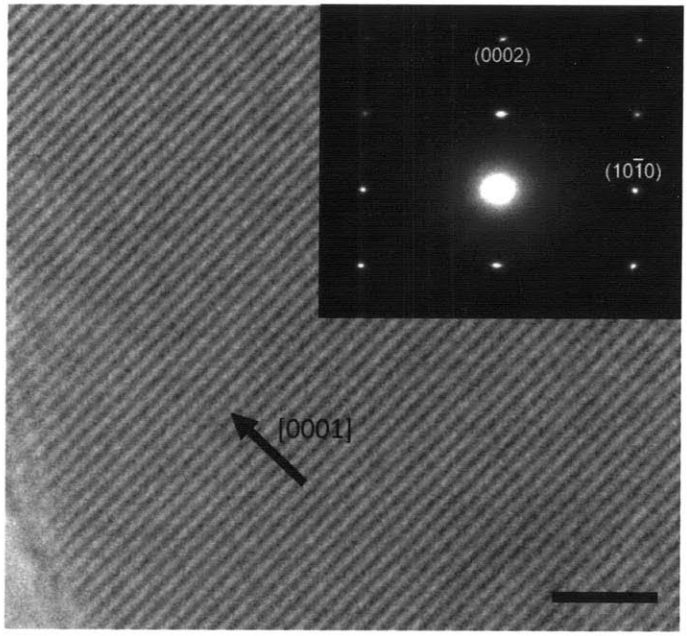


Figure 3.11. High resolution TEM image and selected area diffraction pattern (SADP) of hydrothermally synthesized ZnO nanowire. Scale Bar = 2 nm. SADP pattern shows single crystal with hexagonal structure.

## 3.4. Conclusion

In conclusion, we observed a strong relationship between supersaturation degree calculated from thermodynamic reactions and hydrothermal nanowire growth behavior. Calculated solubility plot gave a good indicator how much the supersaturation would be in certain chemical composition of reaction bath. Based on the experimental results, we observed that the supersaturation was the driving force for the phase change from liquid to solid, forming nanowires by heterogeneous nucleation and growth. At lower supersaturation, growth tends to be proportional to supersaturation degree as expected. This condition would be heterogeneous growth dominant region. However, smaller growth was observed above critical supersaturation condition, because of competition between homogeneous and heterogeneous nucleation and growth. This condition would be homogeneous nucleation and growth dominant region. Optical and crystalline

properties of ZnO nanowires indicated that the nanowire was single crystalline, having highly oriented wurtzite structure ZnO. Beside finding optimal parameters of ZnO nanowire synthesis, this relationship between supersaturation and nanowire growth may also lead to the development of low cost, solution based synthesis for other important materials in a rational manner, such as $TiO_2$, MgO, CdO, ZnS, ZnSe, and others [37-46].

# Chapter 4 : Morphology control of Nanowire Synthesis with Cations

## 4.1. Introduction

The ability to rationally control the morphology of nanostructures would enhance the ability to tune their optical and electrical properties, and improve the performance of nanostructure-based materials and devices [47-49].Many researchers have tried the shape control of ZnO nanowires under hydrothermal synthesis using additional polymers or solution condition changes, but detailed mechanism is still unclear [9, 50-53]. Here, we report the control of hydrothermally synthesized zinc oxide nanowire morphology, in which the growth direction is biased via electrostatic competition from cation-complexes that adsorb to the crystal in a face-specific manner, thereby reducing zinc ion-complex adsorption and suppressing growth along that face. Unlike in high temperature techniques that result in material exchange or doping, though, crystal incorporation of these competing ions is un-measurable, effectively making them inorganic pseudo-ligands. Varying only the competing ions in this all-inorganic batch process, we demonstrated synthesized low-aspect ratio platelets, as well as high-aspect ratio nanowires sharpened sufficiently to create field-emitters with emissivity equivalent to single-walled carbon nanotubes. These results are explained in a thermodynamic model based on electrostatic interactions determined by the species $pK_a$ and zeta-potential of the respective crystalline faces.

## 4.2. Experiments

For the growth of morphology controlled ZnO nanowires, pre-cleaned Si substrate was coated with a ZnO seed layer (2 ~ 30 nm thick) by RF sputtering (150W, 20mTorr, 12sccm Ar). The substrate was placed upside down in a 100 mL solution in a closed system containing fixed concentration of zinc sulfate ($ZnSO_4 \cdot 7H_2O$ 0.01M, Sigma

Aldrich) and ammonium chloride ($NH_4Cl$ 0.3M, Sigma Aldrich) with additional variable concentration of metal sulfate hydrate ($Al_2(SO_4)_3 \cdot 18H_2O$, $In_2(SO_4)_3 \cdot xH_2O$, $Ga_2(SO_4)_3 \cdot xH_2O$, $SrSO_4$, $CaSO_4 \cdot 2H_2O$, $MgSO_4 \cdot 7H_2O$, $CuSO_4 \cdot 5H_2O$, $CdSO_4 \cdot 8/3H_2O$, 0 ~ 0.002M, Sigma Aldrich), followed by pH adjustment to 11 by sodium hydroxide (NaOH, Sigma Aldrich). This enclosed system was then heated to 60 C in a convection oven at various times for the nanowire growth.

Composition of nanowires was characterized by JEOL 2010F field emission transmission electron microscope (FE-TEM) equipped with energy dispersive X-ray spectroscopy (EDS). Morphology and aspect ratio of nanowires were measured using Philips-FEI XL30-ESEM field emission scanning electron microscopy (SEM) with secondary electron detector in normal high vacuum mode. Crystalline structure and orientation of the nanowires was identified by X-ray diffractometry (XRD, Panalytical X'pert Pro) using CuK$\alpha$ (1.5406Å) radiation. Photoluminescence of ZnO nanowires was measured by spectrophotometer (F7000, Hitachi) with excitation of 325nm using monochromatized Xe source at room temperature.

Force-distance measurement was used to evaluate surface potential of ZnO single crystalline surface at pH 11. Au coated contact mode AFM cantilevers (Budget Sensors, force constant 0.2N/m) were chemically modified with carboxylic alkanethiol monolayer to form carboxylic acid surface over the tip surface [54-55]. Initially, the cantilevers were pre-cleaned with concentrated $H_2SO_4$ for 5 minutes, and washed with DI water and ethanol. The cantilevers were then immersed in 1 mM solution of mercaptoundocanoic acid in ethanol for overnight to form self assembled monolayer. Before installing the tip to the AFM (Digital Instrument 3000), the cantilever was taken out from the solution and

rinsed with ethanol, hexane, ethanol, and dried under nitrogen. Single crystal ZnO (MTI Corporation) with (0002), $(10\bar{1}0)$, and $(11\bar{2}0)$ planes were used in this experiments. All crystals were thoroughly rinsed with DI water, dried under nitrogen. To measure surface potential of ZnO planes at pH 11, sodium hydroxide (NaOH, Sigma Aldrich) was used to adjust pH of 1 mM KCl solution to 11. The crystal was placed beneath the carboxylic acid functionalized AFM tip with 50 uL solution and allowed to equilibrate for 5 minutes. Once the system was stabilized, force distance measurement was taken at scan rate of 1 Hz.

X-ray photoelectron spectroscopy (XPS) was used to determine the relative surface acidities of ZnO crystals with different orientations [56]. ZnO crystals with three different planes were coated with 5Å thick palladium (Pd) by RF sputtering (70W, 30mTorr, 12 sccm Ar for 18 seconds). All XPS measurements were performed using monochromatic Al K$\alpha$ radiation under ultra high vacuum ($1.2 \sim 5 \times 10^{-10}$ Torr) at takeoff angle of $30^{o}$ from the plane. Pd 3d photoelectron peaks and Pd MMV auger peaks were measured to determine the modified auger parameter (MAP) of Pd as a function of crystalline orientation. Pd was used because it is chemically inert, and its specific peaks do not overlap with Auger peaks of zinc, oxygen, and carbon.

## 4.3. Results and discussion

Nanowires synthesized with additional cations showed dramatic morphology and aspect ratio changes. Each cation showed distinctive effects on the growth, either suppressing the nanowire vertical growth and forming nanoplates shape, or sharpening the nanowires into spear shape. Depending on ion addition concentrations, trends to sharpen or flatten the nanowires enhanced up to certain aspect ratio points.

Figure 4.1 Shows SEM images of nanowires grown with cadmium sulfate addition (a: 0.002M, c: 0.001M), no addition (e), and aluminum sulfate addition (g: 0.001M, i: 0.002M) with all other parameters kept same. Compared to no additional cation addition (e), Cd added solution induced growth in platelet shape with low aspect ratio, instead of vertical wire growth. It is seen that growth in lateral direction was enhanced, and vertical growth was suppressed. In case of Al added solution, growth in vertical direction was more enhanced, and synthesized nanowires shows increased aspect ratio.

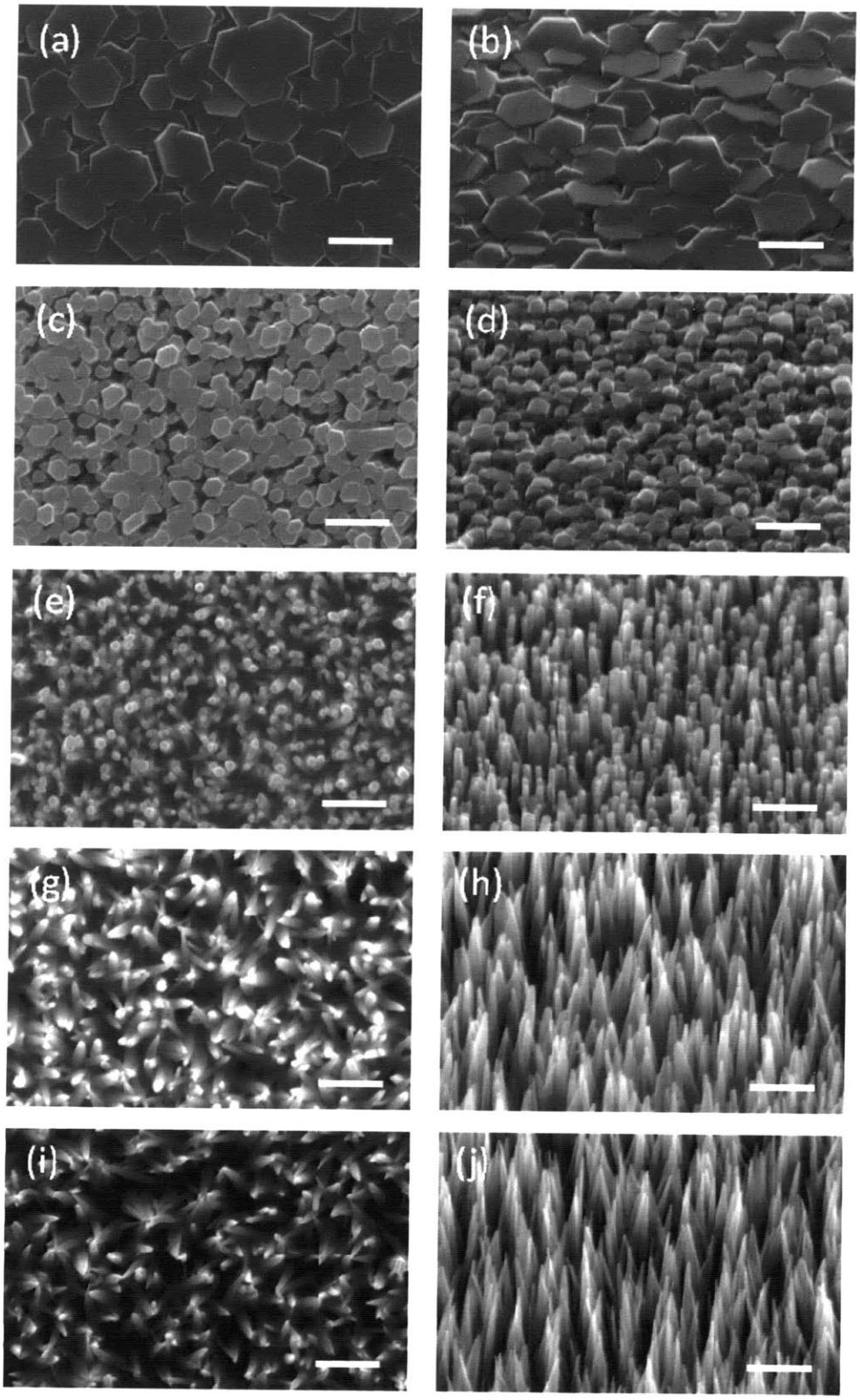


Figure 4.1. Top (a, c, e, g, i) and 45 degree tilted (b, d, f, h, i) SEM images of nanowire grown at 5 different chemical solutions. (a,b): Cd 0.002M, (c,d): Cd 0.001M, (e,f): no additional cations, (g,h): Al 0.001M, (i,j): Al 0.002M. Scale bar = 500 nm.

To evaluate the effect of cations for the morphology changes, various materials with different concentration of add ions were tested. Figure 4.2 shows measured aspect ratio from SEM cross sectional analysis with eight different cations for ten different concentrations. Aspect ratio tends to increase with Al, In, and Ga addition, whereas decrease with Ca, Mg, Cu, and Cd. In case of Sr, no distinctive trend was observed because of aspect ratio fluctuation with different concentrations.

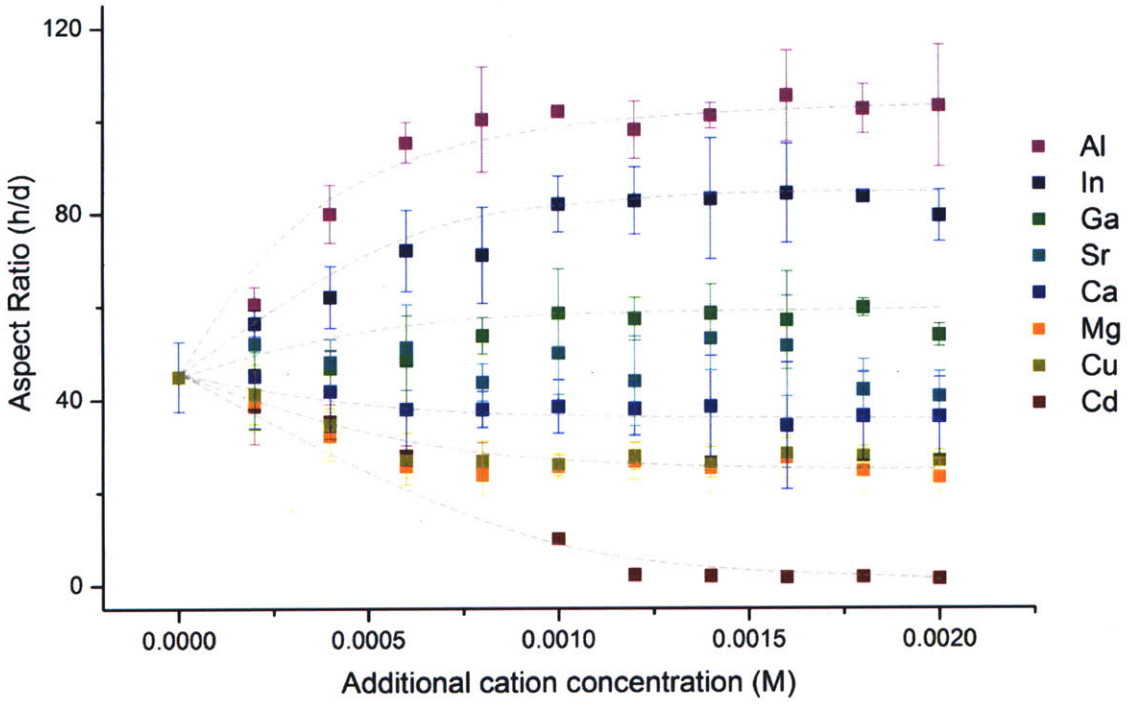


Figure 4.2. Aspect ratios of synthesized nanowires measured by cross sectional SEM with 8 different cations with 10 different concentrations respectively.

In chemical solution bath for ZnO nanowire growth, several zinc ion complexes exist; zinc hydroxide complexes and zinc amine complexes. When cations other than Zn are introduced in the reaction solution, they also form complexes either with hydroxide and amine. Because total hydroxide and amine concentration is fixed at certain condition, Zn complex distribution also changes by additional cations. Those charged ion complexes

will adhere to specific crystal facet of ZnO, which is energetically favorable direction. This selective zinc complex adsorption determines the shapes of crystals.

As each surface plane of single crystal have different surface energies, every plane has different surface potentials defined by isoelectric point (IEP) when the crystal is introduced in the solution. Since hydroxide and proton can adsorb to or desorb from the crystal plane, surface potential changes with pH. IEP is the pH where the surface potential is zero, neutral charge condition. Crystal surface forms positive charges when pH < IEP. When pH > IEP, the surface forms negative charges. Since each crystal plane has different atomic distributions, each plane would have different IEP defined by orientation [56-58]. Several IEP values for bulk powder (multiple facets) with different materials are already known, but not much of data for crystal plane dependent IEP are available yet.

For ZnO, previously reported (0002) plane IEP is 8.7±0.2 [55]. In our experimental condition at pH 11, (0002) plane would form negative surface charges. Since (0002) planes consists of all Zn atoms and $(10\bar{1}0)$ planes consists of ½ Zn and ½ O atoms, (0002) would have higher binding forces to hydroxyl groups and easily form negatively charged condition. Therefore, IEP would be lower for (0002) plane. Since there is no reported value of surface potential of $(10\bar{1}0)$, let's assume that the $(10\bar{1}0)$ would have positive charges under pH 11, and examine whether this surface potential conditions can explain the morphology and aspect ratio changes with different cation additions as shown in Figure 4.3. Detailed surface charge measurements by AFM and XPS analysis would be followed after that.

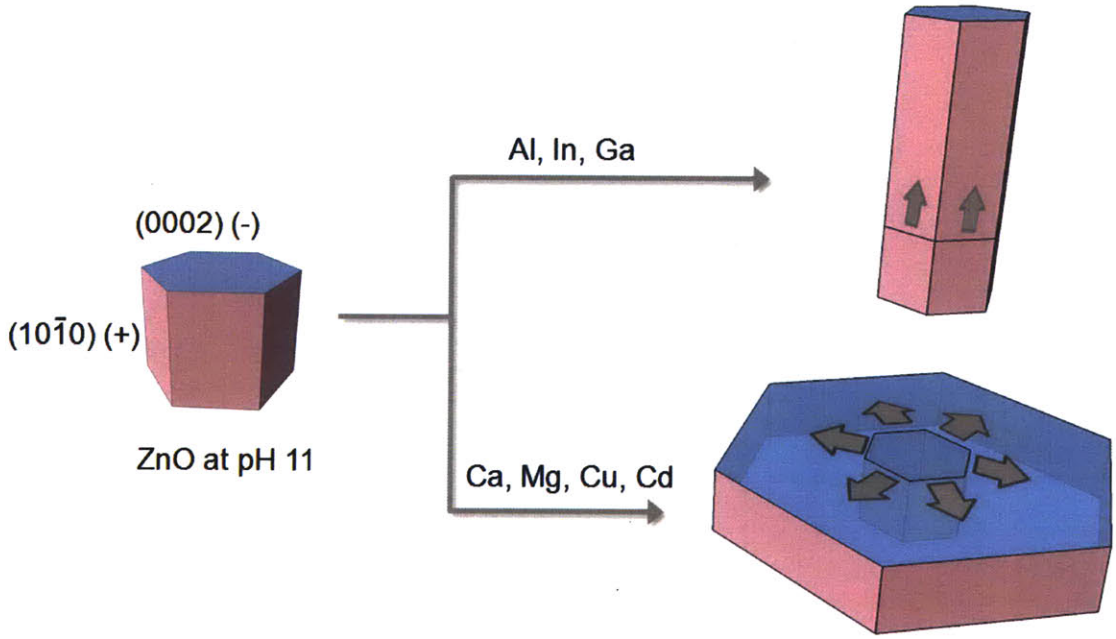


Figure 4.3. Schematic diagram of ZnO growth at different cation addition. Possible scenario of surface potentials at ZnO facets. Different ZnO nanostructures may form by competing ion mechanism.

Solubility plots for Zn and Cd in the reaction solution are shown in Figure 4.4. Cd has different solubility from Zn. Cd also have a solubility increase around pH 8 ~ ph 12 under $NH_4Cl$ existence because of Cd amine complex formation.

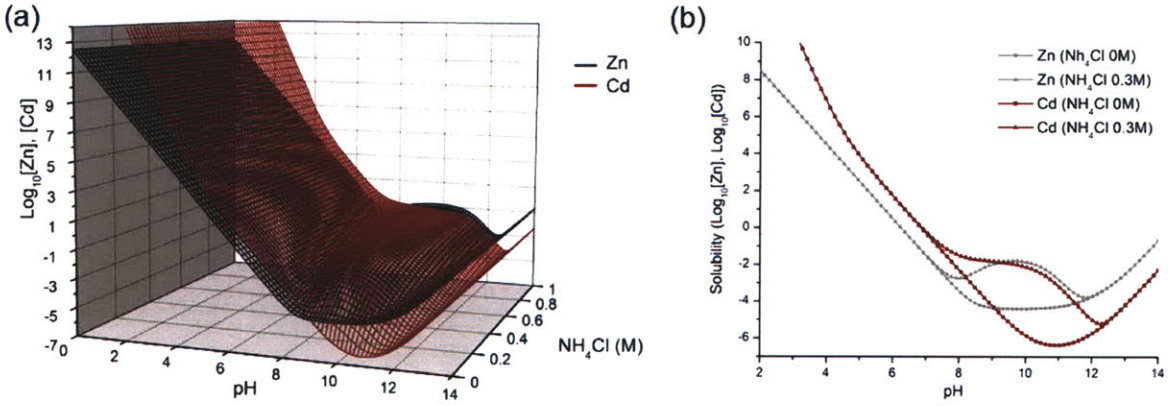


Figure 4.4. (a) Solubility plots of Zn (grey) and Cd (red) with different pH/$NH_4Cl$ concentrations calculated by Matlab code with reaction constants (see appendix). (b) Solubility plots of Zn and Cd with two different concentrations of $NH_4Cl$ (0M, 0.3M).

Equivalent Zn ion complex distribution and Cd ion complex distribution at 0.3M $NH_4Cl$ are shown in Figure 4.5. Complexes with same polarity were added up to investigate the charge distribution of complexes. For Zn complexes case, positive charge value is sum of $Zn(OH)^+$, $Zn(NH_3)^{2+}$, $Zn(NH_3)_2^{2+}$, $Zn(NH_3)_3^{2+}$, and $Zn(NH_3)_4^{2+}$. Negative charge value is sum of $Zn(OH)_3^-$ and $Zn(OH)_4^{2-}$. Neutral charge value is $Zn(OH)_2\ (aq)$. Similar process was taken for Cd complex distribution, and charges with each polarity were calculated. At experimental condition (pH 11), most of Zn ions would exist as positive charge complexes (96.3 %) and most of Cd ions as positive charge complexes (99.9 %). Nanowires grows vertically when most of Zn attaches in vertical direction, and this agrees with the assumption that (0002) plane has negative zeta potential and $(10\bar{1}0)$ plane has positive zeta potential. By electrostatic forces, majority of

Zn complexes, which has positive polarity, will be attracted to the (0002) plane and the crystal will grow vertically. However, when Cd is present in the solution, there are Cd complexes competing with Zn complexes during growth. Since majority of Cd complexes are positive, these would be attracted to (0002) plane and suppress the positive Zn complexes attaching to (0002) plane. Vertical growth would slow down by this competing ion complex mechanism, but lateral growth will still happen, thereby forming nanoplates.

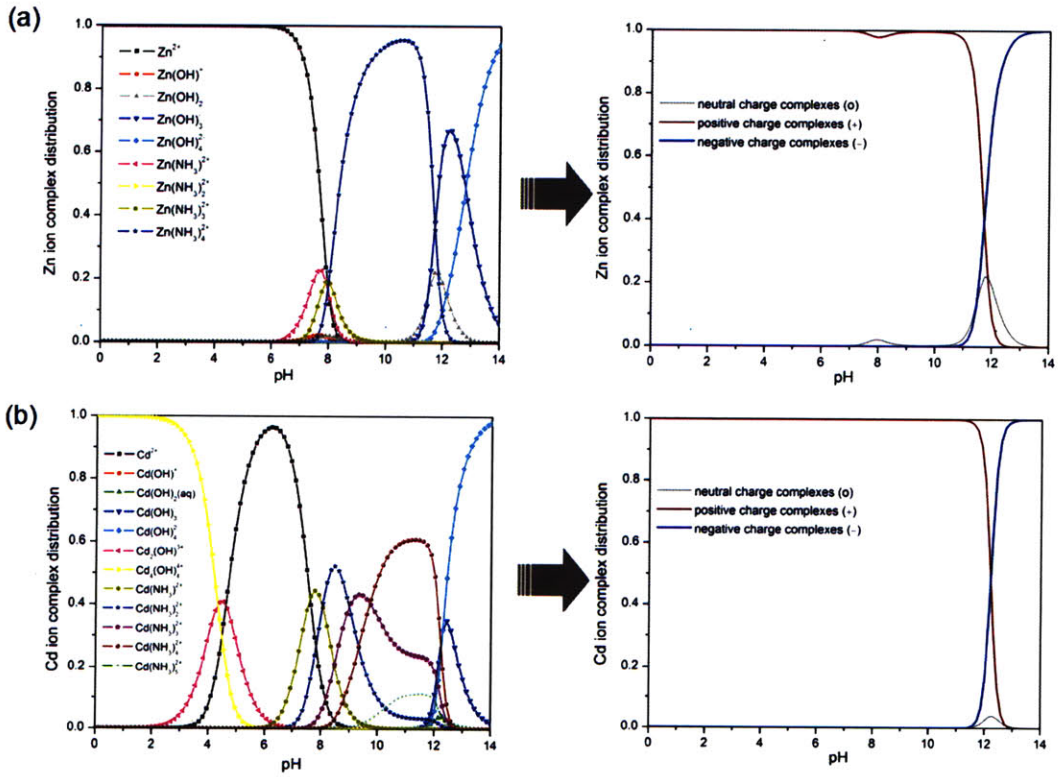


Figure 4.5. Calculated Zn ion complex distribution (a) and Cd ion complex distribution (b) at different pH with 0.3M $NH_4Cl$ condition.

Solubility plots for Zn and Al in the reaction solution are shown in Figure 4.6. In case of Al, solubility has no bump when $NH_4Cl$ is present, because Al does not form Al amine complexes.

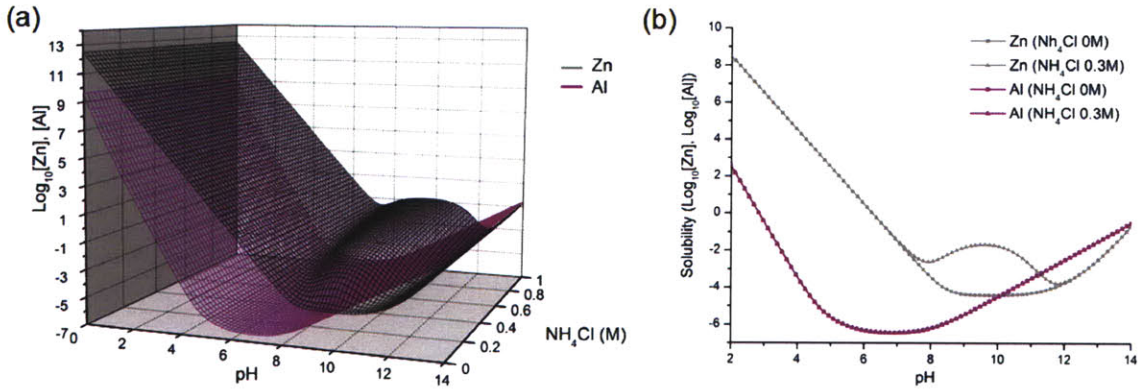


Figure 4.6. (a) Solubility plots of Zn (grey) and Al (red) with different pH/$NH_4Cl$ concentrations calculated by Matlab code with reaction constants (see appendix). (b) Solubility plots of Zn and Al with two different concentrations of $NH_4Cl$ (0M, 0.3M).

Equivalent Zn ion complex distribution and Cd ion complex distribution at 0.3M $NH_4Cl$ are shown in Figure 4.7. Complex distribution of Zn was different from Cd addition situation (Figure 4.5), because Al and Cd have different chemical reactions with hydroxide and ammonia (see Appendix). Similar procedure was taken to evaluate the proportion of ion complexes with different polarity. At this case, main Zn complexes are positive (96.4 %), and main Al complexes are negative (99.9 %). Based on the surface potential assumption, most of Zn complexes (+) will be attracted to negative zeta potential (0002) plane without competing with main Al complexes (-). Main Al complexes would be attached to the positive $(10\bar{1}0)$ plane and compete with minor Zn complexes (-) in lateral direction. Overall, Al addition would not hamper the vertical growth but suppress the lateral growth, thereby creating higher aspect ratio nanowires than no additional cation condition.

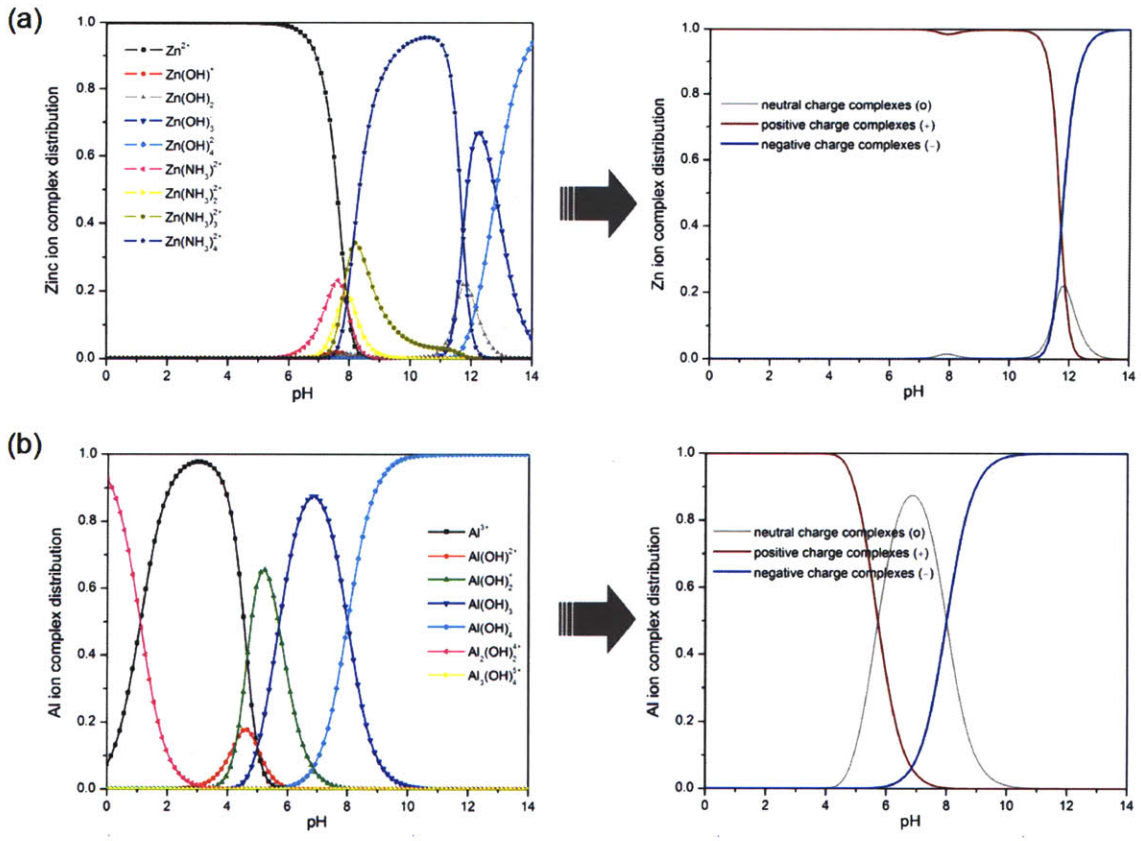


Figure 4.7. Calculated Zn ion complex distribution (a) and Al ion complex distribution (b) at different pH with 0.3M $NH_4Cl$ condition.

Based on the previous two cases with Cd and Al addition, electrostatic competing ion mechanism explains the experimental results of morphology and aspect ratio change reasonably. To check whether other cations also fit into this model, same charged ion complex distributions with rest of cations were calculated.

Charge complex distribution of indium added solution was shown in Figure 4.8. At pH 11, major Zn complexes (96.4%) have positive polarity, and major In complexes (95.5%) have negative polarity. In this case, In would suppress the growth in $(10\bar{1}0)$ plane, forming higher spect ratio as observed from the experiments.

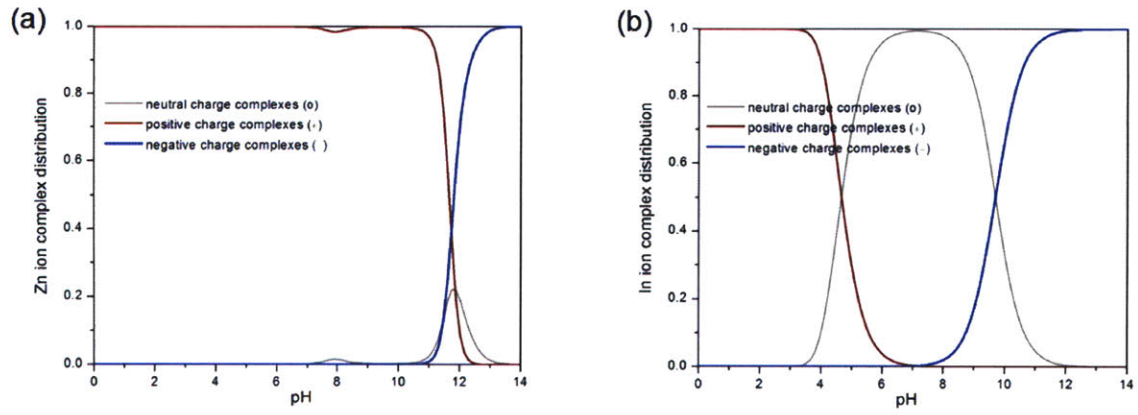


Figure 4.8. Charged complex distribution of Zn and In under 0.3M $NH_4Cl$ condition. (a) Zn complex distribution with different polarities. (b) In complex distribution with different polarities.

Figure 4.9 Shows charge complex distribution of gallium added solution. Main Zn complexes (96.4%) have positive polarity, and main Ga complexes (99.9%) have negative polarity under experimental condition (pH 11). Similar to Al and In, Ga would suppress the growth in $(10\bar{1}0)$ plane and create higher spect ratio nanowires as observed from the experiments.

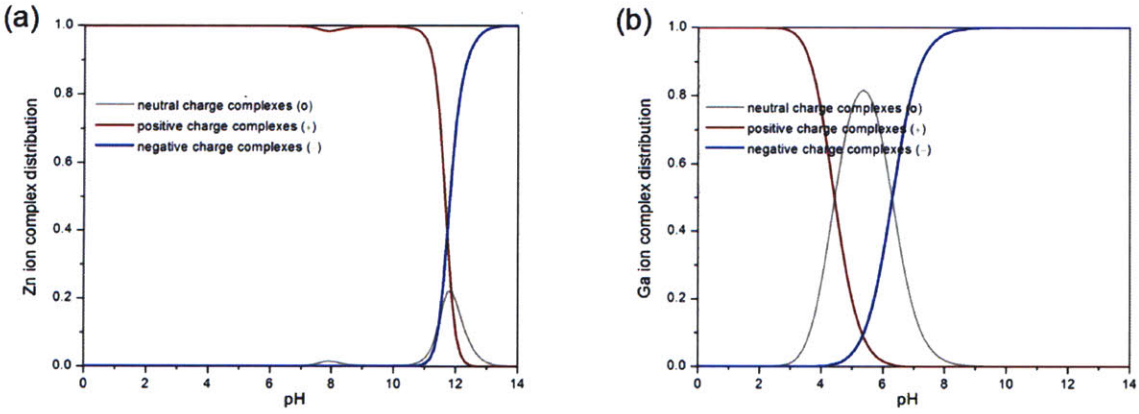


Figure 4.9. Charged complex distribution of Zn and Ga under 0.3M $NH_4Cl$ condition. (a) Zn complex distribution with different polarities. (b) Ga complex distribution with different polarities.

Charge complex distribution of copper added solution was shown in Figure 4.10. At pH 11, major Zn complexes (96.3%) have positive polarity, and major Cu complexes (99.9%) have negative polarity. In this case, Cu would compete with main Zn complexes on attaching (0002) plane, thereby suppressing vertical growth. As a result, platelet shape structures would form, matching experiments.

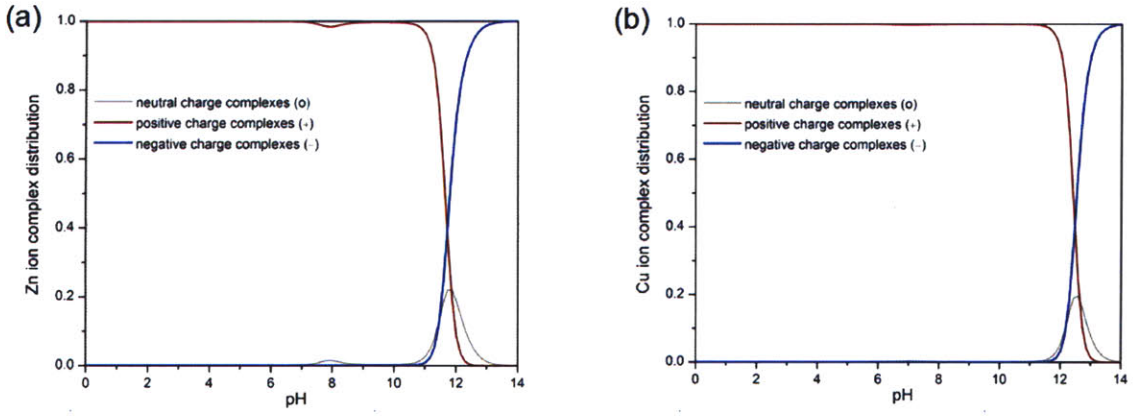


Figure 4.10. Charged complex distribution of Zn and Cu under 0.3M $NH_4Cl$ condition. (a) Zn complex distribution with different polarities. (b) Cu complex distribution with different polarities.

Figure 4.11 Shows charge complex distribution of magnesium added solution. Main Zn complexes (96.4%) have positive polarity, and main Mg complexes (99.9%) have positive polarity under experimental condition (pH 11). Similar to Cd and Cu, Mg would suppress the growth in (0002) plane and create low aspect ratio nanoplates as observed from the experiments.

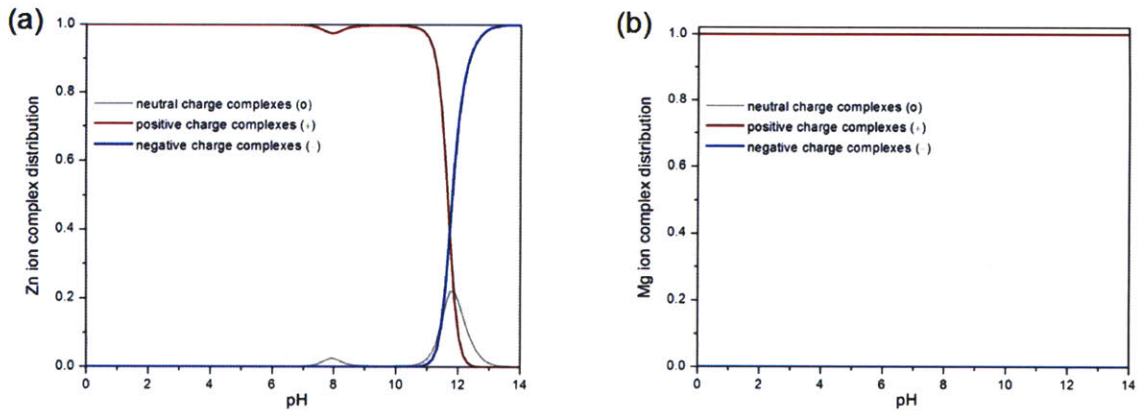


Figure 4.11. Charged complex distribution of Zn and Mg under 0.3M $NH_4Cl$ condition. (a) Zn complex distribution with different polarities. (b) Mg complex distribution with different polarities.

Charge complex distribution of calcium added solution was shown in Figure 4.12. At pH 11, Zn complexes are 69.0% neutral, 7.2% positive, and 23.8% negative. Neutral Zn complexes can attach either positive or negative zeta potential surfaces. Ca complexes have 100% positive polarity. In this case, Ca would compete with positive Zn complexes on attaching (0002) plane, thereby suppressing vertical growth. As a result, low aspect ratio structures would form. It is not clear why the aspect ratio change with Ca addition was not as significant as Cd addition case. It may be related to the fact that main complexes are neutral instead of positive polarity. Also, difference in atomic size of cations and adsorption coefficient of the each complex molecule needs to be considered.

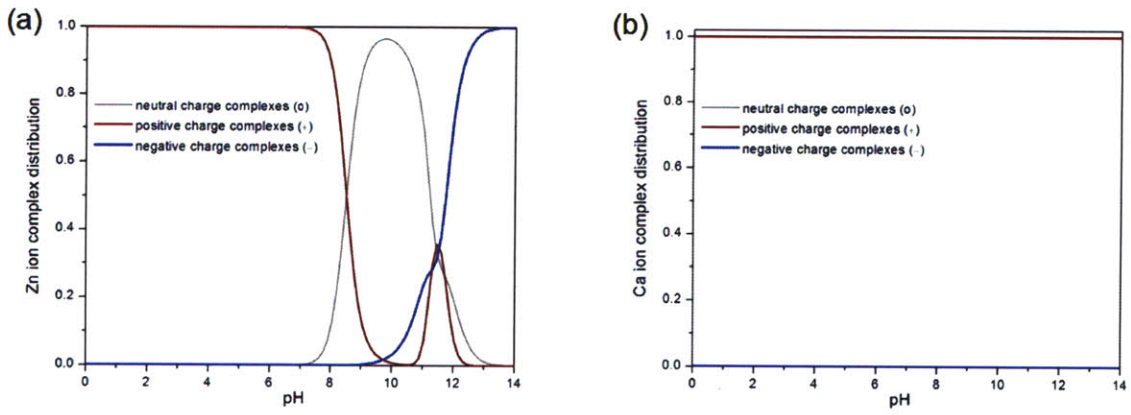


Figure 4.12. Charged complex distribution of Zn and Ca under 0.3M $NH_4Cl$ condition. (a) Zn complex distribution with different polarities. (b) Ca complex distribution with different polarities.

Figure 4.13 Shows charge complex distribution of strontium added solution. Main Zn complexes (96.4%) have positive polarity, and main Sr complexes (100%) have positive polarity under experimental condition (pH 11). In this case, Sr should suppress the (0002) plane growth and decrease the aspect ratio of ZnO, but experimental results shows no tendency of aspect ratio change. This would come from the fact that $SrSO_4$ has extremely low solubility under DI water ($3\sim4 \times 10^{-7}$). Different from other cation sulfate hydrate used for experiments that have high solubility in water, Sr used for experiment was $SrSO_4$ (no hydrate form available). Within the concentration range (0.0002M ~ 0.002M), $SrSO_4$ was still sedimented without dissolution when added to prepared solutions. However, the calculated situation assumes that Sr is fully dissociated from the initial form of chemicals. If almost no Sr complexes exist in the solution because of low solubility of initial chemicals, the Zn charge ion distribution would be almost the same as no additional cation situation. Therefore, aspect ratio would not change significantly to certain direction with $SrSO_4$ concentration changes.

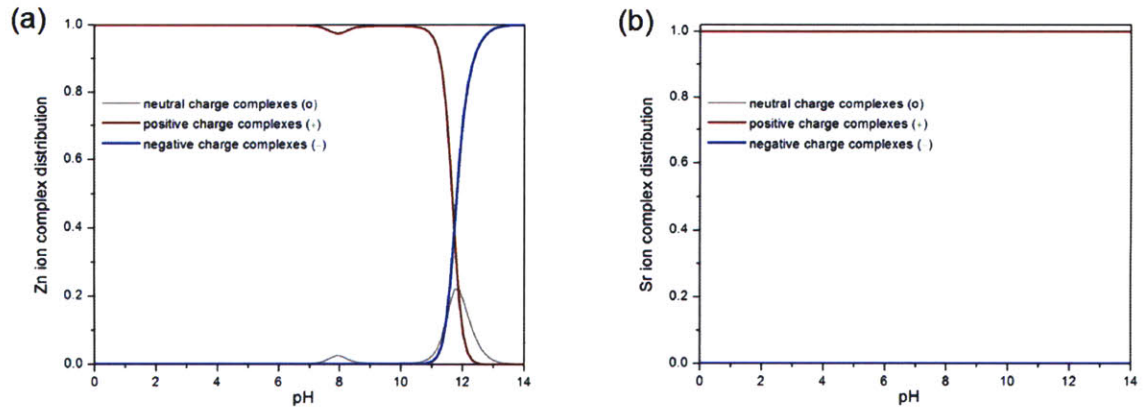


Figure 4.13. Charged complex distribution of Zn and Sr under 0.3M $NH_4Cl$ condition. (a) Zn complex distribution with different polarities. (b) Sr complex distribution with different polarities.

To evaluate whether electrostatic competing ion model is valid approach to explain the experimental results, surface potentials of (0002) plane and $(10\bar{1}0)$ were analyzed by force-distance measurement with AFM. Figure 4.14 shows functionalized AFM tip with mercaptoundecanoic acid. Thiol groups bond to Au coated AFM tip surface, leaving carboxylic acid groups at the end. At pH > 6.5, carboxylic acid would be entirely deprotonated [59], forming negatively charged tip above pH 6.5. Since the force measurement was done at pH 11, tip would be fully negatively charged.

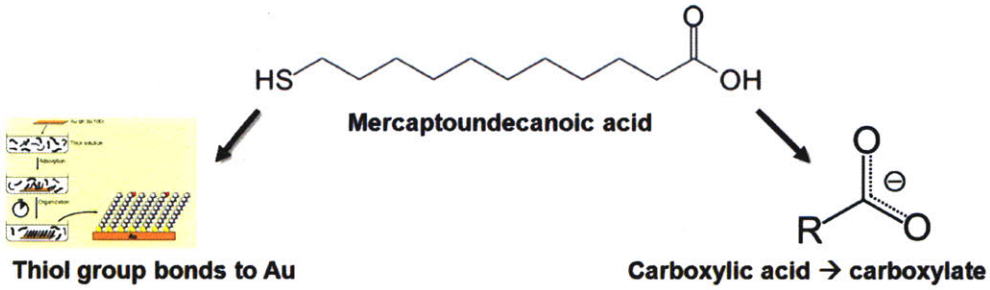


Figure 4.14. Chemical attachment of mercaptoundecanoic acid to Au and formation of (-) polar surface under solution. Au thiol bond image taken from [60].

Figure 4.15 shows two different conditions of cantilever deflection-distance plots.

Under 1mM KCl solution with pH 11, functionalized AFM tip would remain negatively charged. If certain crystal surface has lower IEP than pH 11, that surface would be negatively charged under ph 11. At this situation, electrostatic repulsive force between the surface and the tip would exist, and the cantilever would deflect to upper direction when approaching to the surface (Figure 4.15 b). When the tip is too close by further approaching, the Van der Waals force would dominate and deflection would go downward. If the crystal surface has higher IEP than pH 11, the surface would be positively charged under pH 11. At this situation, electrostatic attraction force would dominate during approach (Figure 4.15 c), so the cantilever would be deflected downward. Van der Waals force would be attractive also, so no reversal cantilever deflection would be observed.

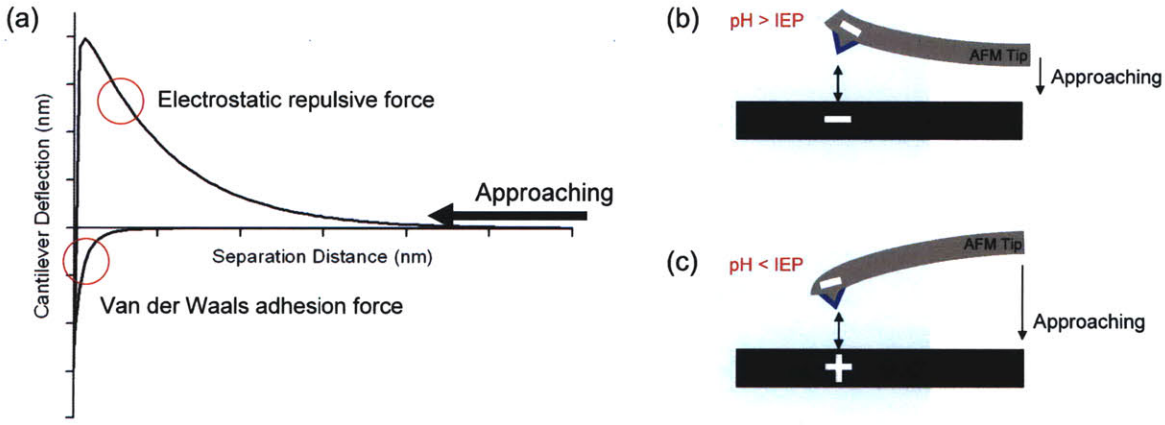


Figure 4.15. (a) Schematic drawing of cantilever deflection under attractive and repulsive electrostatic force during approaching condition. (b) Electrostatic repulsive force dominant when the surface is negative (pH>IEP) and the tip is negative (carboxylate). (c) Electrostatic attraction force dominant when the surface is positive (pH<IEP) and the tip is negative (carboxylate).

Figure 4.16 Shows experimental results of Force-Distance measurement with single crystalline surfaces of (0002) Zn terminated plane and $(10\bar{1}0)$ plane. (0002) plane showed electrostatic repulsive long range force, indicating the surface is negatively

charged under pH 11. This repulsive force and negative potential of (0002) plane under pH 11 matches with previously reported literature [55]. In case of $(10\bar{1}0)$ plane, only attractive force was observed at pH 11, indicating the surface is positively charged. This experimental data support the competing ion model assumption that (0002) plane to be negative, $(10\bar{1}0)$ plane to be positive potential.

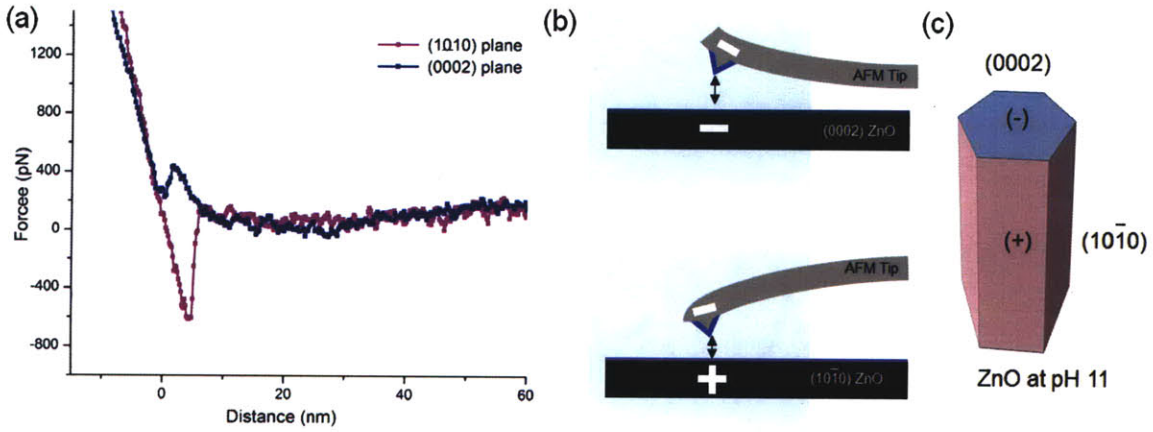


Figure 4.16. (a) Force-Distance measurement of single crystalline (0002) and $(10\bar{1}0)$ plane ZnO under pH 11 solution with carboxylate functionalized AFM tip. (b) AFM deflection schematic drawing of two different planes under pH 11. (c) Possible situation of surface polarity with ZnO nanostructures under experimental condition (pH 11).

To further support the surface potential differences between different surfaces of ZnO, x-ray photoelectron spectroscopy (XPS) was performed. XPS spectra of 3d photoelectron peaks and MMV Auger peaks of monolayer deposited Pd on different crystalline orientations of ZnO is shown in Figure4.17. Data shows almost identical Auger peaks of Pd signal on all three crystalline surfaces. However, the photoelectron peaks of binding energies showed a difference of 0.25 eV between different crystal surfaces. The photoelectron peak of Pd on $(10\bar{1}0)$ surface had lowest binding energy, while the peak at $(11\bar{2}0)$ occurred at 0.125 eV higher, and peak at (0002) showed 0.25 eV higher than the lowest. Both modified auger parameter (MAP) and calculated cation

density is shown in table 4.1. It is seen that the surface with higher cation density has higher MAP. Correlation between MAP and surface charges of surfaces can be explained by classic electrostatic model which others reported with sapphire and titanium oxide crystals [56, 58]. The binding energy of electrons from a Pd monolayer would increase with net positive atomic charges of the crystalline substrate. Therefore, the surface with higher binding energy will also have stronger bonds to hydroxyl groups in the solution environment, and require more protons to change the surface charges from negative to positive. As a result, the surface plane with higher binding energy would have lower IEP. From the binding energy value measured, $(10\bar{1}0)$ plane would have highest IEP, followed by $(11\bar{2}0)$ and (0002). Since (0002) surface has highest binding energy, it would easily be negatively charged compared to $(10\bar{1}0)$ surface that requires higher pH to accommodate lower binding energy to change the polarity of the surface. This XPS matches with AFM data that (0002) surface is negatively charged at pH 11, but $(10\bar{1}0)$ surface is still positively charged.

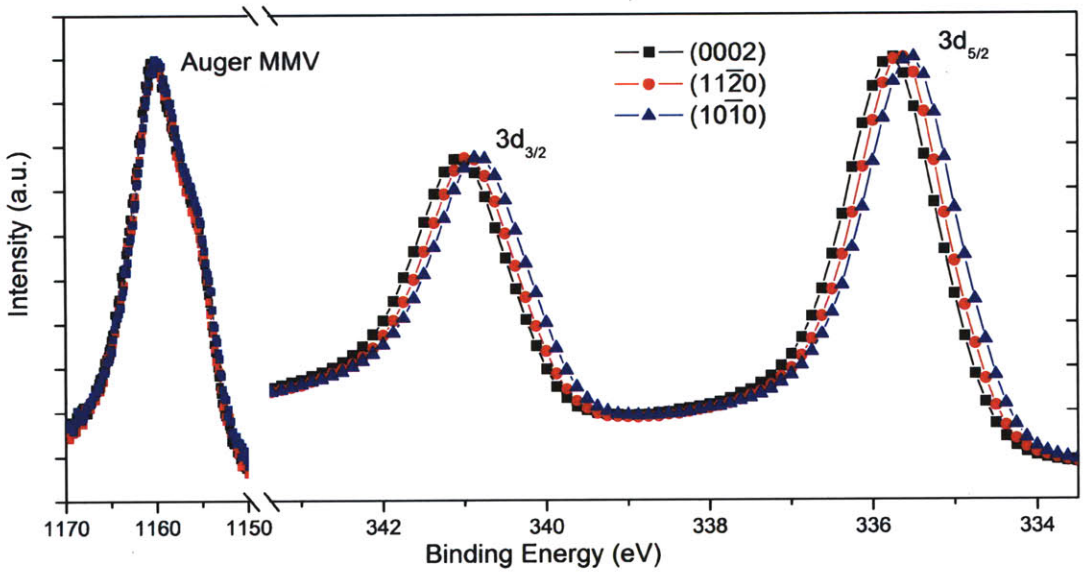


Figure 4.17. XPS data of Auger MMV peak and photoelectron ($3d_{3/2}$ and $3d_{5/2}$) peaks of an atomic monolayer of palladium deposited on three different ZnO crystal surfaces. Different binding energies indicate a difference in the extent to which electrons from Pd are bound to surface sites on their corresponding wurtzite ZnO substrates.

| Orientation | M.A.P. | Cation density ( per nm$^2$) |
|---|---|---|
| (0002) Zn terminated | 824.375 | 10.9 |
| (11$\bar{2}$0) | 824.500 | 6.8 |
| (10$\bar{1}$0) | 824.625 | 5.9 |

Table 4.1. Modified Auger Parameters and cation density of ZnO crystals with different surfaces. (Note that lower MAP corresponds to higher binding energies because MAP is difference between Auger peak (high value) and photoelectron peak.)

We performed EDS measurement for individual nanowires under TEM to investigate how much incorporation of additional cations to the nanowires. Figure 4.18 shows EDS data for nanowires at specific growth condition. No Cd or Al peak was observed within detectable limit of tool capability, indicating additional cation only works as pseudo ligands of suppressing certain crystal growth plane, but not incorporating into crystals effectively.

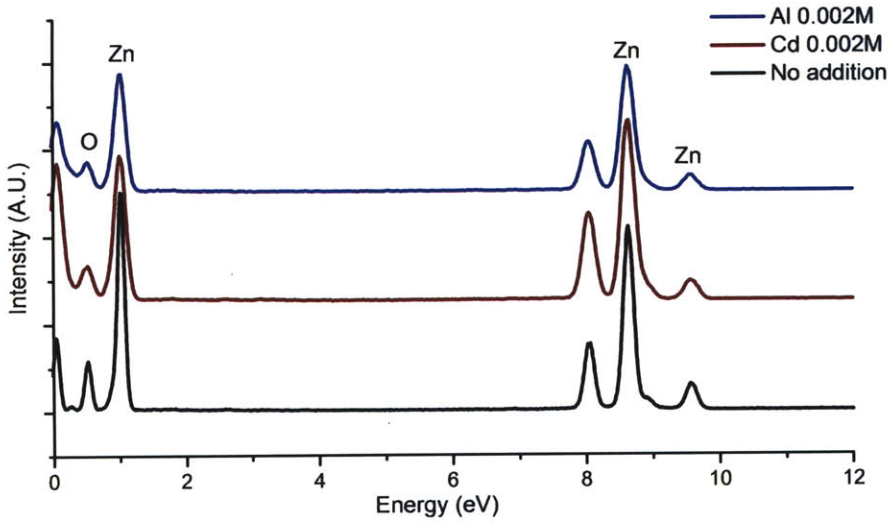


Figure 4.18. Energy Dispersive X-ray spectroscopy (EDS) measurement for individual nanowires grown at different conditions. No distinctive peak or Cd or Al is observed.

Normalized XRD data for samples with different cation addition also showed no change in crystalline orientation of ZnO nanowires (Figure 4.19). All nanowires to nanoplates showed strong ZnO (0002) peak, indicating same alignment of ZnO nanostructures. No other peaks of additional metal or metal oxide phase were observed.

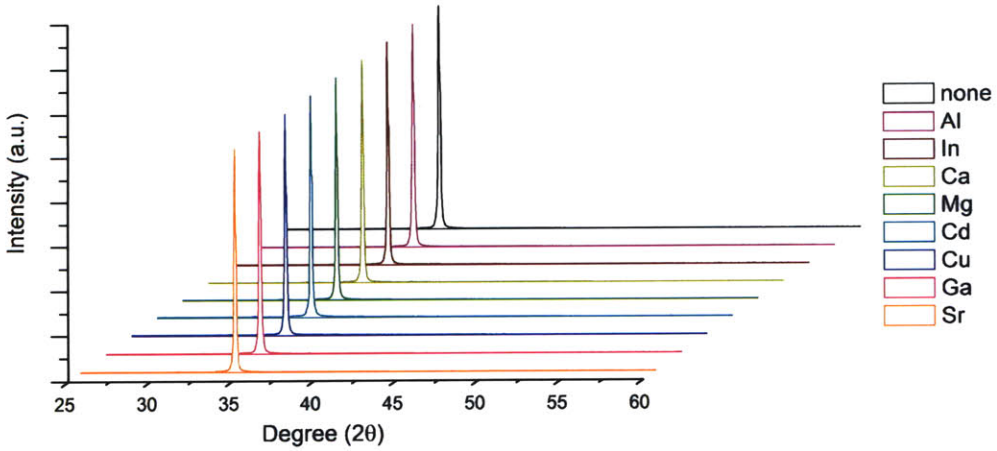


Figure 4.19. X-ray diffraction pattern of hydrothermally synthesized ZnO nanowire with different cation addition (0.002 M) on Si (100) substrate. Strong peak indicates (0002) ZnO peak. No other peaks were observed.

PL data with different cation added nanowire growth was shown in Figure 4.20. Every sample showed distinctive band edge emission at ~ 378 nm, and defect related emission at 600 nm ~ 700nm possibly by oxygen interstitials. Depending on samples, band edge emission intensities were different, but no peak shift at band edge was observed, indicating no optical band gap changed by forming ternary phases. The reason for the intensity change of band edge and defect emission is still not clear. It may be related to the morphology variations in samples, leading to different proportion of surface related defect emission with respect to band edge emission.

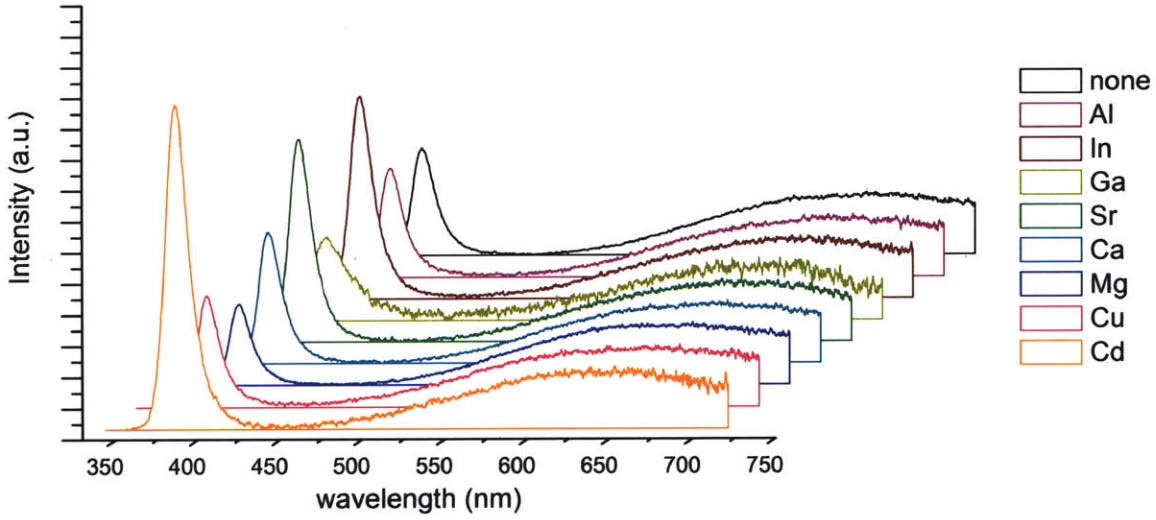


Figure 4.20. Photoluminescence spectra of hydrothermally grown ZnO nanowires with different cation addition (0.002 M). Ultraviolet peak at 378 nm corresponds to band edge emission of ZnO, and broad band defect emission at 600 ~ 700 nm were observed. No peak shift of band edge emission was observed.

In case of suppression of lateral growth in $(10\bar{1}0)$ direction by Al, In, or Ga, needle shape around the top end of the nanowire was generally observed in addition to the diameter decrease. Hexagonal structures are gradually contracted along the [0001] axis with an angle of 87±0.9 degree (Figure 4.21). This needle structure is different from the prism or pyramid structures of ZnO with facets $(10\bar{1}1)$ that has 60 degree angle with

(0002) plane which other people generally reported [61-65]. In our case, multiple steps along the lateral faces instead of flat tilted faces were observed. It indicates that the needle shape around the tip comes from multiple layers of hexagonal crystal structures with gradually decreased areas (Figure 4.21e) [66-68]. We believe that the suppression of $(10\bar{1}0)$ planes by additional ion complexes induces diameter of the ZnO to be gradually decreased. Comparative growth rate increase along the vertical direction because of suppressed growth rate along the lateral direction by additional cation complexes would induce steps on the (0001) face do not move across the face rapid enough, and new layers are nucleated before the previous layers grow across (Figure 4.21f). Crevices and hillock formation in ZnO single crystal growth was also explained in a similar manner that too fast vertical growth compared to lateral growth induced sharp tip shaped crevice flawed crystals [69].

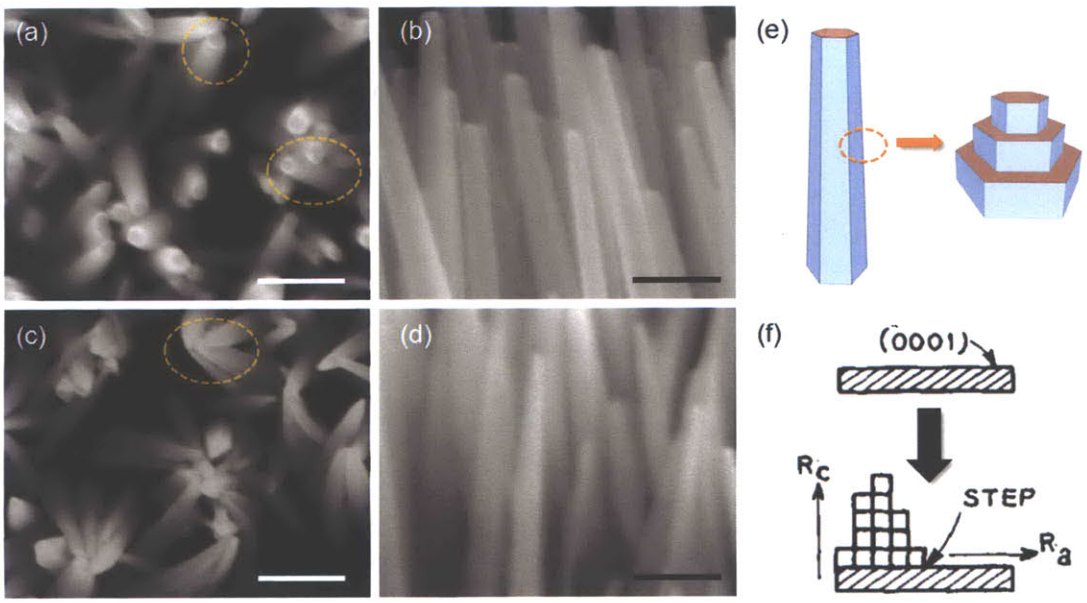


Figure 4.21. Top and 90 degree tilted SEM images of nanowire grown at two different chemical solutions. (a,b): Al 0.0006M, (c,d): Al 0.002M. Scale bar = 200 nm. (e) Crystal structure illustration of needle shape hexagonal nanorods. (f) Crevice-flawed growth of ZnO single crystals by step formation. Image taken from Laudise *et al.* [69].

From the previous AFM force-distance measurement and XPS analysis, it is clear that the surface potential of (0002) would be negative, and $(10\bar{1}0)$ would be positive under experimental condition. From the XRD, PL, and EDS, it is believed that there is no change in crystalline orientation or incorporation of cations under different experimental conditions. This validates the explanations of aspect ratio change with different additional cations by competing ion mechanism. Figure 4.21 shows summarized situation under different cations. When Al, In, or Ga is introduced (Figure 4.21a), majority of additional cation complexes are negatively charged, so suppress the ZnO growth in lateral direction by hindering negative charged Zn ion complexes attaching on $(10\bar{1}0)$ surface. Therfore, higher aspect ratio nanowires forms. When Ca, Mg, Cu, or Cd is present in the solution (Figure 4.21b), main additional cation complexes are positive, and suppress the positive Zn ion complexes attaching to (0002) plane by competing each other. However, negative charged additional cation complexes are minimal, so the growth in $<10\bar{1}0>$ would still exists and forming low aspect ratio plate shapes. Based on this rational understanding of ZnO nanostructure growth under cation addition, we believe that many interesting applications with optimal geometry can be possible in the near future.

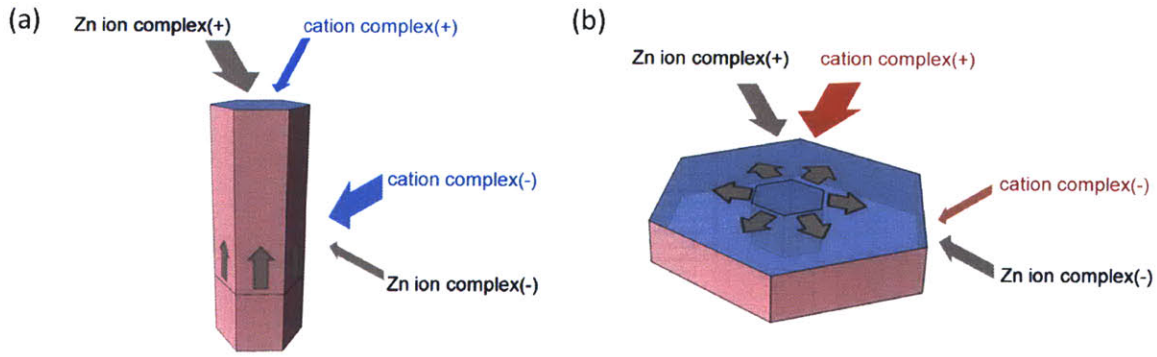


Figure 4.22. Schematic drawing of two different nanostructures forming under additional cations. (a) High aspect ratio nanowire growth under Al, In, or Ga addition. (b) Low aspect ratio nano plate growth under Ca, Mg, Cu, or Cd.

## 4.4. Conclusion

In conclusion, we demonstrated the morphology control of ZnO nanostructures from nano plates to extremely sharp nanowires using additional cations as a growth habit modifier. Using AFM and XPS analysis, crystal orientation dependent surface polarity of ZnO crystals under solutions were measured. Thermodynamic calculation gave the ion complex distributions with different polarities. Ion complex distribution and surface polarity of ZnO were used for the understanding the mechanism of ZnO nanocrystal growth under different cation additions. It is believed that growth direction is biased by electrostatic competition from cation-complexes that adsorb to the crystal in a certain surfaces more dominantly, thereby reducing zinc ion-complex adsorption and suppressing growth along that face. This rational controllability of ZnO aspect ratio has huge potential in improving the performances of the current nanowire devices including field emission display, energy harvester, solar cells [8-11], and also for new device development.

# Chapter 5 : Spatial Control of Nanowire Synthesis by Self Assembled Block Copolymer Templates

## 5.1. Introduction

Spatial control in the synthesis of semiconductor nanowires is of great interest because a device performance is highly influenced by position and spacing of nanomaterials. Among several semiconductor nanostructures, zinc oxide (ZnO) nanowire with direct band gap is one of the most important functional materials used for room temperature UV lasers, piezoelectric energy generators, photo detectors, gas sensors, and solar cells [4]. The conventional position control of hydrothermal nanowire growth is expensive and time consuming because electron beam lithography, which is a serial process, is required to form specific nucleation sites [70].

In this chapter, we report spatially controlled hydrothermal ZnO nanowire synthesis using self-assembled polystyrene-b-polymethylmethacrylate (PS-b-PMMA) diblock copolymer templates. The spacing is controlled by the length of block polymer chains. This scheme can be used for the nanowire synthesis with high precision tunable spacing in a massively parallel manner because the nucleation site is controlled by self assembly process.

## 5.2. Experiments

The schematic of the nanowire synthesis is shown in Figure 5.1. First, a thin ZnO seed layer was coated on a pre-cleaned substrate either by spin coating or RF sputtering followed by plasma treatment at 100 W with 10 sccm oxygen for 30 seconds. 1 wt% random brush copolymer (PS-r-PMMA-OH, Polymer Source) in anhydrous toluene was spin coated at 5000 rpm for 40 sec, then thermally annealed at 170 C for 2 days at $N_2$ environment. The substrate is then taken out and sonicated in anhydrous toluene for 5 minutes, forming a monolayer of random PS-r-PMMA polymer. On this substrate, 1~1.5

wt% PS-r-PMMA diblock copolymer (150k-b-57k, Polymer Source) in anhydrous toluene was spin coated at 4000 ~ 6000 rpm for 50 seconds to deposit 50 ~ 60 nm, followed by thermally anneal at 190 C for 2 days at $N_2$ environment. At this step, the block copolymer formed an ordered array of PMMA dots in PS matrix. After the sample was cooled down to room temperature, oxygen plasma at 100 W with 10 sccm was treated to etch PS and PMMA at different rates until PMMA dots were fully removed and only leaving PS matrix templates. This substrate was then introduced into supersaturated solutions with various ion concentrations ($ZnSO_4$, $NH_4Cl$, and NaOH), generating nanowires by hydrothermal reaction at temperatures from 60C to 80C only at ZnO seed layer exposed positions.

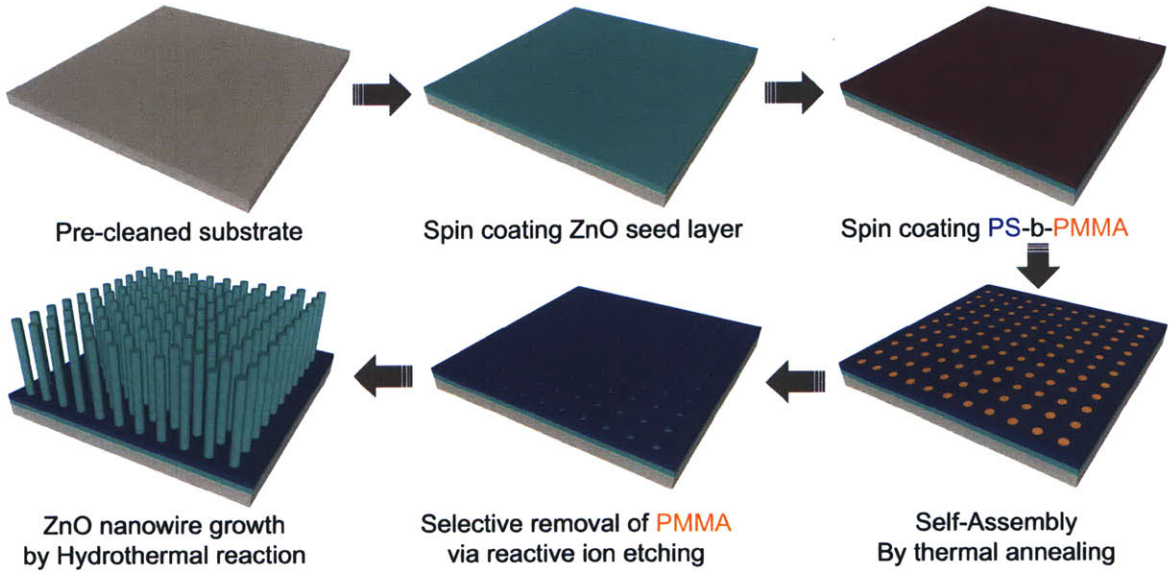


Figure 5.1. Procedure for spatially controlled ZnO nanowire synthesis. A PS-b-PMMA block copolymer thin film was spin coated on seed layer coated substrate and thermally annealed. The self assembled block copolymer patterns are oxygen plasma treated to remove PMMA and form PS templates. The substrate is transferred to supersaturated solution bath, and ZnO nanowires are synthesized only at seed layer exposed locations by hydrothermal reaction at temperature 60C~80C.

## 5.3. Results and discussion

### 5.3.1. Oxygen Plasma Etch Rate

For oxygen plasma etch rate measurement, 5 wt% PMMA and PS were diluted at anhydrous toluene, then spin coated to pre-cleaned Si wafer for etch test. Figure 5.2 shows etched thickness with different time at oxygen plasma treatment at 100W with 10 sccm $O_2$. Linear fit of data gives an etch rate of 0.54 nm/sec for PMMA and 0.27 nm/sec for PS respectively. Using this differential etch rate, PS-b-PMMA block copolymer can leave self assembled PS matrix only.

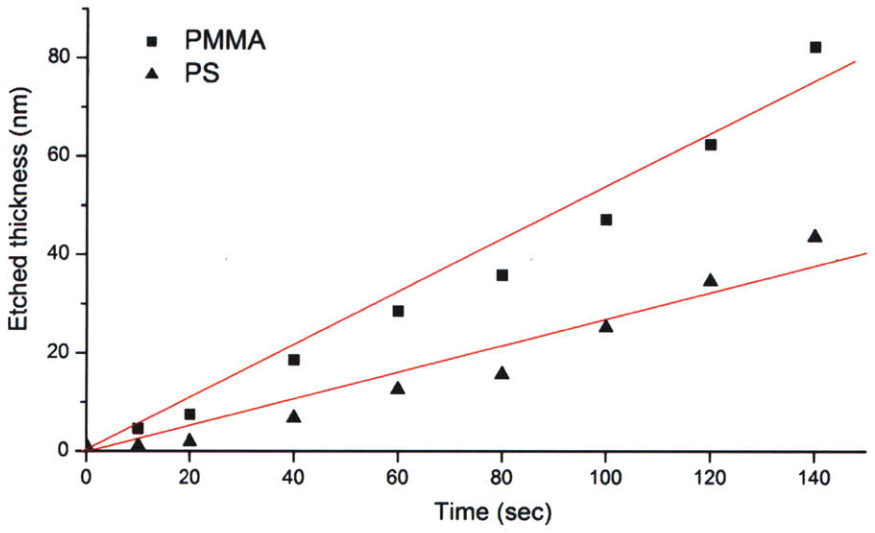


Figure 5.2. Plasma etched thickness for PS and PMMA respectively at 100W, 10 sccm 02 for various time. As seen from the data, PMMA has a higher etch rate than PS by a factor of 2.

### 5.3.2. Thickness dependence in self assembly

Controlling the thickness is critical for block copolymers assembling into desired shape. In this work, matrix with circular dots is necessary to expose the bottom ZnO seed layer for further nanowire growth with distant spacing. Generally, perpendicular alignment of lamellae or cylinders is created when the substrate has a surface energy

neutral with respect to each component by random copolymer brush formation. Depending on the thickness, PS-PMMA can either form cylinders lying parallel or vertical orientations [71]. To find the right condition, PS-b-PMMA samples with different thickness were tested (Figure 5.3). When the initial thickness of spin coated layer was 40 nm or below, self assembly was driven to form linear or wiggled PS arrays parallel to the substrate as shown in Figure 5.3(a). When the thickness was above 40 nm, block copolymer was vertically aligned and formed vertically aligned cylindrical arrays with minor misaligned shapes. Further experiments with ZnO growth, initial thickness of 50~60 nm was used.

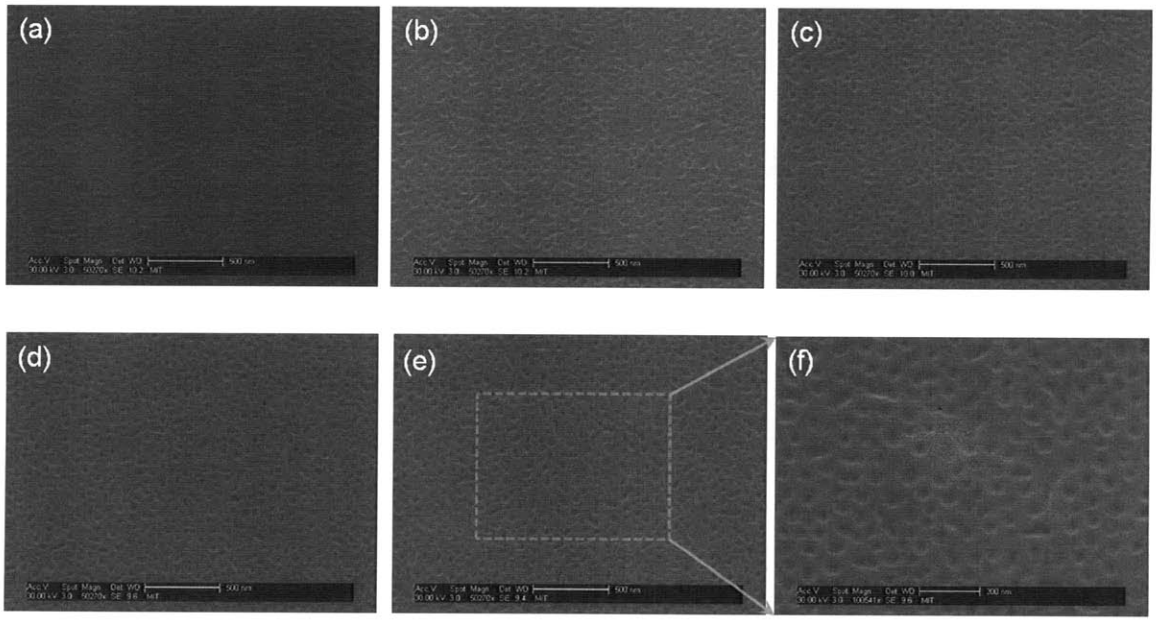


Figure 5.3. PMMA etched SEM image of PS-b-PMMA self assembly with different initial thickness. (a) 40nm, (b) 48 nm, (c) 56nm, (d) 63nm, (e) 68nm, (f) magnified image of (e).

### 5.3.3. ZnO nanowire growth on PS self assembled matrix

To check whether nanowires grow only at PMMA etched regions, we performed the growth with linear trenches first. Figure 5.4 shows the nanowires grown on the trench

PS templates. It is clear from Fig 5.4(b) that nanowires were synthesized only at trenched locations, not on the PS stripes. As a control test, we tried to grow ZnO nanowires on PS polymer coated ZnO seed layer substrate, but no growth was observed. This indicates that PS polymer is not energetically favorable to form heterogeneous nucleation and growth of ZnO. When growth time was increased to grow 1 ~ 2 um length nanowires with PS templates, nanowires got thicker than the initial hole diameter or trench width. Figure 5.4(c) and (d) shows the bottom of nanowires that has initial small size of growth matching PS matrix confinement, but thicker growth after certain height. It is believed that nanowires can grow laterally once the growth reaches above the PS confined structure. To compensate this situation, thicker matrix and wider dimension of self assembly would be necessary.

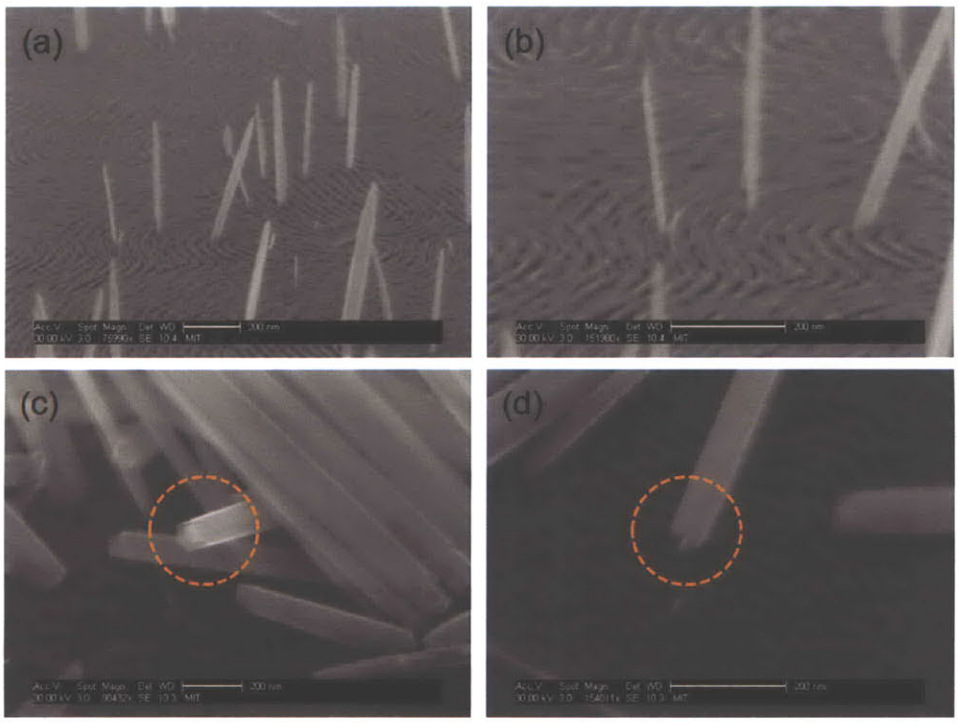


Figure 5.4. (a) and (b): ZnO nanowires synthesized with linear PS templates for growth location verification. (c) and (d): bottom of the nanowires indicating lateral growth above the PS template confinement.

Nanowire growth with circular PS templates is shown in Figure 5.5. Compared to nanowires grown directly on the seed layer (Figure 5a,b), nanowires on PS templates (Figure 5c,d) have lower density because it has smaller nucleation sites confined by PS matrix. The sample without a PS template had nanowires with a density of 125 ± 10 /um$^2$, whereas the sample with the PS template had a nanowire density of 62 ± 8 /um$^2$. With 150k-b-57k PS-b-PMMA block copolymer, center to center distance between each hole was 110 ~ 120 nm, so theoretical nanowire density should be 69.4 ~ 75.6 /um$^2$ assuming every hole is filled with nanowires with perfect spacing. The density value measured was close to the theoretical value, indicating successful nanowire growth in PS matrix. However, nanowire alignment with PS templates was poorer than higher density without the matrix. It is because the density of nanowires is low, so wires with random direction can have more chance to grow longer without being blocked by other vertical nanowires. If the substrate was a c-plane ZnO single crystal or has matching the lattices of c-plane ZnO, it would give vertical growth. Lateral thickness of nanowires seems slightly thicker also, probably because lower nucleation sites at same supersaturation condition would give larger growth with individual nucleus.

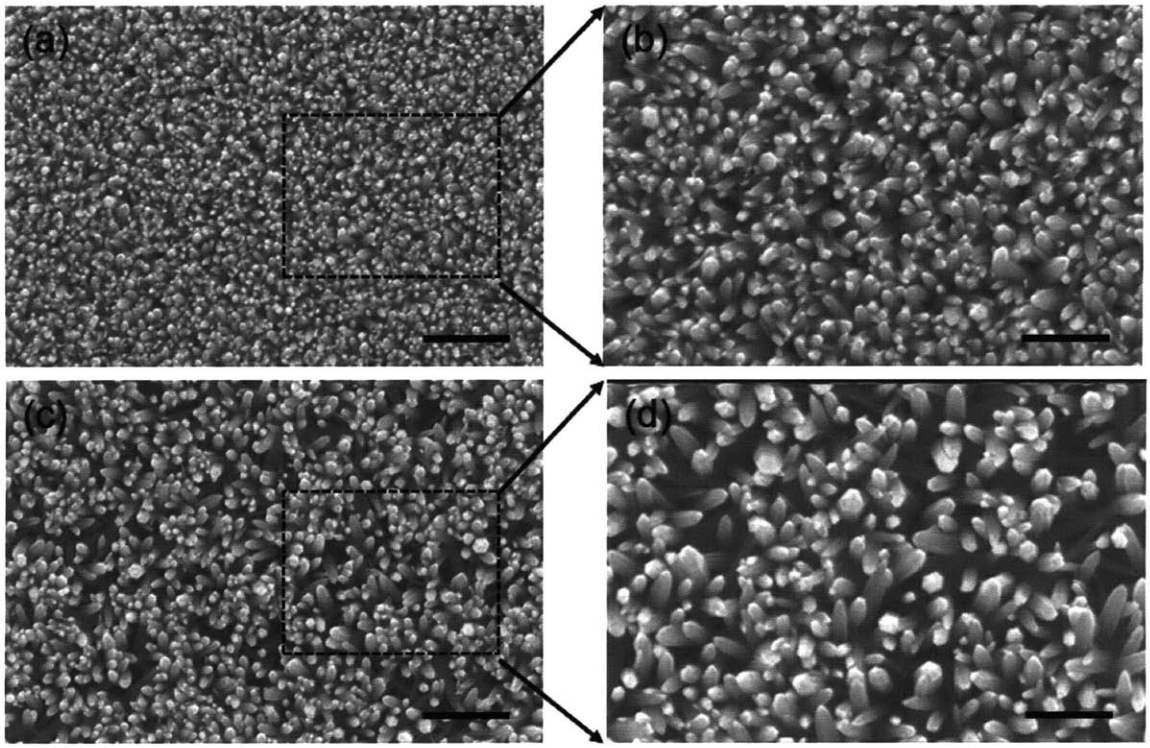


Figure 5.5. ZnO nanowire synthesized ($ZnSO_4$ 0.01M, $NH_4Cl$, pH 11 at 90C 2hrs) without PS templates (a,b) and with PS templates (c,d). Scale bar = 1 um (a,c) and 500 nm (b,d).

## 5.4. Conclusion

In conclusion, we demonstrated hydrothermal nanowire growth guided by self assembled block copolymer templates. Using PS-b-PMMA block copolymer, PS matrix with 40 ~ 50 nm holes was made by oxygen plasma etch. Nanowire growth solution was compatible with block copolymer layer without dissolving PS matrix within growth period. ZnO nanowires were successfully grown from the exposed region of the block copolymer template. Nanowires were grown to vertical direction initially, but it also expanded to lateral direction slightly once ZnO started to grow above the template. PS-b-PMMA with larger molecular weight may need to compensate the lateral growth

behavior, but it may not be easy to form self assembled PS/PMMA matrix in that large size during annealing process. Growth direction of nanowires was not perfectly vertical, because the seed layer was amorphous ZnO layer. To synthesize nanowires with nearly perfect spacing, c-axis oriented ZnO or other single crystal layer that matches with (0001) ZnO plane crystalline lattice would be necessary.

Many applications are possible using this method because it has several merits in commercialization such as low temperature solution process, parallel pattern formation, and parallel growth. This process may lead to development of high sensitivity photo detector sensor, flexible ultraviolet light emitting diode, and high efficiency photovoltaic cells.

# Chapter 6 : Microfluidic Control of Nanowire Synthesis

## 6.1. Introduction

In a hydrothermal ZnO nanowire synthesis, growth happens in a liquid phase at a low temperature < 100 C. Growth is governed by supersaturation degree described in a previous chapter. At an unoptimized condition, growth also happens in the solution by homogenous growth condition, leading less efficient growth per chemical consumption.

In this chapter, we report a combination of microfluidics and hydrothermal nanowire synthesis. By coupling chemical reaction with fluid dynamics, we demonstrate a spatial and temporal control of nanowire growth over various key parameters including ion concentration, pH, temperature, flow rates, and flow geometry.

Each individual growth channel allows nanowires to be synthesized with different properties in parallel with a single device. This technique was used for finding the optimized reaction parameters and creating nanowire channels with different aspect ratio by divalent or trivalent ion addition in the solution. Furthermore, we have achieved a growth rate that is an order of magnitude greater than in bulk solution synthesis under the same conditions by minimizing the depletion of reactant ions using continuous flow. Integrated control of reaction conditions enables the in-situ fabrication of nanowire-based electronics, as well as the study of nanowire growth kinetics in a highly controlled manner. Using the above technique, we have achieved a novel, continuous gradient control of the nanowire growth rate along the channel length. Also, 3D geometrically complex nanostructures were synthesized in various flow channels. We discuss fundamental studies on the coupling of reaction dynamics with fluid dynamics, as well as demonstrations in morphological control and algorithmic nanostructure growth on surfaces.

## 6.2. Experiments

Schematic of microfluidic nanowire synthesis is shown in Figure 6.1. After spin coating or RF sputtering a thin ZnO seed layer on a pre-cleaned substrate, molded Polydimethylsiloxane (PDMS) fluidic channels were attached to the substrate either by mechanically pressurized contact or plasma bonding. Supersaturated solutions with various ion concentration and pH ($ZnSO_4$, $NH_4Cl$, and NaOH) flew through each channel, and synthesized nanowires by hydrothermal reaction at temperatures from 40 C to 80 C controlled by a Peltier stage.

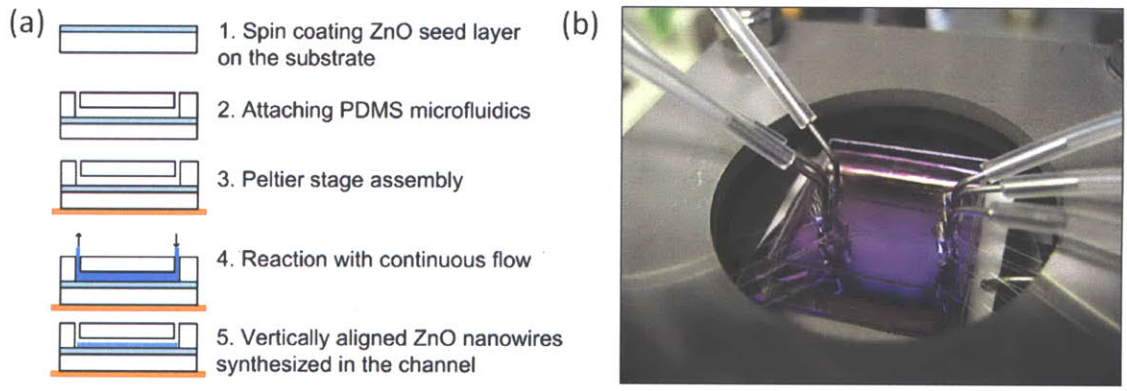


Figure 6.1. Schematic diagram of microfluidic ZnO nanowire synthesis (a) and prepared device unit with three parallel channels (b).

In detail, optically patterned SU-8 was used as a mold for PDMS layer. After spin coating SU-8 2050 (Microchem) at 1000 rpm (for 80 um height) for 40 seconds on the pre-cleaned 4" Si wafer (Wafernet), the substrate was prebaked at 65 C for 10 minutes, followed by 90 C for 30 minutes on a hot plate. Using transparency mask (Pageworks) designed with Autocad, the SU-8 photoresist was exposed at UV (INTELLI-RAY 400, Uvitron) with 50mW/cm$^2$ for 40sec, and post baked at 65 C for 1 minute, followed by 95 C at 10 minute. Finally, the wafer was developed by SU-8 developer with active agitation

for 10 minutes, then washed with DI water and dried under nitrogen.

For replicating SU-8 master mold, approximately 40 g of liquid PDMS pre-polymer (GE, RTV 615) at a component A to B ratio of 10 : 1 was poured onto the mold to a thickness of 1 cm, followed by curing in a convection oven at 80 C for 3 hours. The PDMS layer was then peeled off from the master, and individual device was cut off with a razor blade. Holes for the inlets and outlets were cored with a 0.75 mm beveled needle (Harris Uni-Core). This PDMS was briefly cleaned with IPA again and put on top of a ZnO seed layer coated substrate. Custom made holder (laser cut / waterjet parts) was used to pressurize PDMS / substrate on top of peltier stage (FerroTec) connected to microcontroller (Watlow).

Flexible tubing (Excelon Micro-Line, 0.75 mm ID) was connected to PDMS inlets and outlets by intermediate stainless steel tube (New England Small Tube Corp., 0.082 mm OD). Tubing was connected to 1 ~ 5 mL syringe (Norm-Ject) filled with supersaturated solution. Flow rate was controlled by mechanical syringe pump (KDScientific). After microfluidic nanowire synthesis was finished at fixed time and flow rate, PDMS layer was detached from the substrate, and cleaned with DI water, followed by nitrogen dry.

Growth of nanowires was examined using Philips-FEI XL30-ESEM field emission scanning electron microscopy (SEM) with a secondary electron detector in normal high vacuum mode. Simulation was performed by Comsol Multiphysics finite element software with a Matlab code.

## 6.3. Results and discussion

Nanowire growth along the Microfluidic channel is shown in Figure 6.2. Nanowires would grow by heterogeneous nucleation and growth through supersaturation as discussed in the previous chapters. Top down SEM shows nanowires grown only at the defined linear region, indicating easy patterning of vertical nanowires at specific location guided by microfluidic channels. Nanowire morphology and density was similar to the bulk system. Tilted view SEM showed that nanowires grow vertically along the interface between PDMS and ZnO solution.

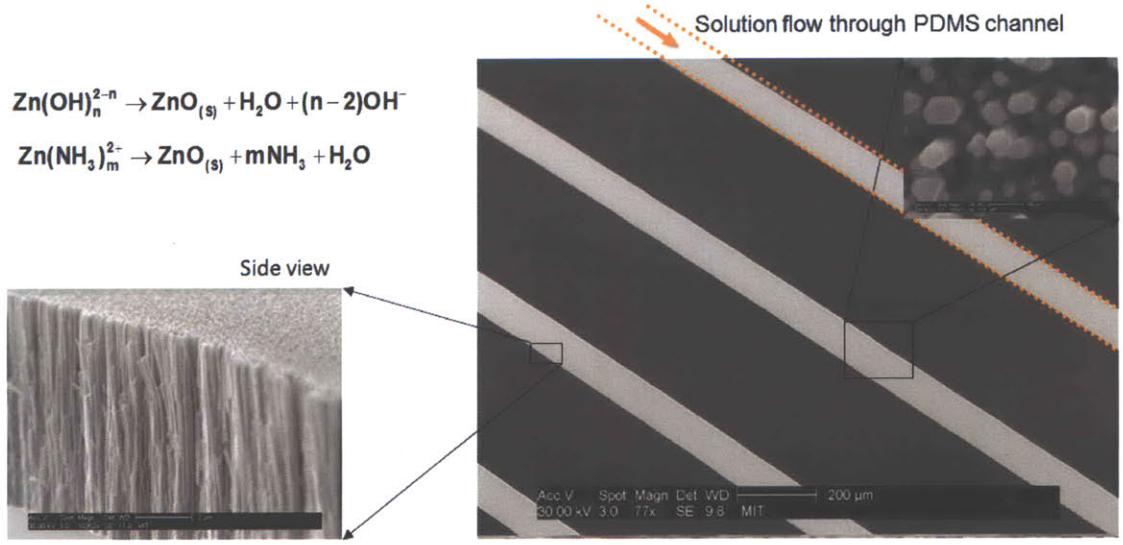


Figure 6.2. SEM image of nanowires synthesized on top of Si substrate. PDMS was detached for SEM analysis on top and side view.

The microfluidic synthesis with chemical solution is analogous to chemical vapor deposition (CVD) process (Figure 6.3). Both systems involve chemical reaction and flow of either solution of gas. It would have a diffusion limited reaction condition (when reaction is fast enough), or reaction limited condition (when diffusion is fast enough). However, there are distinctive differences between microfluidic synthesis and CVD

synthesis. In CVD, deposition generally occurs on all surface area unless the surface is prepatterned for selective deposition. In microfluidic synthesis, deposition occurs only at fluidic channels, so site specific growth is automatically achieved. Also, parallel growth with different materials can happen at the same time, compared to CVD methods that require multiple lithography and deposition steps to define each material section.

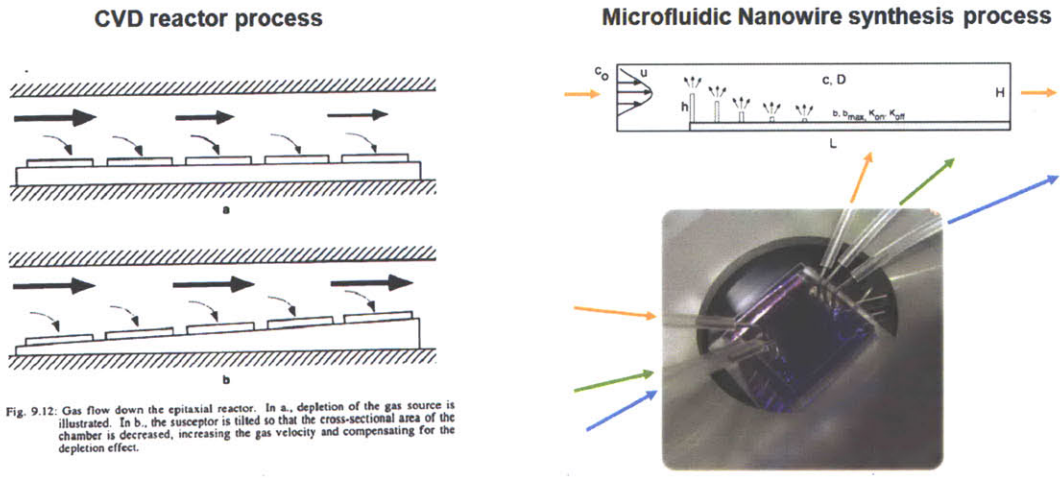


Figure 6.3. Comparison between chemical vapor deposition (CVD) process and microfluidic nanowire synthesis. CVD image taken from Plummer *et al.* [72].

To evaluate the condition for the nanowires under microfluidic system, a serpentine structure of a microfluidic channel with 100 um width, 80 um height, and 35 cm length was fabricated. Nanowire growth was performed with this fluidic channel at a fixed supersaturation solution ($ZnSO_4$ 0.01M, $NH_4Cl$ 0.3M, pH 11 by NaOH) and a fixed flow rate of 0.3 mL/h for 5.5 hrs. Only variable was a reaction temperature from 40 C to 60 C. Figure 6.4 shows the drawing of microfluidic channel, and SEM image of nanowire grown on Si substrate at 45 C. After detaching the PDMS layer, nanowire growth heights with respect to the distance from the inlet were plotted after 80 degree tilted height measurement with SEM.

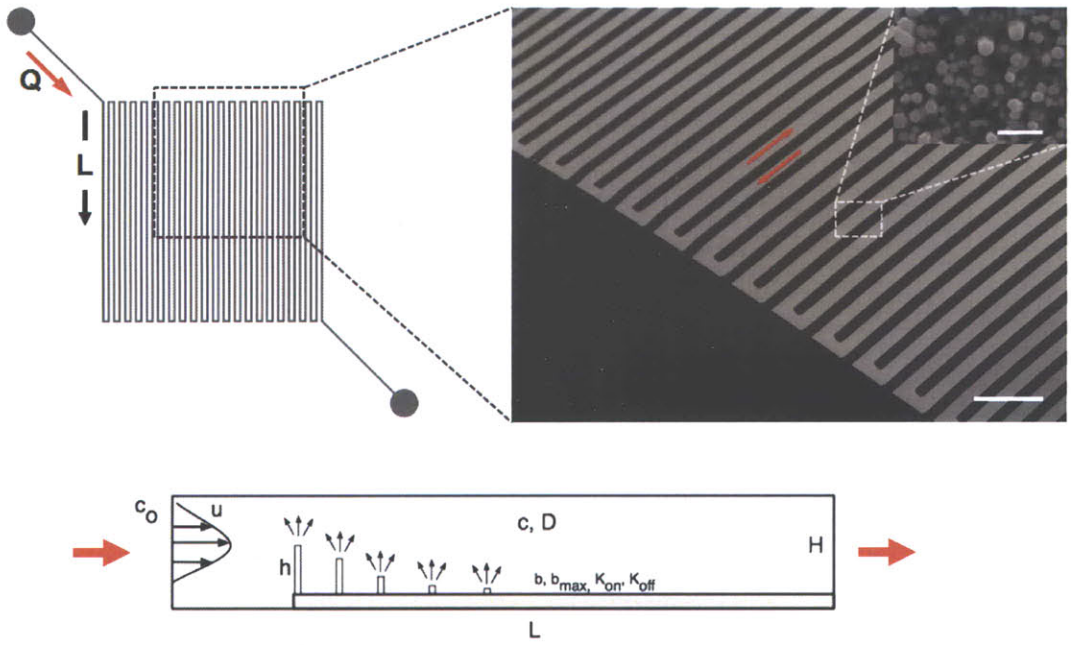


Figure 6.4. Microfluidic channel drawing and SEM image of nanowires grown on Si substrate. The PDMS layer is detached from the substrate for SEM characterization. Scale bar = 500 um. Inset scale bar = 500 nm.

Figure 6.5 (a) shows the result with different positions. It is clear that the growth was dominant at the inlet port, and decreased as it goes further to the outlet. At these temperature conditions and flow rate, the process seems to follow the diffusion limited regime because the growth varies with location, and closer to the source has higher growth rate. This is growth decay along the distance is similar to CVD process with diffusion limited regime. In CVD, the substrate is tilted to compensate the source depletion by decreasing the cross sectional area and increasing gas velocity (Figure 6.3).

Figure 6.5 (b) shows temperature dependent nanowire growth at a fixed distance from the inlet. At temperatures below 40 C, no growth was observed within a reaction period, indicating not enough energy to overcome activation barrier to transform from solution phase to solid phase. Growth rate was maximum at 50 C, and lower towards both 40 C and 60C at any locations. This result is different from the general CVD process. In

CVD, surface reaction and gas transport are both proportional to temperatures. The surface reaction can be described by thermal activated process (Arrhenius equation, $\exp(-Q_r^*/KT_{sub})$, and gas transport can be de described by diffusion process (gas, $D \propto T_{sub}^{3/2}$, for $T_{gas} \approx T_{sub}$). In the microfluidic system, the distance dependent experiments empirically follows mass transport limited regime (Figure 6.5 a), so the growth should follow diffusion constant-temperature relationship (Stokes-Einstein relation, $D = K_b T/6\pi\eta r$) in ideal condition. In solution system, heterogeneous growth and homogeneous growth are both present at an elevated temperature. However, what we measured as a ZnO height only accounts for the heterogeneous growth. From 40C to 50 C, nanowire growth increase can occur either from higher diffusivity of Zn ion complexes from the solution to the substrate or chemical reaction increase with temperature increase. In case of 50 C to 60 C or higher, growth decreases with temperature increases. In higher temperature, homogenous nucleation and growth would be enhanced, so measured growth decreases even though the total ZnO growth in the system, which is an added value of homogeneous and heterogeneous nucleation and growth, may be higher under the assumption that temperature increase will enhance the growth by increase of diffusivity and reactivity of the chemicals.

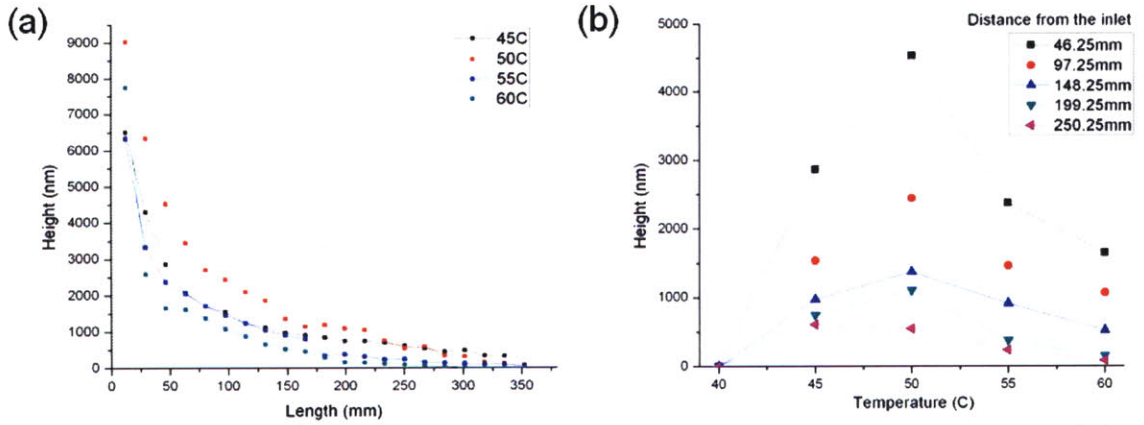


Figure 6.5. (a) Experimental data of ZnO nanowires height versus distance from the inlet. (b) ZnO nanowire height versus temperature at fixed distances.

Flow rate dependent nanowire growth is shows in Figure 6.6. Individual fluidic channel has 100 um width, 80 um height, and 15 mm length. Reaction was performed at fixed concentration ($ZnSO_4$ 0.01M, $NH_4Cl$ 0.3M, pH 11 by NaOH) at 50 C. Flow rate was varied as 0.2 mL/h, 0.8 mL/h, and 1.2 mL/h for each inlets. At low flow rate, exponential decay of growth with respect to the distance from the inlet is prominent, indicating the synthesis condition is under diffusion limited regime. However, distance dependent growth change decreases as flow rate increase, and almost flat when the flow rate was 1.2 mL/h. It is believed that higher flow rate decreases the boundary layer of the mass transport. Also, solution would be replenished faster, so it could and minimize supersaturation decrease by consumption on the surface (or growth). Therefore, optimized condition may give more even growth with respect to the flow distance if necessary. Unfortunately, experiment with higher flow rate than 1.2mL/h was not practical because of the pressure build up was too much to create constant flow rate using syringe pump system.

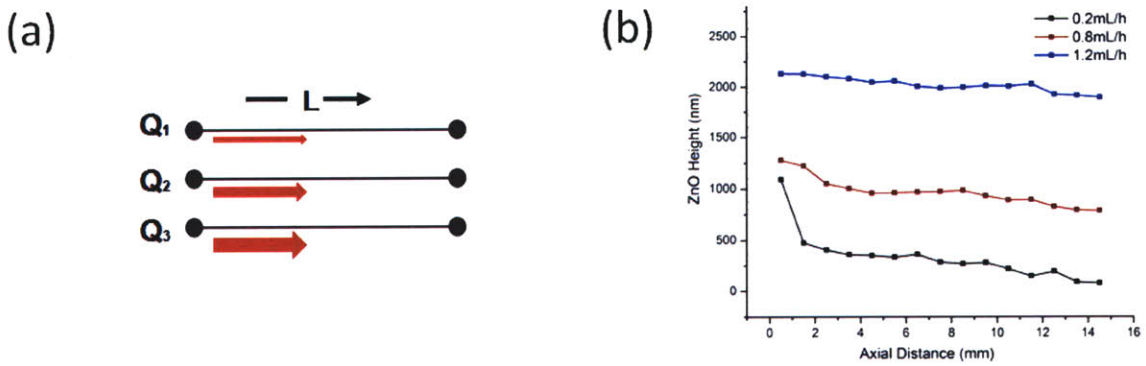


Figure 6.6. Microfluidic channel drawing (a) and experimental growth data with ZnO nanowires height versus distance from the inlet with different flow rates (b).

Using numerical simulations, we analyzed the growth behavior of ZnO nanowires under microfluidic system. Figure 6.6a shows the equations used for the finite element modeling. Concentration, pressure, and adsorption have time and position dependence. Surface reaction was based on the adsorption model. In case of ZnO synthesis, there are always available sites for the ions to form crystals at any surface, so the available sites for the Langmuir adsorption was set to be a constant. Since several parameters on this specific case are not readily available, we put values reported with close conditions for adsorption coefficients, diffusivity, and viscosity [73-74]. Time dependent surface concentration with respect to distance is shown in Figure 6.7b. The simulation was performed only close to the inlet port because of mesh condition in finite element model. At fixed time, surface concentration decreases along the distance, so the growth would follow the same shape. The decay is not as prominent as we observed from the experiment in Figure 6.5, and we believe it would be similar if we can calculate further along the axis. At an initial stage, highest adsorption happens at the inlet with high decrease along the distance. As time increases, actual adsorbed ions participating the growth decreases around the inlet, and getting close to the value at the further location

(Figure 6.7c). We believe that this decrease comes from the diffusion of ions at the initial port to further location. More detailed simulation and experimental analysis would be necessary to fully understand chemical nanowire synthesis reaction and fluid dynamics.

(a)

Incompressible Newtonian Fluid with density $\rho$ and viscosity $\mu$

$$\rho\left(\frac{\partial u}{\partial t}+u\cdot\nabla u\right)=-\nabla p+\mu\nabla^2 u$$

$$\nabla\cdot u=0$$

diffusion-Advection equation with local concentration c

$$\frac{\partial c}{\partial t}=D\nabla^2 c-u\nabla\cdot c$$

Langmuir surface adsorption model for growth kinetics

$$\frac{\partial C_s}{\partial t}=K_{ads}C\theta_0-K_{off}C_s$$

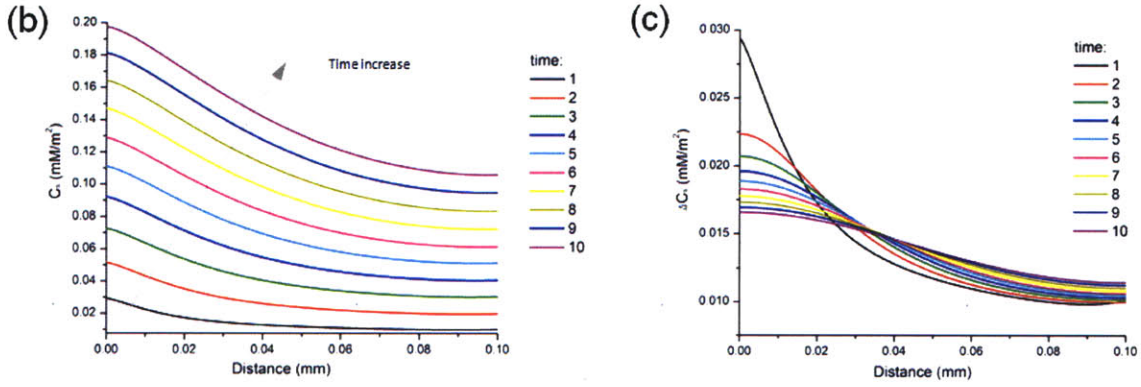


Figure 6.7. (a) Equations used for finite element analysis assuming Langmuir surface adsorption model for nanowire growth kinetics. (b) Time dependent cumulative surface concentration vs. distance from the inlet plot from the simulation. (c) Time dependent surface concentration vs. distance.

Microfluidic nanowire synthesis was also tested with more complex geometry. Figure 6.8 (a) shows fluidic channel designed for study. Linear channel and fins along the line of the channel were designed to separate the effect of convective flow and diffusive flow of the ion species under microfluidic system. Along the direction of fins ($L_1$), only diffusion of Zn ion species is present. At this case, ZnO growth with respect to the distance was similar to the diffusion from a finite source at the interface (Figure 6.8b). Color gradient along $L_1$ shows the height changes with different fins are almost identical,

indicating only diffusion is dominant factors for the growth along $L_1$. Interestingly, no growth was observed at the branch regions (Figure 6.8d), and it is still not clear how it happens. It may be related to porous structure of PDMS, fluid geometry, and others. More detailed experiments and simulation may give an insight on the coupling of chemical reaction and fluid dynamics.

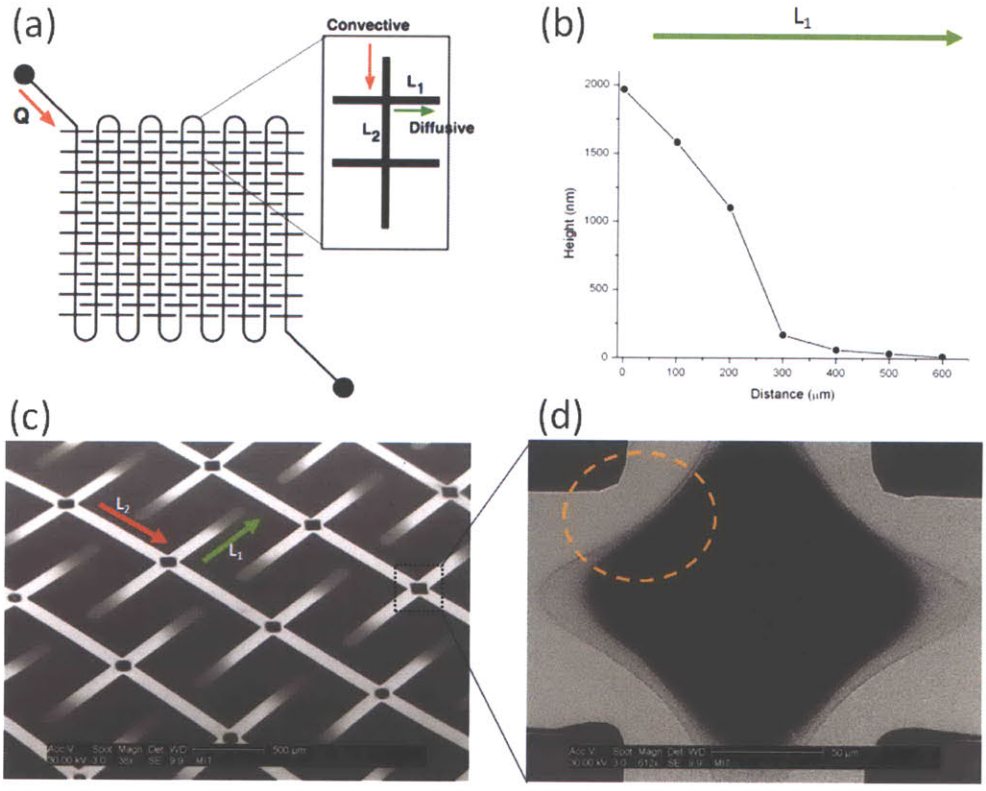


Figure 6.8. (a) Complex microfluidic channel design for analyzing diffusive ($L_1$) and convective ($L_2$) flow terms separately. (b) Experimental nanowire height data along with $L_1$ at branched diffusive region. (c) SEM tilted image of nanowires (white) on Si substrate. Gradient color change indicates height decrease along $L_1$ axis. (d) Non growth region at the center of the branches.

## 6.4. Conclusion

In conclusion, we demonstrated ZnO nanowire synthesis in a microfluidic system with a controlled manner. The synthesis of vertically aligned zinc oxide (ZnO) nanowires in a microfluidic device that allows precise control over key parameters in hydrothermal synthesis and the creation of complex geometries via fluidic control. This technique facilitates rapid screening and optimization of growth conditions, and the *in-situ* fabrication of morphologically diverse nanostructure-based integrated devices. We have determined that optimized conditions in a microfluidic device yields growth rates an order of magnitude greater than in bulk solution with a minute fraction of the reagent consumption. Lastly, by physically coupling growth and transport dynamics of reactants in a continuous flow microfluidic reactor, we demonstrated the programmed synthesis of complex geometrical patterns within enclosed geometries. Thus, this simple yet innovative methodology may lead to *in-situ* patterned- and synthesized, integrated devices with highly tunable geometrical, electrical and optical properties.

# Chapter 7 : Applications

## 7.1. Nanowire Field Emission Device

### 7.1.1. Background

Field emission (FE) is an emission of electron induced by external electric fields. The theory of field emission was explained by a quantum mechanical tunneling behavior. When the external field is high enough, the triangular energy barrier width gets smaller as shown in Figure 7.1, electron escape probability increases exponentially. This general concept of tunneling was proposed by Fowler and Nordheim [75] followed by several modified mathematical models to explain the experimental behavior.

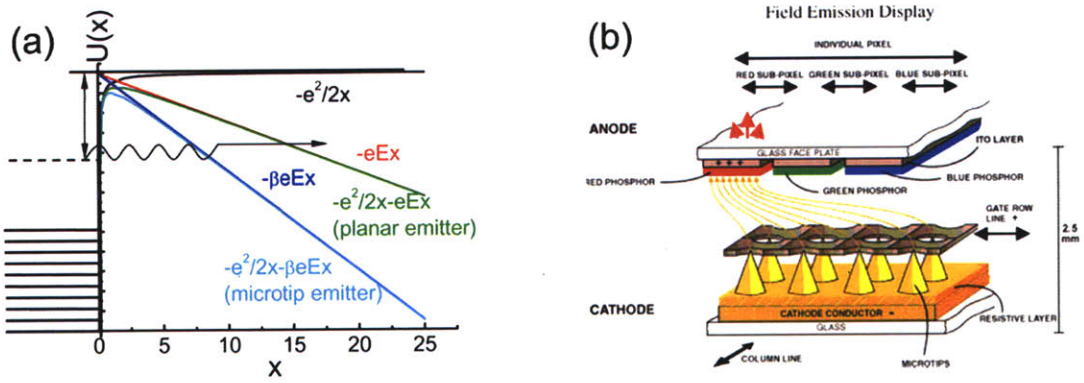


Figure 7.1. (a) Schematic diagram of field emission barriers for a planar and a microtip emitter [76]. The microtip emitter has a higher probability of tunneling behavior than the planar emitter. (b) Schematic structure of a field emission display device [77]. Electrons extracted from several field emission micro tips are accelerated to individual phosphor color pixels, creating lights for display system.

If the surface has a high aspect ratio tip, a localized field around the tip increases compared to the flat surface with the same potential difference. This is called a field enhancement factor ( $\beta$ ). In general rule of $\beta$, the following relationship is valid [78],

$$\beta = \frac{h}{D}\left(1 + \frac{d}{r}\right) \tag{1}$$

Where $h$ is length of the tip, $r$ is radius curvature of the tip, $d$ is gap between tip and counter electrode, $D$ is gap between bottom of the tip to the counter electrode (Figure

7.2). Researchers have used this effect to make efficient field emitters for scanning electron microscopy, scanning ion microscopy, and field emission display.

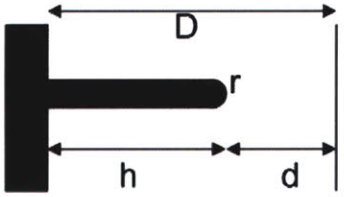


$$\beta = \frac{h}{D}(1 + \frac{d}{r})$$

Figure 7.2. Relationship between tip geometry and field enhancement factor [78].

Field Emission Display (FED) is a flat panel display that has parallel electron emission sources for exciting colored phosphor in each pixel to create color display. Spindt *et al.* used micro fabrication technique to create molybdenum cone arrays [79]. Recently, carbon nanotubes were used as field emission source because of its natural high aspect ratio structures. For the first time, Samsung Electronics demonstrated fully sealed carbon nanotube FED in 1999 [80]. However, carbon nanotubes are still not an optimal material for FED yet because of its stability issue of electron emission current by degradation from burning out and destructive arching in a vacuum. To solve the problems of carbon nanotubes, researchers have worked on finding different nanowires for FED, including gold, copper, ZnO, ZnS, $WO_3$, Si, and others [81].

### 7.1.2. Introduction

The vertically aligned morphology of ZnO nanowires has shown great advantages in manipulation and device assembly within the nanometer regime. Among them, field emission is one of the most important applications because the electron emission efficiency can be highly improved by high aspect ratio of structures. Several people demonstrated the field emission characteristic of ZnO nanowires [8, 82], but the threshold

voltage, indication of extraction efficiency, was not close to carbon nanotube (CNT) field emission devices. By rationally controlling the tip geometry with cation addition during nanowire synthesis, the performance of ZnO nanowires as a field emission device was evaluated.

### 7.1.3. Experiments

For Nanowire field emission measurement, ITO glass (Delta Technologies) was pre cleaned, followed by 30 nm thick ZnO seed layer deposition by RF sputtering (150W, 20mTorr, 12 sccm Ar). Different morphology nanowires were synthesized on the substrate with various solution bath conditions similar manner described in chapter 4. All basic solution was prepared with zinc sulfate ($ZnSO_4$, 0.01M) and ammonium chloride ($NH_4Cl$, 0.3M) in 100 mL deionized solution. Five different cation sulfate ($Al_2(SO_4)_3$ : 0.001M, 0.002M / $CdSO_4$ : 0.001M, 0.002M / No addition) was introduced to each solutions, then sodium hydroxide (NaOH) was added to adjust pH to 11. The substrates were introduced to each bath to grow nanowires on the ITO substrates for 20 hrs. After removed from the solution, the substrate was washed with DI water followed by nitrogen dry. To expose ITO layer for IV characterization, corner ZnO nanowire and ZnO seed layer was etched by diluted HCl (2M) with cotton swap, then cleaned with acetone.

Schematic of field emission electrical measurement setup is shown in Figure 7.3. Counter electrode was prepared with 1/16" diameter tungsten tip (McMaster Carr) covered with Teflon on the side for electrical insulation. This electrode was attached to three axis positioner (Newport) with micrometer for the high precision spacing adjustment. This custom built setup was introduced in vacuum chamber ($5 \times 10^{-6}$ mbarr), and high voltage measurement unit (Keithley 237) was connected through electrical feed

through for IV characterization.

For phosphor light emission excited by field emitted electrons, nanowire grown ITO substrate and P22 phosphor coated ITO substrate (Lexel Imaging Systems Inc.) were sandwiched with 190.5 um spacer (Precision Brand) in a vacuum chamber (5 x $10^{-6}$ mbarr), then high voltage supply (Stanford Research systems, PS350) was used for field emission. Images under operation were captured by Canon Rebel XTi DSLR camera with EF 24-70mm f/2.8L USM macro lens.

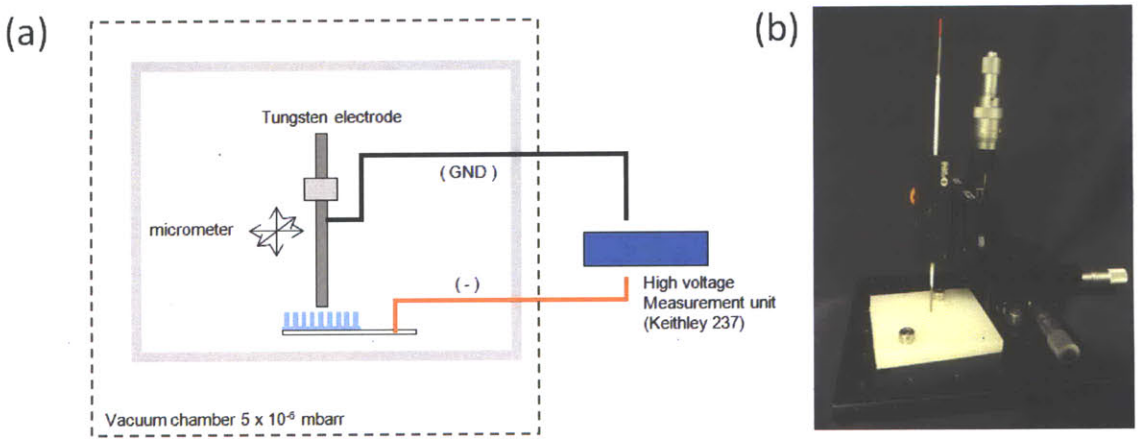


Figure 7.3. Schematic of field emission measurement setup for ZnO nanowire device in vacuum system (a) and three axis measurement unit (b).

### 7.1.4. Results and Discussion

To investigate nanowire geometry and aspect ratio dependent field emission, Spacing was fixed to 30 um between the tip of the nanowire/nanoplate and the tungsten counter electrode.

Figure 7.4 Shows field emission measurement with five different nanowire / nanoplate grown on ITO with Al 0.002M (aspect ratio: 103.1), Al 0.001M (aspect ratio: 101.9), no addition (aspect ratio: 44.9), Cd 0.001M (aspect ratio: 10.1), and Cd 0.002M (aspect ratio: 1.3). As expected from field enhancement factor described before (Figure

7.2), field emission was enhanced with the samples with higher aspect ratio. In fact, ZnO nanowire with Al addition creates sharpen tip, so real tip diameter (r) is much smaller than diameter measured at the middle of the nanowire, so d / r ( length / tip diameter) would be much higher than aspect ratio stated above. This would be the reason why Al 0.002M sample and Al 0.001M sample have huge differences in field emission even though aspect ratio values are in a similar range. Turn on field values (reaching 10 $uA/cm^2$) were 0.45 V/um (Al 0.002M), 1.77 V/um (Al 0.001M), 3.70 V/um (No Addition), 6.18 V/um (Cd 0.001M), and out of range (Cd 0.002M). For Al 0.002M, the value is similar or smaller to the carbon nanotube (CNT) field emitter that has a value of ~ 0.8 V/um [83].

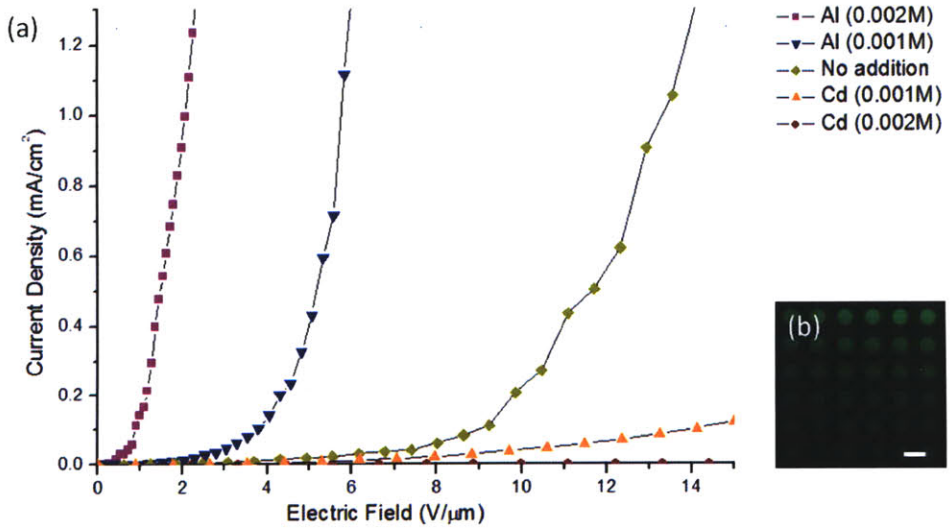


Figure 7.4. (a) Field emission measurement data for five different nanowire samples. (b) Green light emission from P22 phosphor excited by field emitted electrons from nanowires. Scale bar = 1 mm.

Electron emission under an applied field can be described by Fowler-Nordheim (FN) equations,

$$J = A\frac{E^2}{\varphi}\exp\left(-\frac{B\varphi^{3/2}}{E}\right) \quad (2)$$

where J is the current density ($A/cm^2$), E is the electric field (V/um), A and B are constants ($A = 1.56 \times 10^{-10}$ $A{\cdot}eV/V^2$, $B = 6.83 \times 10^3$ $eV^{-3/2}$ V/um), and $\varphi$ is the work function of ZnO (5.3 eV) [8, 84-85]. In case of nanowires, other researchers have reported slightly lower work function value of $4.7 \pm 0.2$ based on a photoelectron spectroscopy measurement. The reduction in $\varphi$ maybe related to faceting of nanowires, surface variation in stoichiometry, and others. However, no value change was observed within diameter variation of 80 nm ~ 200 nm [86-87] .

Local electric field can be described as,

$$E = \beta V/d \quad (3)$$

Where $\beta$ is the field enhancement factor, V is the applied voltage, and d is the spacing between electrode and nanowire tip.

Arranging equation (2) with (3) gives the following FN plot,

$$\ln\left(\frac{I}{V^2}\right) = \ln\left(\frac{A\beta^2}{d^2\varphi}\right) - \frac{B\varphi^{3/2}d}{\beta V} \quad (4)$$

The slope of the FN plot (k) is determined by field enhancement factor ($\beta$) and work function ($\varphi$).

$$k = -B\varphi^{3/2}d/\beta \quad (5)$$

Therefore, we can calculate the field enhancement factor from the FN plot by measuring the slope.

Previously measured field emission with five different nanowire samples were

plotted again with FN curve (Figure 7.5a). Different aspect ratio had different slopes, indicating different field enhancement factors. From the slopes of FN curve, field enhancement factor for each nanowire device was calculated (Figure 7.5b). As expected, highest aspect ratio (Al 0.002M, h/d = 103.1) showed highest field enhancement factor (28246.6). Cd 0.002M device did not show any enhancement because it did not give field emission under our experimental range. Interestingly, field enhancement factor should be proportional to h/r approximately, but the calculated value was one to two orders higher than the aspect ratio. It would be because the real radius of the tip is smaller than the diameter in the middle of the nanowires, so the field enhancement would be higher than aspect ratio value. Generally reported ZnO nanowire $\beta$ is in the range of 1000 ~ 2000, similar to what we observed with no additional cations (2082.9). In case of CNT, $\beta$ from the literature is in the range of 1000 ~ 8000, with a maximum value of 35000 [88-89]. The remarkable value of $\beta$ (28246.6) of our Al added sample seems to be related to the morphology of the wires. Several researchers reported that tapered cone shape nanostructures showed higher $\beta$ than flat top nanowire shape [90]. In our case, Al addition tapers the tip, thereby decreasing the radius of the tip. It also slightly increases the spacing between individual wires, thereby minimizing the screening effect between wires. Maximum $\beta$ reported with ZnO was ~ 41,100 with controlled density and nanowire length [91] . We believe that optimized ZnO nanowires by rationally controlling the morphology, height, and spacing may give higher field enhancement factor that would be useful for various field emission devices.

(a)

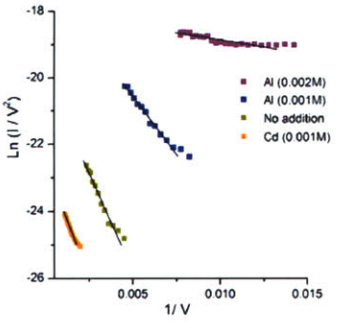


(b)

| Nanowires | Slope of FN curves (k) | Field enhancement factor (β) |
|---|---|---|
| Al 0.002 M | -86.0 | 28246.6 |
| Al 0.001 M | -489.6 | 4962.4 |
| No addition | -1166.5 | 2082.9 |
| Cd 0.001 M | -1363.6 | 1781.8 |
| Cd 0.002 M | N/A | N/A |

Figure 7.5 (a) Fowler-Nordheim (FN) plots for different aspect ratio ZnO nanowire samples. (b) Slope of FN curves field enhancement factor for ZnO nanowire samples.

| sample | Turn on Field (v/um) | Field enhancement factor (β) |
|---|---|---|
| Al 0.002 M | 0.45 | 28246.6 |
| Al 0.001 M | 1.77 | 4962.4 |
| No addition | 3.70 | 2082.9 |
| Cd 0.001 M | 6.18 | 1781.8 |
| Cd 0.002 M | N/A | N/A |
| Controlled ZnO NW[a,b] | 1.1, 0.7 | 9804, 41100 |
| Controlled CNT[c,d] | 0.2 | 18820, 35000 |
| Multiwall CNT[e] | 0.8 | 8000 |
| $SnO_2$ nanobelt[f] | 2.3 | 1796 |
| ZnO nanoneedle array[g] | 4.1 | 1134 |
| AlN nanorod array[h] | 8.8 | 565 |

Figure 7.6 Turn on field (to reach 10 uA/cm$^2$) and field enhancement factors of the ZnO nanowires samples and others. [a]Reference [83]. [b]Reference [91]. [c]Reference [92]. [d]Reference [89] . [e]Reference [93] . [f]Reference [94]. [g]Reference [95]. [h]Reference [96].

### 7.1.5. Conclusion

In conclusion, field emission properties of variable aspect ratio nanowires were successfully evaluated. Varying only the competing ions in the inorganic batch process, we demonstrated synthesized low-aspect ratio platelets, as well as high-aspect ratio

nanowires sharpened to create field-emitters with emissivity equivalent to carbon nanotubes. Being oxide instead of carbon based material may solve the problems of stability issue of current carbon nanotube system. As seen from the data, this field emitter may be useful for high efficiency field emission display [80], portable x-ray source machine [97-98], parallel miniature electron beams [99-100], and others.

## 7.2. Nanowire embedded Alternative Current Electroluminescent Device

### 7.2.1. Background

A thin-film electroluminescent device consists of five stacked layers, conductor / insulator / phosphor / insulator / conductor / substrate, as shown in Figure 7.7. The Phosphor layer is generally polycrystalline zinc sulfide (ZnS) doped with atoms such as Mn, Ce, and Tb with concentration of an order of 1 mol%. The insulator layers are generally barium titanate ($BaTiO_3$), silicon oxide ($SiO_2$), or aluminum oxide ($Al_2O_3$) behaving as capacitors. At least one of the conducting layers is transparent for the light emission to be possible from overlapped electrodes.

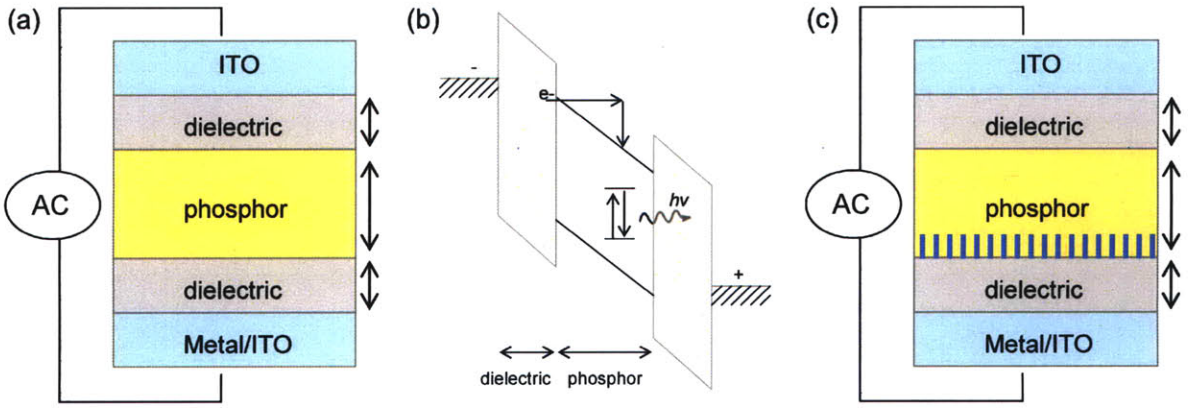


Figure 7.7. (a) Schematic diagram of an Alternative Current Thin Film Electroluminescent (ACTFEL) Device. (b) Band structure of ACTFEL multiple layers when a pulse voltage is applied. (C) Proposed structure of nanowire embedded ACTFEL device. ZnO nanowires are embedded between the electrode and the phosphor for increasing light emission efficiency by the field enhancement effect.

To create light emission from the phosphor layer, a pulse voltage is applied over the two conductors. If the voltage ($V_a$) is below the threshold voltage ($V_{th}$), the phosphor layer behaves as an insulator. When $V_a$ is higher than $V_{th}$, electrons at the phosphor – insulator interface of the negative potential are released, and start being accelerated to the

opposite side of phosphor layer. If the electric field is high enough, the accelerated electrons can excite the dopant atoms. When the excited dopant atoms relax from the excited states to the ground states, it can emit a photon. The spectrum of photon is determined by available energy levels of the dopant atom. Since the electrons cannot move through the other side of insulator, they accumulate at the interface between insulator-phosphor and create a reverse electric field. These trapped electrons prohibit the further electron transfer. When reverse voltage pulse is applied, the electrons can move to the opposite side of phosphor again and act as an impact source for light emission.

The main applications of this alternative current electroluminescent device are flat panel displays, but the low efficiency has been a major drawback for its wide use.

### 7.2.2. Introduction

AC electroluminescent (ACEL) devices have several useful characteristics for display, including wide viewing angle, high contrast, and wide operating temperature range (-100C~100C) [101]. However, the low efficiency of ACEL compared to current p-n junction LED devices limits its applications only to the rugged environment display. To increase the efficiency of ACEL devices, we introduced nanowire structures between phosphor layer – dielectric – electrode interfaces. Since high aspect ratio tip can create field enhancement compared to flat structure, it will induce more tunneling of electrons to the phosphor layer and excite dopant atoms more effectively for efficient light emission.

Based on the rational understanding of morphology control of ZnO nanowires, we fabricated the nanostructure embedded ACEL devices and evaluated the performance enhancement.

### 7.2.3. Experiments

The schematic fabrication process of the nanowire embedded ACEL device is shown in Figure 7.8. Pre-cleaned ITO glass (Delta Technologies) was optically patterned to form transparent electrode, then 30 nm ZnO seed layer was coated by RF sputtering (AJA International) at 150W, 20mTorr with 10sccm Ar for 14 minutes. In case of a flexible device, 30 nm thin Au is thermally evaporated to pre-cleaned PET (0.01" thick, McMaster Carr) by shadow mask as a semi-transparent electrode. For nanowire synthesis bath preparation, variable additional cation sulfate ($Al_2(SO_4)_3$ 0.002M,$CdSO_4$ 0.002M, or none) was added to fixed concentration of zinc sulfate ($ZnSO_4$, 0.01M) and ammonium chloride ($NH_4Cl$, 0.3M) in 100 mL deionized solution, then sodium hydroxide (NaOH) was added to adjust pH to 11. The substrate was then introduced to each bath to synthesize nanowires or plates with 1.2 um thick (no addition bath: 4hr, Al 0.002M bath: 6hr, Cd 0.002M bath: 20hr), then removed from the bath, washed with DI water, and dried under nitrogen. On top of this nanostructures, 300 nm ZnS:Mn phosphor layer was deposited by RF sputtering (110W, 3mTorr, 12sccm Ar, 0.8 at.% Mn target, Kurt J. Lesker) at 250 C (60 C for flexible PET device). Barium titanate ($BaTiO_3$) paste (Dupont, LuxPrint 8153) was used to deposit 13 um thick dielectric layer by spin coating at 4000 rpm with 50 sec, followed by heat treatment at 150C for 20 minutes. Top electrode was either deposited with Al by RF sputtering (160W, 3mTorr, 12 sccm Ar, 100 nm) or brush painted using a graphite paste (Alfa Aesar).

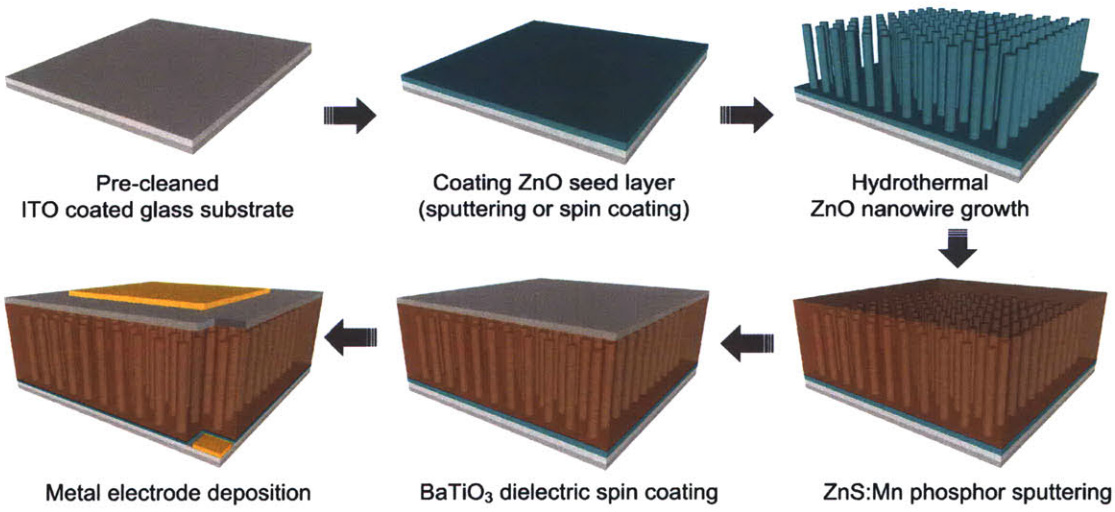


Figure 7.8. Schematic fabrication process of zinc oxide nanowire embedded alternative current electroluminescent device.

ZnO nanostructures, ZnS:Mn phosphor layer, and $BaTiO_3$ dielectric were inspected by SEM (Philips-FEI XL30 ESEM). X-ray diffraction (XRD, Panalytical X'pert Pro) was used to measure the crystalline orientation of ZnO and ZnS:Mn. Photoluminescent spectrum of ZnS:Mn was measured by fluorescence spectrophotometer (Nanolog, Horiba Jovin Yvon) with 160 mW 488 nm $Ar^+$ ion laser(Spectra Physics) as an excitation source. ZnS:Mn optical bandgap was calculated by transmittance measurement of ZnS:Mn on quartz substrate with HP 8452A spectrophotometer. Electroluminescent spectrum of nanowire ACEL device was measured by high resolution fiber optic spectrometer (HR2000, Ocean Optics). Voltage dependent measurement was performed with 5 kHz function generator (HP 33120A) with high voltage amplifier (Trek). Luminance was measured using Konica-Minolta CS-200 luminance color meter. Input power to ACEL device was calculated by measuring voltage drop across the device and a series resistor (200 Ω) and the phase angle between two signals with a Textronix 3054B oscilloscope.

### 7.2.4. Results and Discussion

*7.2.4.1. RF sputtered ZnS:Mn properties*

Many researchers have reported concentration dependent quenching of photoluminescent intensity in ZnS:Mn phosphors [102-104]. For very low concentrations of manganese, which the activator (Mn) is isolated, the luminescent intensity is directly proportional to the concentration of activator ions (Mn). However, activators create interaction each other when the concentration is high enough and perturb the luminescent characteristics. Based on the data from Warren *et al.* [105] and others, ZnS:Mn showed a decrease in luminescence intensity when Mn concentration was above 1 at.% (Figure 7.9). For deposition, 0.8 at. % Mn in ZnS target was custom made to minimize luminous intensity decrease by activator interactions.

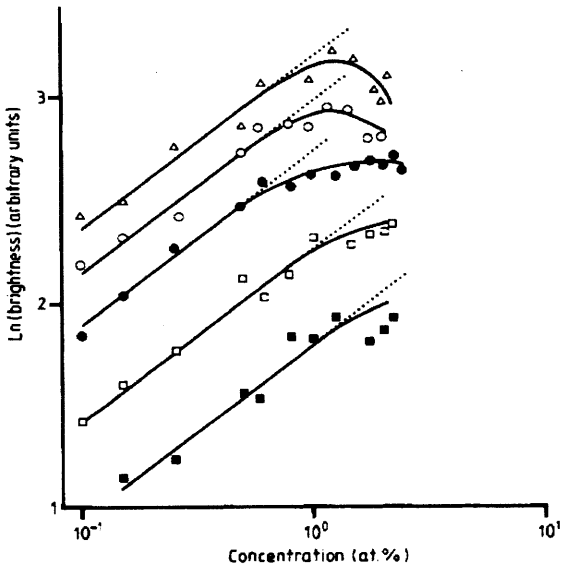


Figure 7.9. The intensity of photoluminescence as a function of Mn concentration in ZnS with different annealing temperatures (■ 300C, □ 350C, ● 400C, ○ 450C, Δ 500C) for 1hr. Image taken from Warren *et al* [105].

To achieve high luminescence device, activating Mn atoms in ZnS matrix is necessary. Higher temperature during deposition gives larger grain size and host atom

activation more effectively [106] as shown in Figure 7.10. However, the substrates using for the device testing were soda lime float glass ($T_g$ ~ 500C ) and PET ($T_g$ 70 C ~ 80 C, $T_m$ ~260 C). To achieve reliable device fabrication with specified materials, deposition was carried out at 250 C for glass device and 60 C for PET device.

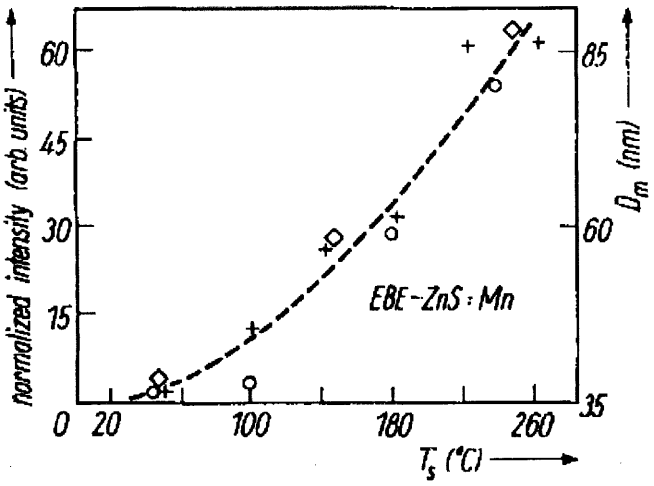


Figure 7.10. Normalized photoluminescence(+) and cathodoluminescence(o) efficiencies of ZnS:Mn layers and mean grain diameter (◊) at thickness t = 500 nm vs. substrate temperature Ts. Image taken from Theis [106].

After depositing ZnS:Mn layer on top of amorphous glass slide, XRD was performed to evaluate crystallinity. Sample deposited at 250 C showed (111) an (311) peaks of ZnS, indicating polycrystalline phase (Figure 7.11). No Mn peak existed in a detection limit of XRD, indicating that Mn is incorporated to ZnS as a substitutional to Zn lattice. Sample deposited at 60 C also showed similar characteristics (data not shown).

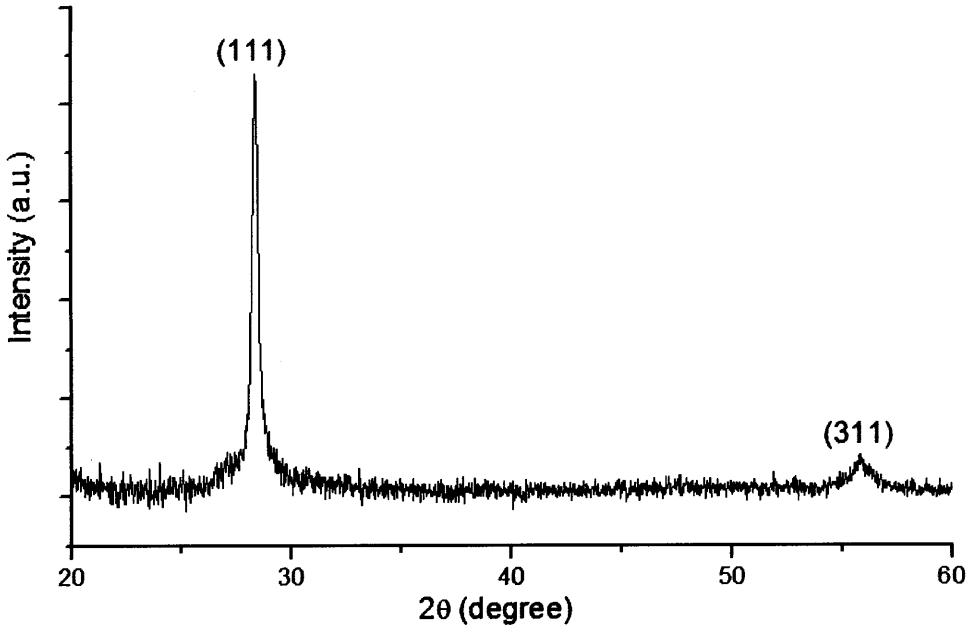


Figure 7.11. XRD pattern of 300 nm thick ZnS:Mn on top of glass substrate deposited at 250 C. Distinctive (111) and (311) ZnS peak with no Mn peak indicates phase homogeneity within a detection limit.

Optical absorption spectra of the ZnS:Mn films were measured as a function of photon energy (hv) in a wavelength range of 200 ~ 800 nm. Optical bandgap can be measured by Tauc relationship [107] as follows,

$$\alpha h\nu = A\,(h\nu - E_g)^n \qquad (1)$$

where $\alpha$ is the absorption coefficient, A is a constant, h is Plank's constant, $\nu$ is the photon frequency, $E_g$ is the optical bandgap, and n is ½ for direct bandgap semiconductors [108]. An extrapolation of $(\alpha h\nu)^2$ on the y axis versus $h\nu$ on the x axis gives the value of optical bandgap at $(\alpha h\nu)^2 = 0$. Figure 7.12 Shows Tauc plot data of ZnS:Mn deposited on glass substrate, and optical bandgap energy is extrapolated to be 3.89 eV, which is similar value reported elsewhere [109-110].

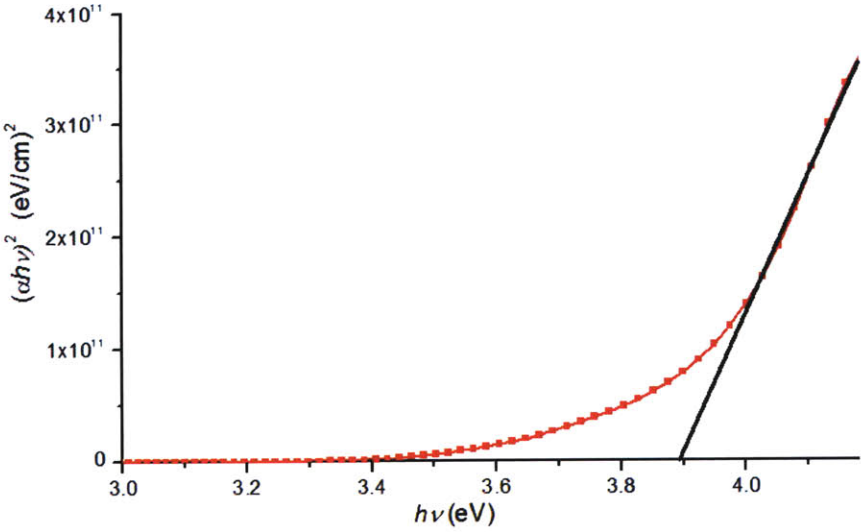


Figure 7.12. Tauc plot (n=1/2) for of 300nm thick ZnS:Mn on glass substrate. The linear extrapolation of the Tauc region (bold) intersects with the energy axis of 3.89 eV.

Photoluminescent spectrum was measured with ZnS:Mn deposited on quartz substrate. Initially, Xe lamp installed to the Nanolog spectrophotometer was tested as an excitation source, but low excitation intensity gave no detectable range of photoluminescence. Optical fiber guided 488 nm $Ar^+$ ion laser with 160mW enabled high intensity excitation, giving successful PL spectra as shown in Figure 7.13. This broad band spectrum has a peak at 592 nm fitted with Gaussian distribution by $h\nu$ vs. intensity, then plotted with $\lambda$ vs. intensity again. This yellow/orange PL comes from the energy release of manganese electrons from the photoexcited states to the ground states.

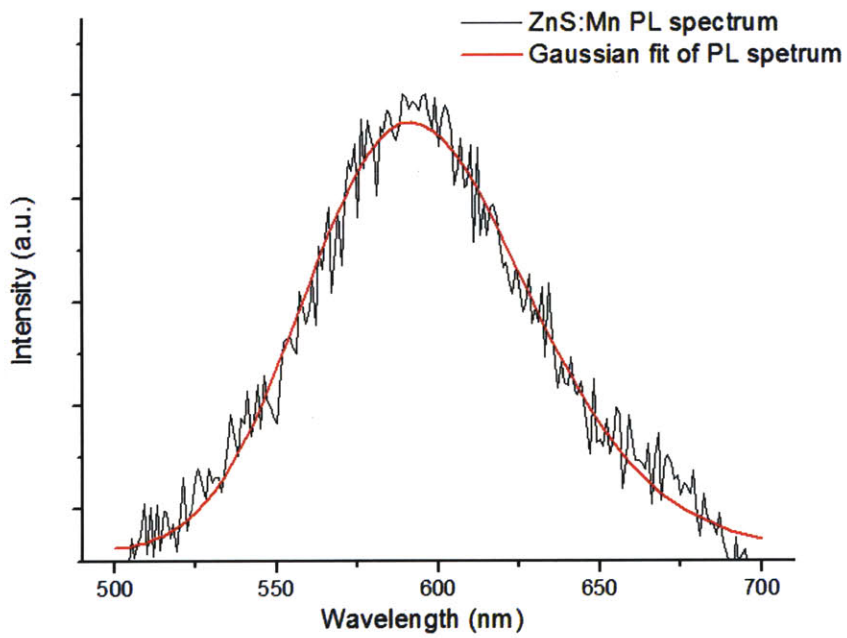


Figure 7.13. Photoluminescence spectrum of ZnS:Mn on quartz substrate excited with 488 nm $Ar^+$ ion laser.

*7.2.4.2. Dielectric layer deposition*

There are several requirements for dielectrics to be used for an ACEL device. It should provide carrier confinement, charge storage and barrier protection, as well as mechanical/thermal stability during operation. General figure of merit is the charge density of the electric displacement at breakdown, which is a product of dielectric constant (ε) and breakdown electric field ($E_{bd}$) [111].

$SiO_2$ has high dielectric constant (ε =15) with high breakdown field (1~10 MV/cm), but known to have a stability issue. We tried PECVD $SiO_2$ deposition (MTL, MIT) and several spin on glass (IC1-200/Futurrex, and Fox14/Dow Corning) deposition, but no reliable result was achieved with $SiO_2$.

BaTiO3 also has high dielectric constant (ε =15~20 in amorphous, ε > 100 in polycrystalline) and reasonable breakdown field (~0.1MV/cm) [112], so it was chosen for

this ACEL device study. Dupont 8153 dielectric paste was used for $BaTiO_3$ dielectric coating. Si substrates were coated with various spin speed for thickness measurement (Figure 7.14).

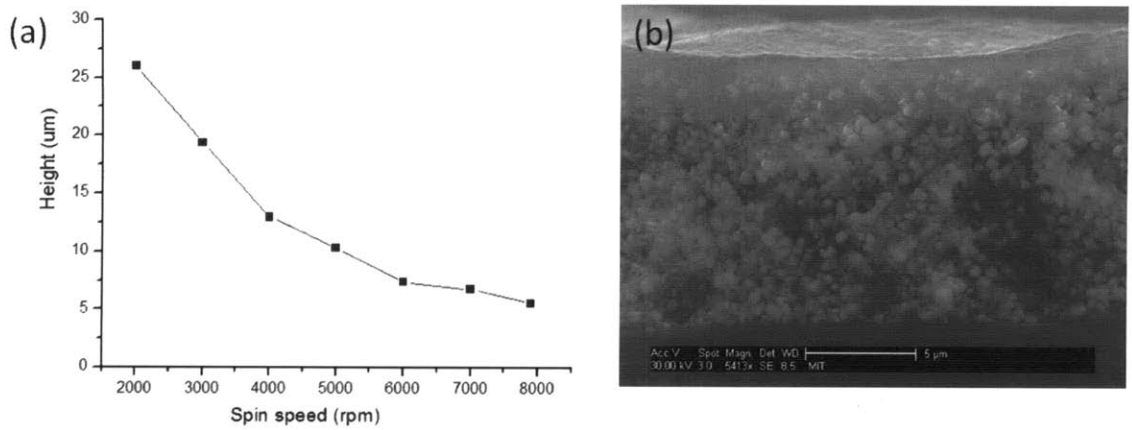


Figure 7.14. (a) $BaTiO_3$ thickness versus different spin coating speed using Dupont 8153 dielectric paste. (b) Cross sectional SEM image of $BaTiO_3$ on Si substrate coated at 4000 rpm.

*7.2.4.3. Nanowire ACEL device*

Cross sectional image of nanowire ACEL device is shown in Figure 7.13. On top of 1.2 um thick ZnO nanowires, 300 nm thick ZnS:Mn was conformally coated between nanowires, followed by 13 um thick $BaTiO_3$ dielectric deposition.

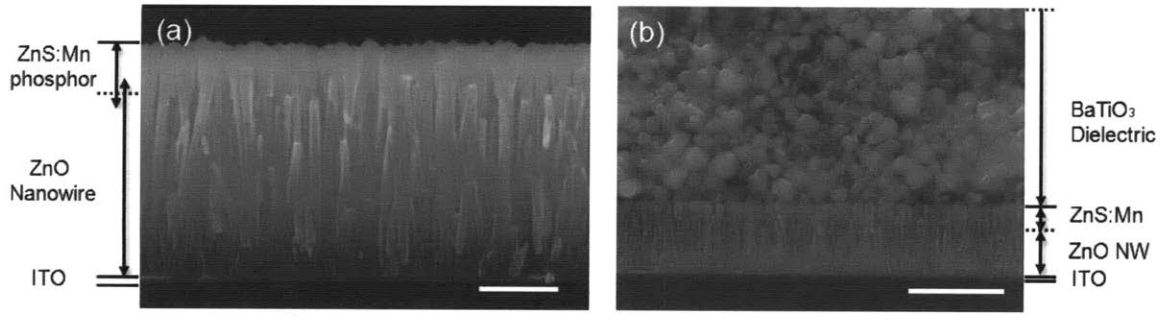


Figure 7.15. Cross section SEM of 300 nm thick ZnS:Mn sputtered on ZnO nanowires (a) and $BaTiO_3$ dielectric spin coated over ZnS:Mn/ZnO nanowires (b). Scale bar = 500 nm (a), 2 um (b).

Electroluminescent spectra of ZnO nanowire embedded ACEL device is shown in Figure 7.16. Maximum peak was 596 nm close to Gaussian fitted PL maximum of 592 nm, indicating the EL light also comes from energy transfer from the excited states to the ground states of manganese electrons. However, the electron excitation mechanism is different from photoexcitation. In ACEL case, high electric field at phosphor layer creates accelerated electron in the layer or tunneling of electrons from the dielectric layer, then accelerates and impact the ground electrons of Mn. There was no difference in EL spectra with and without nanowires (image not shown), indicating that ZnO nanowires serve only as a field enhancing layer, not an active light emitting layer.

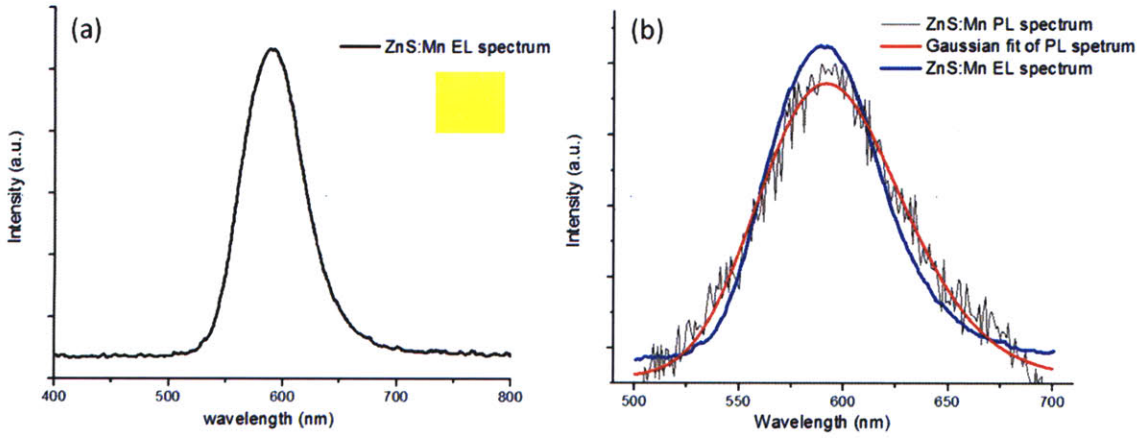


Figure 7.16. (a) ZnS:Mn Electroluminescence spectra measured with nanowire embedded ACEL device running at 300 V at 5 kHz. Inset: color captured image from the device. (b) ZnS:Mn PL and EL spectra compassion.

ZnO nanowire embedded flexible ACEL device is demonstrated in Figure 7.17. In this device, light comes through the thin Au instead of ITO. However, it still shows same distinctive EL color from phosphor layer. Since nanowires can withhold more strain than thin film by having inter wire spaces without cracking, this nanowire embedded ACEL device can be useful for flexible lighting or display devices with high efficiency, low voltage operation.

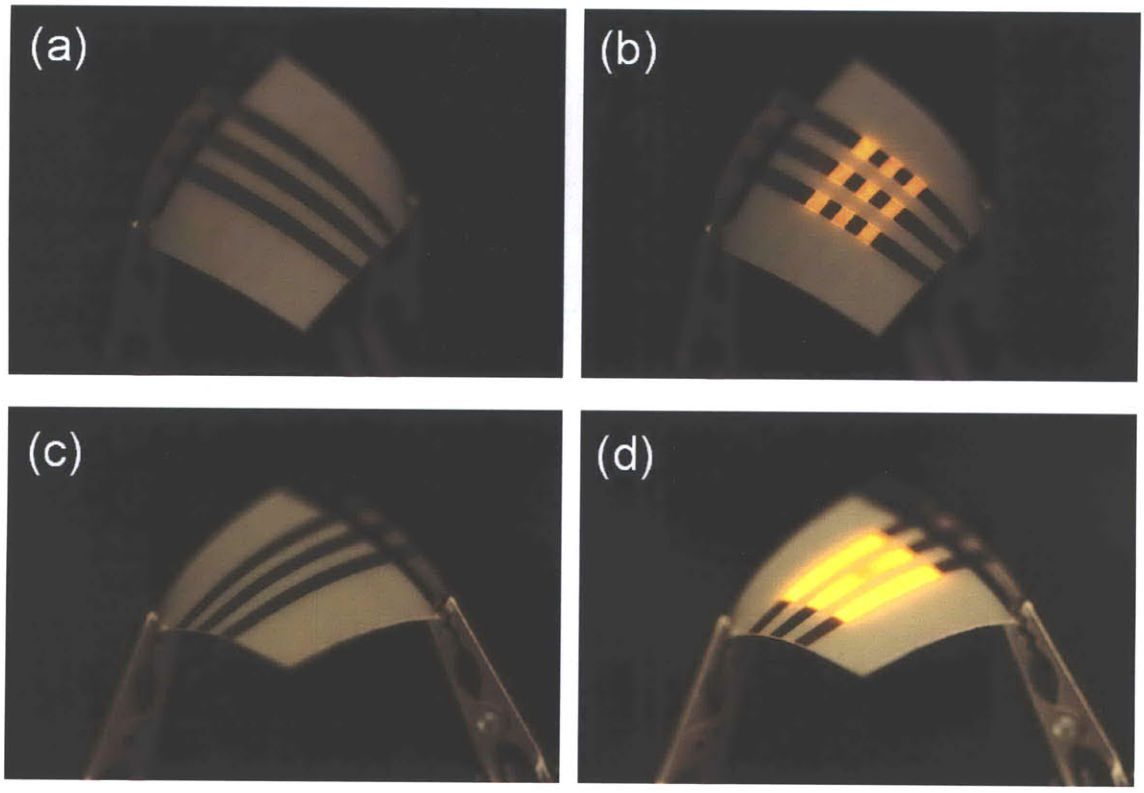


Figure 7.17. ZnO nanowire embedded AC electroluminescent device on flexible PET substrate. Cross bar array device (a) off (b) on, and stripe device (c) off (d) on.

Voltage dependent characteristics of each device are shown in Figure7.18. Within hydrothermally grown ZnO embedded ACEL devices (Al 0.002M, no addition, Cd 0.002M), trend was similar to the field emission device described in the previous section. Device with high aspect ratio nanowire (Al 0.002M) had a low threshold voltage to reach same luminance compared to the device with lower aspect ratio nanowire (no additional cation), followed by lowest aspect ratio plate (Cd 0.002M) device. Field enhancement near the tip seems to be a key factor in enhanced luminance with higher aspect ratio structures. This locally enhanced electric field would increase tunneling electrons, accelerates electrons faster, and excites dopant atoms more effectively, thereby producing more light at the same applied voltage. Since the spacing between phosphor layer and

bottom seed layer was fixed at 1.2 um, electric field drop across ZnO nanostructures would not be related to the voltage shift. Also, nanowire structure might guide the light through by waveguide effect, and external quantum efficiency might have been increased with embedded nanostructures. Interestingly, all devices with hydrothermally grown nanostructures had a higher light emission at same voltage compared to the control device (without nanostructures). In case of a control device, distance between the top and the bottom of the device would be 13.3 um. Smaller than that of nanostructure embedded devices (14.5 um, adding 1.2 um layer). Therefore, electric field at the same voltage should be higher with control device if field enhancement does not exist. The low luminance with control device indicates that introduced nanowires or nanoplates with sharp tips are important factors to enhance light emission in ACEL devices.

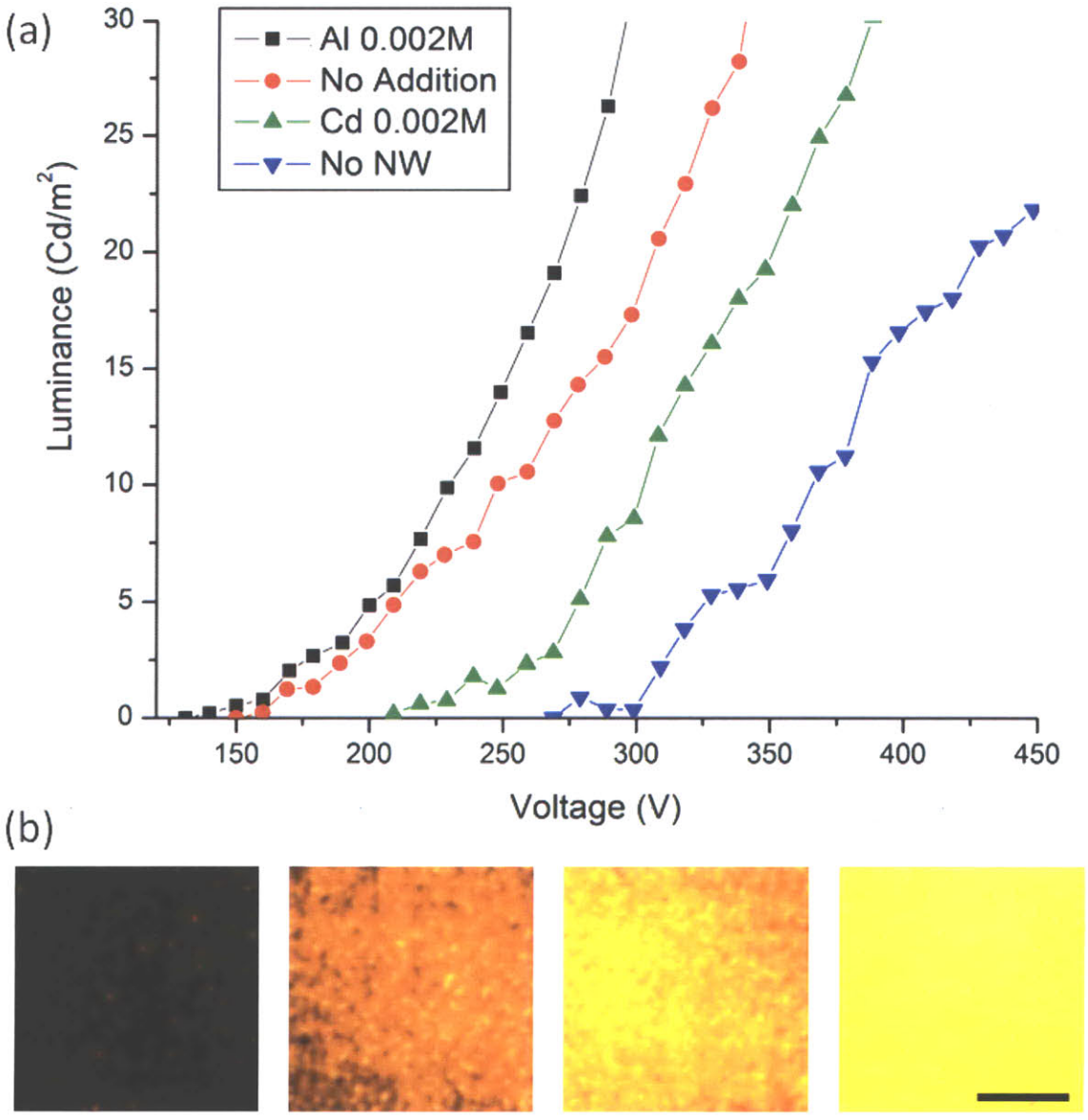


Figure 7.18. (a) Voltage dependent luminance data with different nanowires embedded under ZnS:Mn layers. (Al 0.002M: additional $Al_2(SO_4)_3$ 0.002M added during growth, No addition: ZnO nanowires grown only with $ZnSO_4$, $NH_4Cl$ in DI water solution with NaOH pH 11, Cd 0.002M: additional $CdSO_4$ 0.002M added during growth, No NW: only 30 nm ZnO seed layer exists without nanowire growth) (b) Electroluminescent light emission from each device operating at 260 V. From left to right: No NW, Cd 0.002M, No addition, Al 0.002M. Scale bar = 500 um.

Schematic diagram of device power measurement setup is shown in Figure 7.19. Since device operates in AC condition, phase between current and voltage of the device was measured for power calculation. Assuming perfect sinusoidal wave of I and V, AC power would be calculated by the following equation,

$$P = I \cdot V \cdot cos\varphi = \left(\frac{V_2 - V_1}{R}\right) \cdot (V_3 - V_2) \cdot cos\varphi \quad (1)$$

where P is power, I is current (root mean square, RMS), V is voltage (root mean square, RMS), and $\varphi$ is phase shift between current and voltage. A series resistor was used for current measurement.

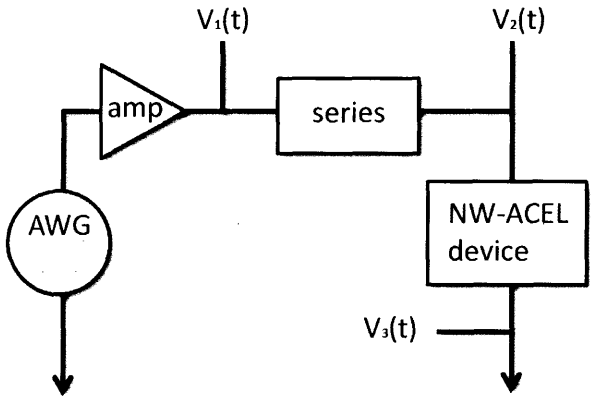


Figure 7.19. Schematic diagram of power measurement setup for NW-ACEL device.

Figure 7.20 shows current and voltage signals of nanowire embedded ACEL device under 300 $V_{rms}$ operation. There is an apparent peak shift between I and V, indicating capacitive term exists in ACEL device, mainly by a dielectric layer. At a high voltage, the current did not follow perfect sinusoidal shape as voltage, and the reason is not clear. It may come from the trapping and release of electrons at dielectric layer, phosphor, and nanowires different from a conventional AC circuit. This current characteristic may lead to explain other light emission mechanisms of ACEL device also.

The power should be calculated by integration of $I(t) \cdot V(t)$ for one cycle, and divided by the time of the cycle. However, the real power calculated from the integration and the power calculated from the equation (1) stated above showed ~ 95% match, so equation (1) was used for luminous efficiency calculation.

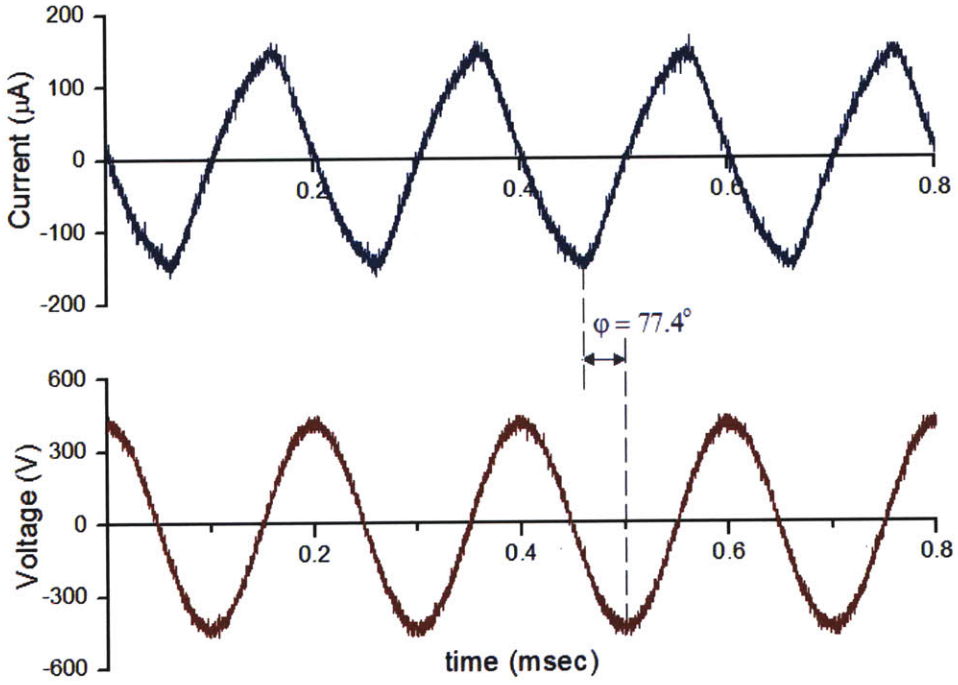


Figure 7.20. Current / Voltage signal of nanowire embedded ACEL device operating at 300 $V_{rms}$ with 5 kHz. Phase shift is measured from the peak to peak value between current and voltage.

Voltage dependent luminance efficiency is shown in Figure 7.21. The trend was similar to the voltage dependent luminance, but ZnO nanowires with Al 0.002M device had a huge efficiency increase compared to other no addition /Cd 0.002M device. This might be from the tip geometry of nanowires and spacing between nanowires. Close packed nanowires do not effectively contribute to field enhancement, known as screening effect [113-116]. Spacing of nanowires can be controlled using block copolymer self assembly or other lithography process discussed in the previous section. Even though the

system is not optimized, at least 10 fold increase in luminous efficiency at 300 ~ 400 V was observed between Al 0.002M device and the control device. Further optimization of nanowire shape, spacing between nanowires, length of nanowires, thickness of phosphor layer and dielectric layer would give higher efficiency improvement for practical applications.

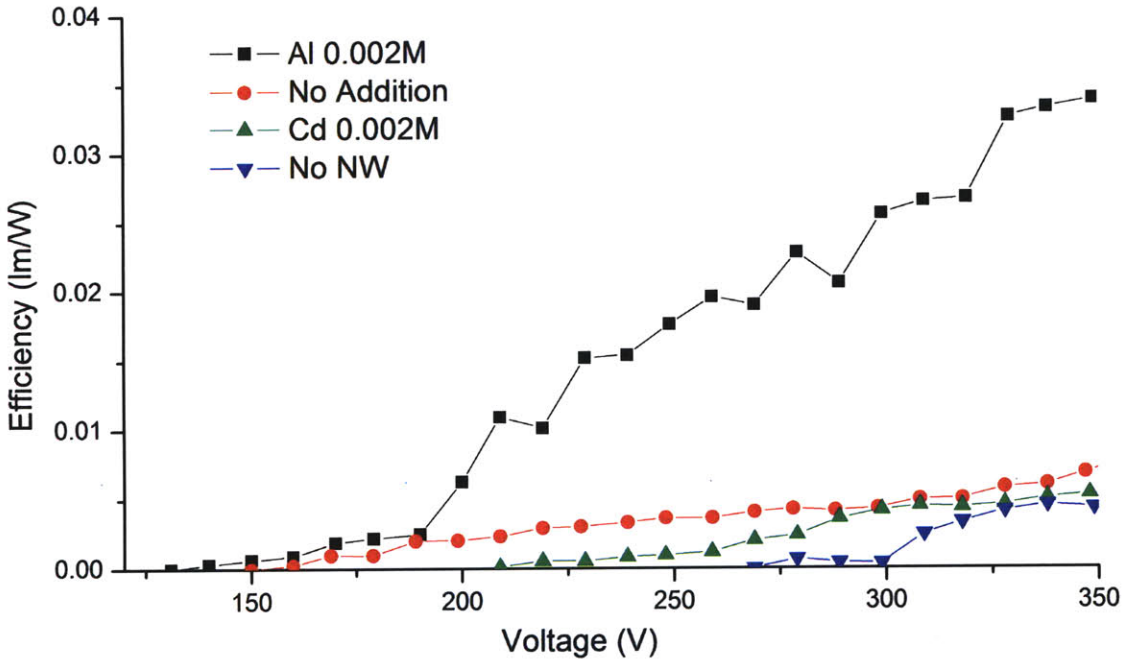


Figure 7.21. Voltage dependent luminous efficiencies for different nanostructure embedded ACEL devices.

We believe that the device has a huge potential to increase the performance by several optimization parameters. Compared to our control device, researchers have reported ACTFEL luminance up to 7,700 Cd/m$^2$ and 9.5 lmW$^{-1}$ using $((Y_2O_3)_{0.6} - (GeO_2)_{0.4})$:Mn phosphor with $BaTiO_3$ dielectric with post annealing at 1020 C [117-118] . Others reported a luminance up to 1,800 Cd/m$^2$ with luminous efficiency and 1.2 lmW$^{-1}$ using $Y_2O_3$ as a dielectric layer on ZnS:Mn with multiple annealing steps at high temperature ~ 500 C [119]. Using metal organic CVD system for ZnS:Mn deposition

with thick $BaTiO_3$ sheet, turn on voltage (at 1 $Cd/m^2$) as low as 20 V was also demonstrated [120]. If we can make our control device to perform in a similar luminance and efficiency range as others reported by optimizing phosphor and dielectric material, deposition processing condition, and further annealing, the improved nanowire embedded ACEL device may be applicable to current lighting or display technology, such as LCD or OLED display having a brightness range of 350 ~ 1000 $Cd/m^2$.

| sample | Turn on voltage (V at 1cd/m2) | luminance ($cd/m^2$) | Max Luminous efficiency (lm/W) | Notes |
|---|---|---|---|---|
| Al 0.002 M | ~ 160 | 131 | 0.065 | High aspect ratio nanowires embedded |
| No addition | ~170 | 54.7 | 0.009 | Nanowires embedded |
| Cd 0.002M | ~230 | 30.2 | 0.0064 | Nanoplates embedded |
| Control (no NW) | ~ 300 | 22.7 | 0.006 | N/A |
| $\{(Y_2O_3)_{1-x}$-$(GeO_2)_x\}$:Mn / $BaTiO_3$[a] | < 100 | 7,700, 724 | 1.0, 9.5 | New phosphor, anneal at 1020C |
| ZnS:Mn / $Y_2O_3$[b] | ~ 200 | 1,800 | 1.2 | Anneal at E-field , oxygen glow discharge |
| ZnS:Mn / $BaTiO_3$ sheet[c] | ~ 20 | 6,300 | 11 | ZnS:Mn by MOCVD |
| Cold Cathode Fluorescent light[d] (LCD backlight) | N/A (120~1500 at run) | 32,000 | 60 ~ 70 | In production |
| CNT FED[e] | N/A (1kV at run) | 10,000 | 31 | Printed CNT for BLU |
| LED[f] | 0 ~ 2 | 50 ~ 110 | 208 | New record for white LED |
| OLED[g] | 2.5 ~ 3 | 1,000 ~ 10,000 | 90 | Pattern surface for high extraction efficiency |

Table 7.1. Comparison of device performance with nanowire embedded ACEL devices and other technologies. [a]Reference [117]. [b]Reference [119]. [c]Reference [120]. [d]Reference [121]. [e]Reference[122]. [f]Reference [123]. [g]Reference [124].

### 7.2.5. Conclusion

In conclusion, we demonstrated a high efficiency, low voltage ACEL device by introducing optimized nanowire structures between phosphor and electrode layer. Depending on the morphology and aspect ratio of nanostructures, luminance and luminance efficiency at the fixed voltage changed dramatically. We also demonstrated flexible nanowire embedded ACEL devices. Controllable nanostructure synthesis in a

hydrothermal process gave the efficiency increase, addition to the compatibility of large scale flexible devices. This process may lead to the development of new lighting devices for rugged display, consumer electronics, and others.

## 7.3. Metal/Insulator/Semiconductor Nanowire Light Emitting Diode device

### 7.3.1 Background

Band diagram of metal / insulator / semiconductor (MIS) diode under forward bias is shown in Figure 7.5. If the insulator layer is too thin (Figure 7.5(b)), electrons from the semiconductor (in this case, n-type ZnO) can tunnel through, so radiative e-h recombination would not exist. If insulator layer is thick enough, electrons from ZnO at forward bias would accumulate at the insulator/semiconductor interface. Hole injection mechanism for MIS diode is still not clear, but there are several possible pathways. Electron – hole pairs are generated at the insulator layer by impact ionization under high electric field. Even though the lifetime would be considerably small, holes from this layer can be swept into the valence band of ZnO. Holes in ZnO also can be generated if electrons at the valence band of ZnO layer are drawn into the electron trap sites at the insulator layer under sufficient forward bias. These holes and accumulated electrons produce lights by radiative recombination process.

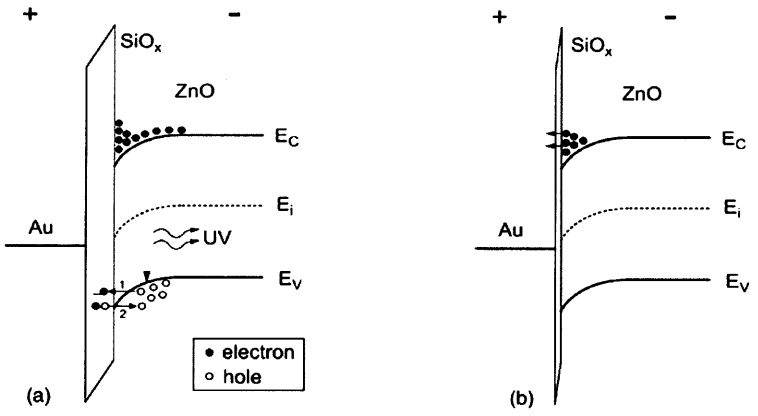


Figure 7.22. Schematic energy band diagrams of two ZnO based MIS structure with different SiOx thickness layer under the forward bias. (a) with ~100 nm thick SiOx layer, arrows 1 and 2 refer to two possible pathways for injection of holes into the valence band of ZnO for light emission. (b) with ~ 10 nm layer. Image taken from Chen *et al.*[125]

### 7.3.2. Introduction

Zinc oxide is an n-type semiconductor with a direct bandgap of 3.2 ~ 3.4 eV quite close to bandgap of GaN (~3.4 eV). ZnO can be used for blue to ultraviolet light emitting diode (LED) as a current GaN substitute. However, p type doping of ZnO has been always a problem, and still not solved yet even though many researchers are currently working on it [126-131]. N-type character of ZnO is known to come from oxygen vacancy, and property changes with different annealing condition. Since p-type ZnO is not readily available, ZnO based p-n junction structured LEDs are mostly demonstrated with n-type ZnO combined with different materials for p-type layer such as p-type GaN [132-136].

In this chapter, we examine other possibility of LED using metal / insulator / semiconductor nanowire (MIS) structure. Instead of using p-type hole injection layer for p-n junction diode, insulator was used for electron accumulation at insulator/ZnO nanowire interface. Using spin on glass as an insulator layer that penetrates gap between nanowires and form smooth surface on top, ZnO nanowire based MIS LED was evaluated under forward bias. Furthermore, we examine the MIS LED using microfluidic nanowire synthesis toward in-situ device fabrication.

### 7.3.3. Experiments

The schematic of the nanowire synthesis is shown in Figure 7.20. Transparent electrode is patterned by optical lithography. Pre cleaned ITO on glass substrate (Delta Technologies) was spin coated with AZ 4620 photoresist at 1500 rpm for 40sec, and prebaked at 90 C for 1hr. The photoresist was exposed at UV (INTELLI-RAY 400, Uvitron) with 50mW/cm$^2$ for 20sec, and developed by AZ 440K developer with active

agitation. Exposed ITO was etched by ferric chloride ($FeCl_3$, 25~30%) mixed with hydrochloric acid (HCl, 1~5%) in water (TE-100, Transcene) for 2 hrs, then cleaned with DI water, dried under nitrogen. 30 nm thick ZnO seed layer was deposited on top of ITO patterned substrate by RF sputtering at 150W with 20mTorr, 12 sccm Ar condition. Nanowires were grown under zinc sulfate ($ZnSO_4$ 0.01M), ammonium chloride ($NH_4Cl$ 0.3M) in deionized water with pH 11 adjusted by sodium hydroxide (NaOH) for 6 hrs. On top of ZnO nanowire substrate, small section of the corner was covered with masking tape (3M) to protect ITO layer, followed by spin coating spin on glass (SOG) (IC1-200, Futurrex) at 3000rpm for 40 seconds for multiple times. After removing the masking tape, the substrate was annealed at 200 C for 1hr, then 300C for 1hr on a hotplate consecutively. Top 40 nm Au electrode was deposited by thermal evaporation with a shadow mask.

In case of microfluidic nanowire MIS LED, 100 um (width) x 80 um (height) x 15 mm (length) microfluidic channel was made using SU-8 mold as described in chapter 5. To bond the PDMS and a ZnO coated ITO patterned glass, precut PDMS layer was put on top of uncured PDMS pre-polymer (GE, RTV 615) at a component A to B ratio of 10 : 1 spin coated on top of Si wafer at 6000 rpm for 4 minutes. The PDMS was then transferred to ZnO coated substrate, followed by curing in a convection oven at 80 C for 3 hours. Nanowire growth in microfluidic channel was performed with same solution as bulk condition described above at 50 C for 30 minutes at a flow rate of 0.6 mL/h. SOG was flown through the channel at flow rate of 1 mL/h for 10 seconds at 200 C with a same flow direction as growth. Top electrode was formed by flowing molten metal (In52 / Sn48, AIM Specialty Inc.) with a low vacuum from the opposite end of the channel at

200 C [137].

Nanowires and spin on glass dielectric layers were examined by scanning electron microscopy (Philips-FEI XL30 ESEM). Photoluminescence of ZnO nanowires was measured by spectrophotometer (F7000, Hitachi) with excitation of 325nm using monochromatized Xe source at room temperature. Spectrophotometer (HR2000, Ocean optics) was used for the spectral measurement of the light emission. Electrical I-V characterization was performed with HP 4156A semiconductor analyzer. Macroscale device images with light on/off were captured by Canon Rebel XTi DSLR camera with EF 24-70mm f/2.8L USM macro lens. To calculate the external quantum efficiency, EL from the glass side of the device was measured using a calibrated low power Si photodiode (818-UV, Newport) with picoammeter (Keithley 485).

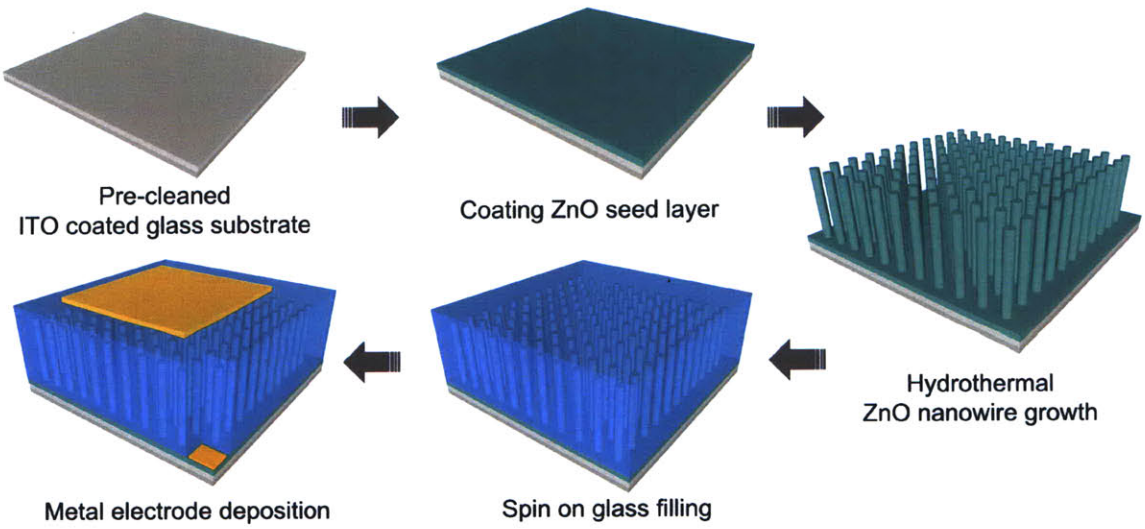


Figure 7.23. Schematic of metal / insulator /semiconductor nanowire LED device fabrication process.

### 7.3.4. Results and Discussion

Spin on glass (IC1-200, Futurrex) is a polysiloxane based chemical generally used for the planarization process of integrated circuits. After nanowires are synthesized, the spin on glass (SOG) solution was spin coated to form as a dielectric to block electrons moving from ZnO to metal electrode before radiative electron hole pair recombination happens. Figure 7.24 shows the cross sectional image of SOG/ZnO nanowire structure after spin coating for three times followed by heat treatment. All gaps between nanowires were filled with SOG and top had a thin dielectric layer (~ 120 nm) formed serving as a weak insulator. A sample with SOG coated for four times had a ~180 nm thick layer from the tip of the nanowires with flat surface. A sample with SOG coated for two times had a 30 nm ~ 100 nm thick dielectric layer (large variation within a sample) and the surface was not as smooth as SOG with three or four times coating.

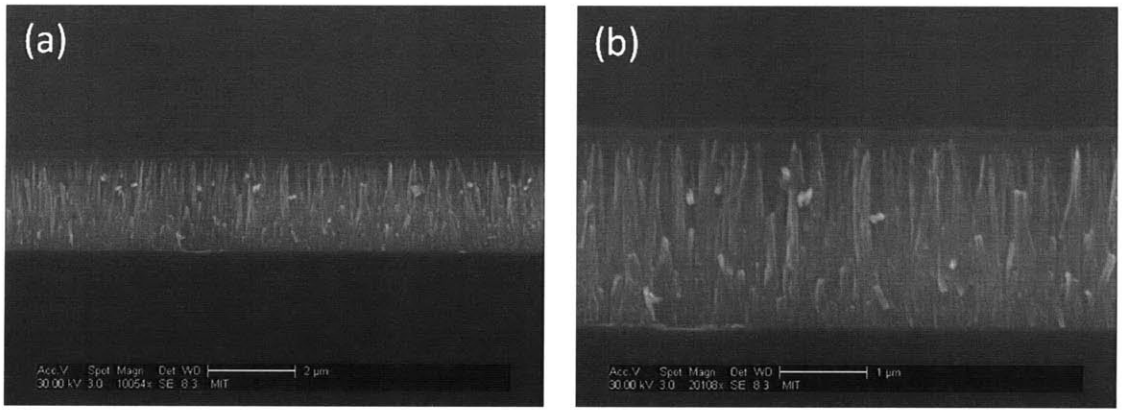


Figure 7.24. Cross sectional SEM image of dielectric coated on top of ZnO nanowires grown on ITO substrate. Top dielectric is formed by spin coating spin on glass at 3000 rpm, 40 sec for 3 times followed by heat treatment. Spin on glass penetrated ZnO trenches and formed smooth flat top surface.

The thickness dependent I-V characteristic of typical diode is shown in Figure 7.25. All devices with different insulator thickness show a good rectifying behavior of the MIS diode, with different threshold voltages and a reverse current of about $10^{-5}$ A (or current density 3.14 x $10^{-4}$ A/cm$^2$). Based on I-V curve, 2 layer SOG coated device seems to have a tunneling of electrons more frequently than other devices because it has a short distance to tunnel by thickness variation. 3 layer SOG coated device showed a threshold voltage near 3 V, where as 4 layer SOG coated device showed a threshold near 5 V, mainly by the thickness difference of insulators.

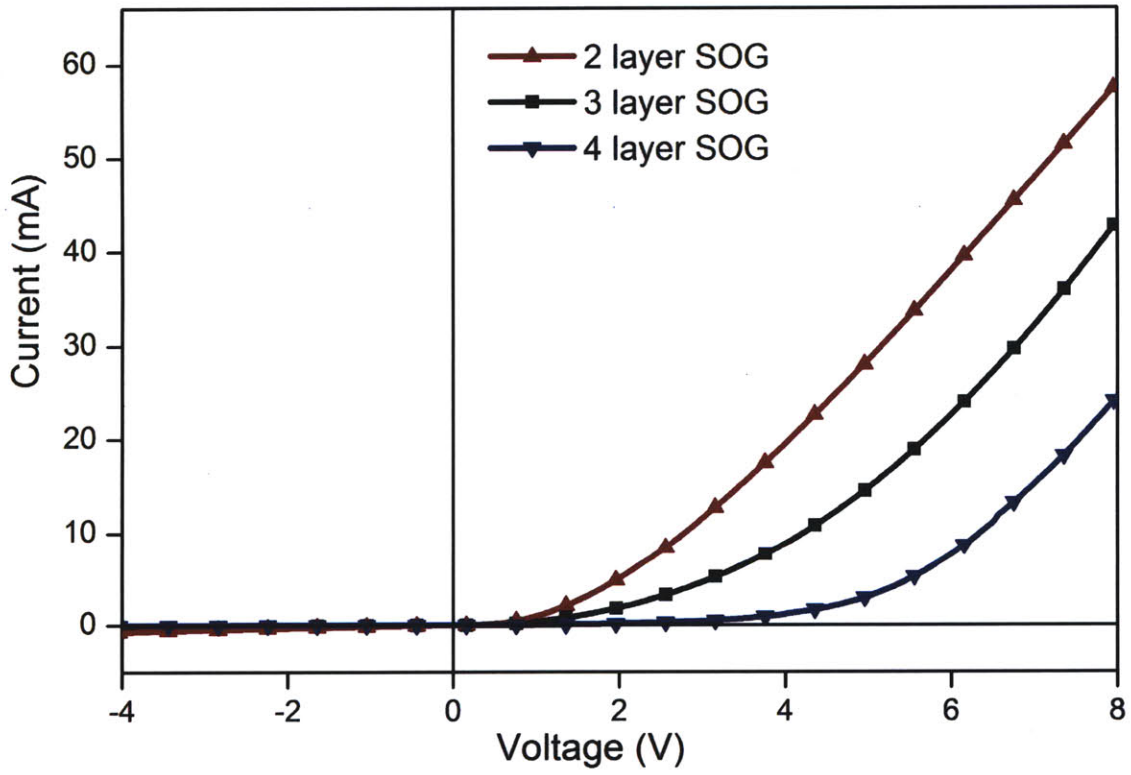


Figure 7.25. Current-Voltage characteristic Au/SOG/ZnO nanowire/ITO with different SOG layer repetitive coating. Nonlinear IV data shows a rectifying behavior, and a sample with a thicker insulator shows a higher threshold voltage.

Under forward bias (Au metal positive), broadband emission was observed at room temperature. Figure 7.26 shows an image of the light emitted from a single device with cross bar array. The diodes emitted orange to red spectrum of light, possibly from the dominance of deep level defects [29, 138-139].

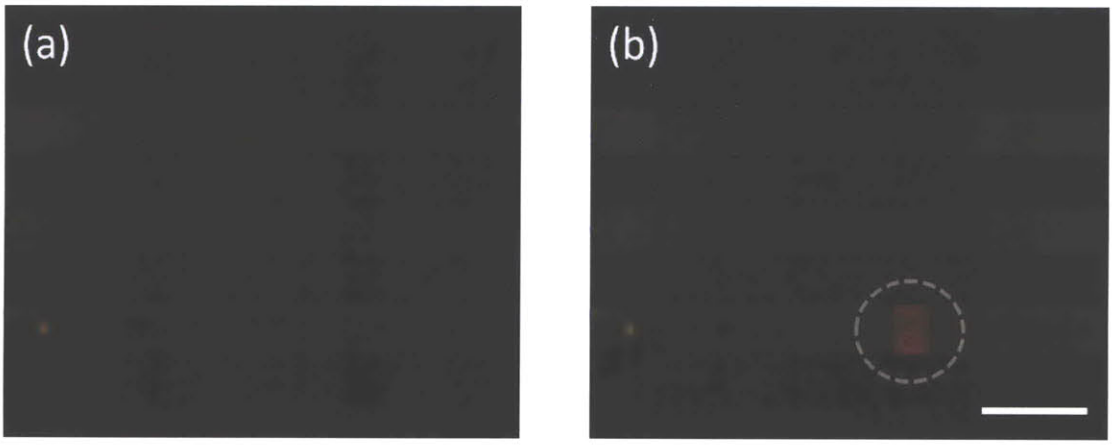


Figure 7.26. Camera captured image of metal/insulator/ZnO nanowire semiconductor light emitting diode device under zero bias (a) and bias at 8V (b). Active square region (1.59 mm x 2mm) shows light emission under bias. Scale bar = 5 mm.

Figure 7.27 shows room temperature PL from ZnO nanowires on top of ITO substrate. Band edge emission at UV was observable, but defect related emission intensity was more pronounced. Even though we were able to capture the light emission from the camera with a long exposure time, EL spectrum was not measured within a detection limit of several analytical spectrophotometer tools (HR2000 Ocean optics, or AQ 6315A Ando optical spectrum analyzer). Low energy conversion efficiency of MIS compared to conventional p-n junction would be the reason for low power light emission. Using a PL as a reference spectrum for EL, calculated external quantum efficiency of the device was in the range of $10^{-6}$ ~$10^{-7}$ %, lower than Si MIS LED devices reported [140].

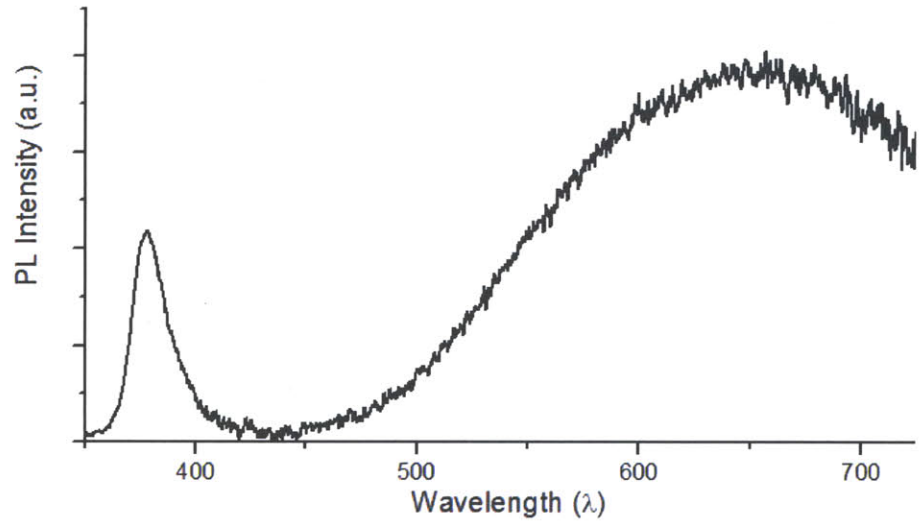

Figure 7.27. Photoluminescent spectra of 3 layer SOG coated ZnO nanowires.

Using the similar process, we also developed in-situ device fabrication of MIS LED with microfluidic ZnO nanowire synthesis. All active device components (active ZnO nanowire, SOG, and electrodes) were fabricated within a microfluidic channel. Figure 7.28 shows the SEM image of full device. SOG thickness was ~ 240 nm, thicker than 4 layer spin coated on the bulk nanowire sample described before. Molten metal conformally coated on top of SOG layer up to the PDMS structure (Figure 7.28c), and formed as a top electrode.

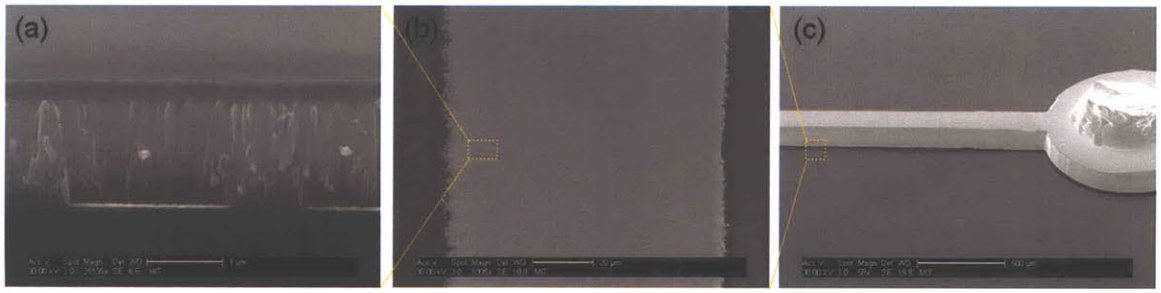

Figure 7.28. (a) Cross sectional SEM of SOG/ZnO in a microfluidic channel. (b) 45 degree tilted SEM image of SOG/ZnO synthesized in a fluidic channel. (c) 45 degree tilted SEM image of metal / SOG/ ZnO. Top PDMS layer was detached for the imaging.

The I-V characteristic of in-situ fabricated MIS LED in a fluidic device is shown in Figure 7.29. It showed a good rectifying behavior of the MIS diode with a threshold voltage around 4 V, and a reverse current of about $10^{-8}$ A (or current density 5 x $10^{-6}$ A/cm$^2$).

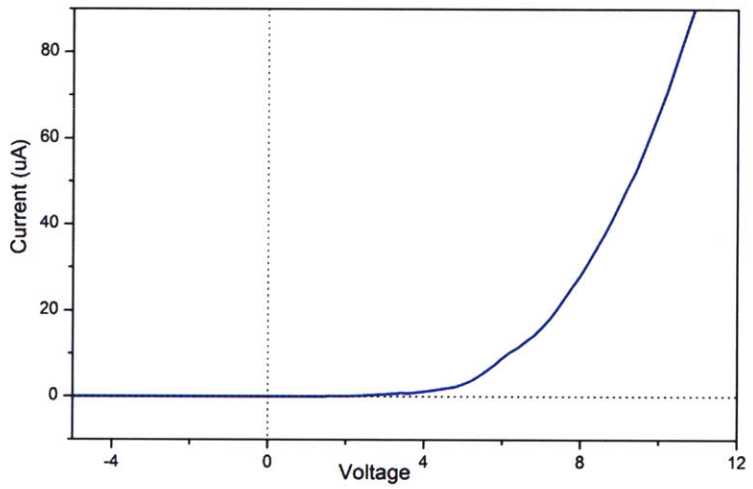


Figure 7.29. Current-Voltage characteristic molten metal/SOG/ZnO nanowire/ITO within a microfluidic channel. Nonlinear IV data shows a rectifying behavior.

Device was tested under forward bias of 10 V, and it showed broadband white light emission at room temperature. Figure 7.30 shows an image of the light emitted from a single device with cross bar array. No light was observed under reverse bias. A control device without ZnO film and nanowire also did not give any light, indicating that ZnO is the active light emission materials. Light shown at here was close to the white light, and it is possibly coming from similar oxygen related defects people have reported so far [138]. Unfortunately, we were not able to measure the EL spectrum with measurable tools we tried, indicating low light conversion efficiency. Using a PL as a reference spectrum for EL, calculated external quantum efficiency of the device was in the range of 2 x $10^{-6}$ %, similar to MIS LED fabricated with spin coating device without microfluidic system.

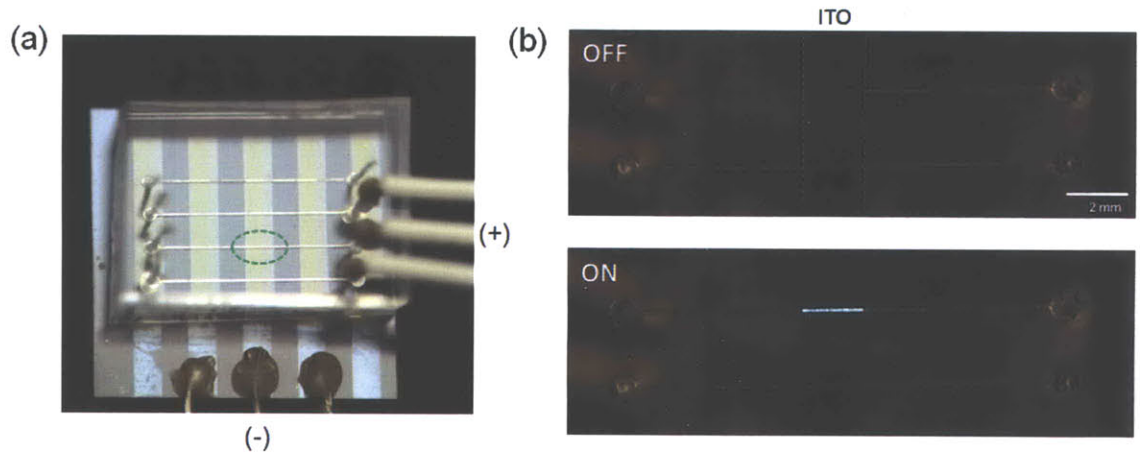


Figure 7.30.(a) Camera captured image of in-situ fabricated microfluidic MIS LED device (b) Device under zero bias and bias at 10 V Active rectangular region (200 um x 2mm) shows light emission under bias.

Even though light intensity is not optimized, this microfluidic in-situ device fabrication has several advantages. Since each channel can be filled with different chemical solutions, multi color component LED can be made within one chip by growing different bandgap materials at each channel. Also, the fluidic process consumes minimal chemical solution.

### 7.3.5. Conclusion

In conclusion, we developed solution process ZnO nanowire based MIS LED. Spin on glass effectively filled the gap of active emission layer of ZnO and performed as an insulator for accumulating electron charges at the interface. Threshold voltages increased with SOG layer thickness increase. Broadband light emission was observed under forward bias, possibly from defect related emission reported elsewhere [138-139]. Further characterization with variable annealing temperatures might lead to increased band edge ultraviolet emission. Since most process steps are low temperature based

solution process including insulator layer deposition, it would be compatible to make flexible MIS ZnO nanowire LED. This may lead to the development of low cost, but flexible ZnO UV or white light source for several consumer electronics applications. Also, we demonstrated in-situ fabricated LED device using microfluidic ZnO nanowire synthesis process. By growing different bandgap materials at each channel, we believe that this process can be used for multi color LED device in a flexible platform.

## 7.4. Full oxide Nanowire Photovoltaic Device

### 7.4.1. Introduction

Nanowire based photovoltaic cell has been of great interest because it has an advantages over conventional thin film devices by separating the light absorption length and exciton diffusion length [9, 141-142]. Optimized nanowire based photovoltaic cell can have a thick absorbing layer for full spectral absorption, and small nanowire spacing for short exciton diffusion. To create an ideal geometry, spatial control in the synthesis of semiconductor nanowires is really critical. However, conventional position control of Vapor-Liquid-Solid or hydrothermal nanowire growth is expensive and time consuming because electron beam lithography, which is a serial process, is required to form specific nucleation sites [70].

In this work, ZnO nanowire for full oxide photovoltaic cells are spatially controlled using self-assembled polystyrene-b-polymethylmethacrylate (PS-b-PMMA) diblock copolymer templates. Tunable spacing is controlled by the size of polymers. This scheme can be used for the nanowire synthesis with high precision tunable spacing in a massively parallel manner because the nucleation site is controlled by self assembly process. Compared to other process [11, 23, 143], the self assembled PS template also gives an additional advantage, providing insulation from the bottom ZnO seed layer for device integration. For a p-type material, cupric oxide ($Cu_2O$) was chosen because it is an earth abundant material that has shown a strong potential in thin film photovoltaic applications due to its direct bandgap energy (1.9~2.1 eV) [23, 144-146]. Theoretical conversion efficiency ($\eta$) of Cu2O solar cell is in the order of 20 %, comparable to Si [147]. By combining these two materials with defined nanostructures, we demonstrate a

low cost, yet efficient photovoltaic system.

### 7.4.2. Experiments

The schematic of the nanowire synthesis is shown in Figure 7.31. Up to ZnO nanowire synthesis in PS templates, the procedure is the same as described in chapter 5. After the nanowires were synthesized, $Cu_2O$ was conformally deposited by reactive DC magnetron sputtering with copper target in the presence of argon and oxygen. Finally, 100 nm thick Au ($Cu_2O$ side) and Au (ITO side) electrodes were deposited by e-beam evaporation with a shadow mask.

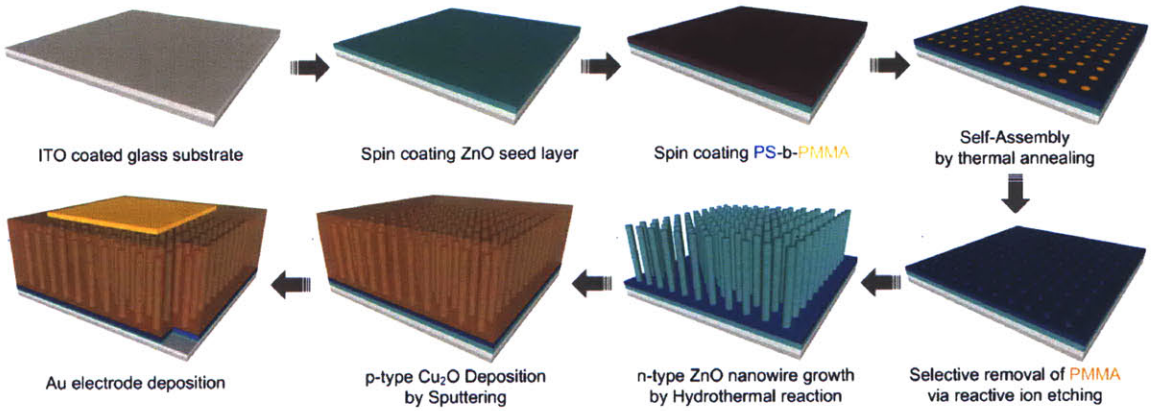


Figure 7.31. Procedure for nanowire embedded full oxide solar cell. A PS-b-PMMA block copolymer was spin coated on top of ZnO seed layer coated ITO substrate, and thermally annealed. Oxygen plasma removes PMMA, forming PS templates. The substrate is transferred to a supersaturated solution bath and grows ZnO nanowires only at seed layer exposed positions at temperature 60C~80C. $Cu_2O$ layer is deposited by DC reactive sputtering on top of ZnO nanowire, providing high interface area of p-n heterojunction. Finally, metal electrode is deposited using a shadow mask for the solar cell device.

$Cu_2O$ and ZnO nanowire structures were measured using Philips-FEI XL30-ESEM field emission scanning electron microscopy (SEM) with secondary electron detector in normal high vacuum mode. Crystalline structure and orientation of the nanowires was identified by X-ray diffractometry (XRD, Panalytical X'pert Pro) using

CuK$\alpha$ (1.5406Å) radiation. The current-voltage characteristics of the n-ZnO nanowire / p-$Cu_2O$ p-n heterojunction were measured with HP4156A semiconductor analyzer under dark or AM 1.5 solar simulator (SS50, Photo Emission Tech, Inc) with 120 mW/cm$^2$.

### 7.4.3. Results and Discussion

*7.4.3.1. DC reactive sputtering of $Cu_2O$*

Various parameters for $Cu_2O$ deposition were carried out to find high p type conductivity and crystallinity film. Sputtering power, gas pressure, Ar / $O_2$ ratio, and substrate temperature were parametrically tested to optimize a $Cu_2O$ deposition condition. Figure 7.32 shows XRD data of 500 nm thick $Cu_2O$ deposited on top of ZnO nanowires grown on ITO substrate by reactive DC sputtering of Cu target (AJA International, 99.99%) with 50 W, 4mTorr, 40 sccm $O_2$ / 15 sccm Ar at 250 C. Only Cu2O phases were observed without CuO or Cu phase.

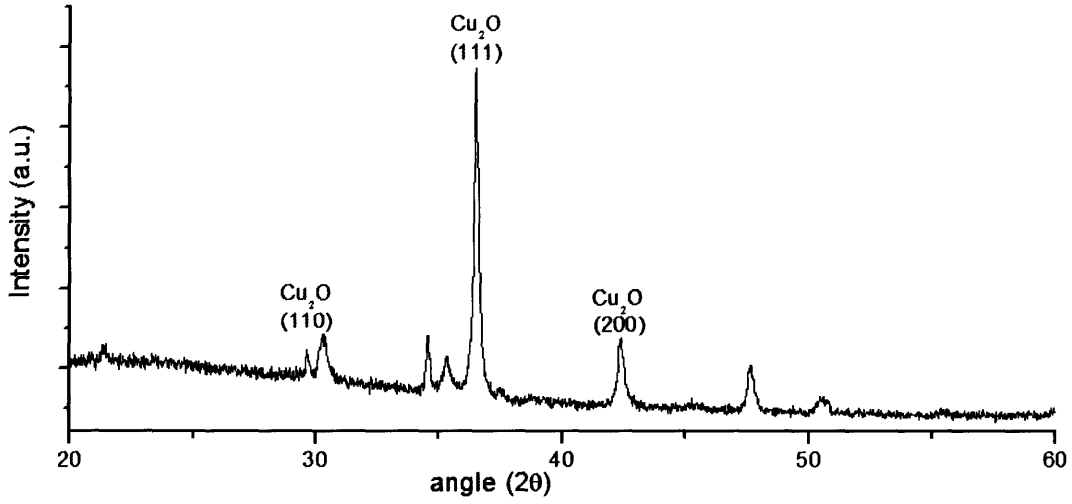


Figure 7.32. XRD pattern of $Cu_2O$ on top of ZnO nanowires grown on ITO glass substrate. Distinctive $Cu_2O$ peak indicates phase homogeneity. Other peaks corresponds to ZnO and ITO phase.

Under the $Cu_2O$ layer, ZnO nanowire structure was used to overcome the short minority carrier diffusion length of $Cu_2O$ by minimizing the photo generated carrier

travel distance. To achieve this goal, conformal filling of $Cu_2O$ in ZnO nanowire trenches is essential. Slow deposition rate, and additional RF bias [148-150] on the substrate was carried out to match this filling criteria. Figure 7.33 shows cross section image of $Cu_2O$ / ZnO interface by reactive DC sputtering of Cu target with 50 W, 4mTorr, 40 sccm $O_2$ / 9 sccm Ar at 250 C under 10W RF bias.

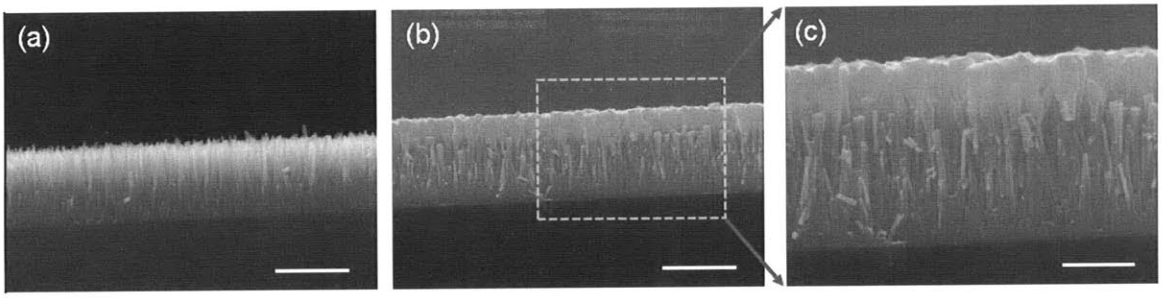


Figure 7.33. Cross sectional SEM of before (a) and after (b) conformal $Cu_2O$ deposition on ZnO nanowires grown on ITO substrate. Magnified image(c) shows $Cu_2O$ is penetrated under the tip of ZnO nanowires effectively. Scale bar = 1um (a and b), 500 nm (c).

*7.4.3.2. Electrical Characterization of full oxide nanowire photovoltaic cell*

Photovoltaic effects of 500nm thick p-$Cu_2O$/ 1.2 um thick n-ZnO nanowire devices were measured under illumination through ITO glass substrate. Figure 7.34 shows non linear J-V curve, indicating rectifying behavior of p-n heterojunction under dark condition. When light with 120 $mW/cm^2$ was illuminated, the device showed open circuit voltage of 0.153V and short circuit current density of 1.067 $mA/cm^2$. Fill factor was measured to be 41.16. The energy conversion efficiency was found to be 0.056 %. The value is similar to the device previously reported $Cu_2O$/ZnO nanowire solar sell using $Cu_2O$ nanoparticles for $Cu_2O$ layer with additional $TiO_2$ layer to prevent shorting [23]. In our case, self assembled PS polymer templates itself help preventing short circuit. Other researchers have demonstrated the energy conversion efficiency of 1.2 %with $Cu_2O$/ZnO thin film system using different deposition conditions [151]. We believe that

further optimization of $Cu_2O$ and ZnO nanowire doping and nanowire spacing would give higher energy conversion efficiency compared to thin film structures as others expected with different material sets [142, 152].

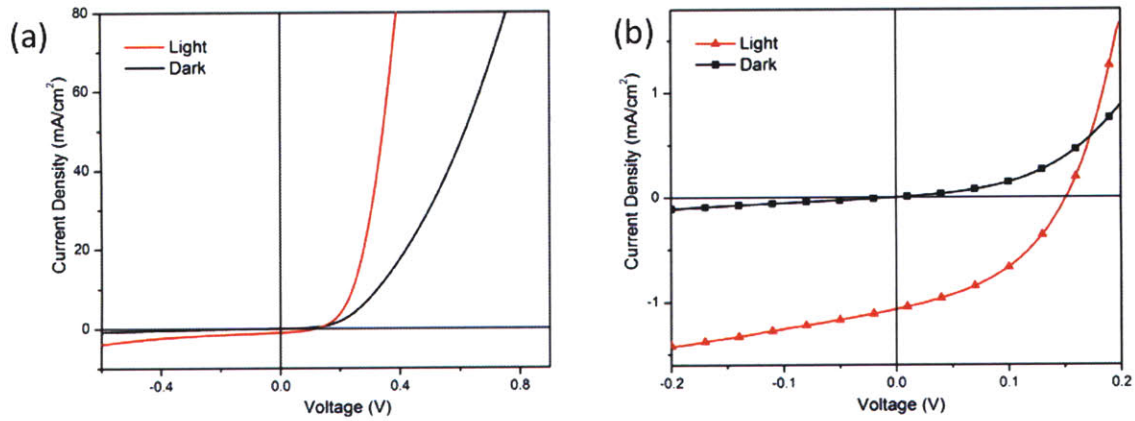


(c)

| sample | $J_{sc}$ (mA/cm²) | $V_{oc}$ (V) | Fill Factor | Efficiency ($\eta$) |
|---|---|---|---|---|
| ZnO NW/$Cu_2O$ | 1.067 | 0.153 | 41.16 | 0.056 % |

Figure 7.34. (a), (b) J-V characteristics of the p-$Cu_2O$/n-ZnO nanowire heterostructure photovoltaic cells under dark and AM 1.5G illumination with 120 mW/cm$^2$. (c) Measured photovoltaic cell performance.

### 7.4.5. Conclusion

In conclusion, full oxide based nanowire solar cell was demonstrated using ZnO nanowires. $Cu_2O$ sputtering with different conditions was tested to optimize filling between ZnO nanowire spacing. PS templates effectively prevented the device from shunting. By increasing the nanowire spacing with longer chain block copolymer, property control by annealing and effective doping would increase photovoltaic cell efficiency higher than 0.056 % reported here. Further optimized nanowire based structure would enable the light to be absorbed in the vertical direction while allowing exciton diffusion in lateral direction more effectively. In addition, $Cu_2O$ and ZnO are stable and

abundant materials. With these merits, this full oxide nanowire device may be useful as a low cost, long lifetime photovoltaic cells.

# Chapter 8 : Alternative Nanoscale Fabrications

This chapter is partially adopted from the following papers.

Jaebum Joo, Kimin Jun, and Joseph M. Jacobson, "Simple fabrication of UV nanoimprint templates using critical energy electron beam lithography," *J. Vac. Sci. Technol. B* 25(6), 2407-2411 (2007)

Jaebum Joo, Brian Y. Chow, and Joseph M. Jacobson, "Nanoscale Patterning on Insulating Substrates by Critical Energy Electron Beam Lithography," *Nano Lett.* 6(9), 2021-2025 (2006)

Jaebum Joo, SangJun Moon, and Joseph M. Jacobson, "Ultrafast patterning nanoparticles by electrostatic lithography," *J. Vac. Sci. Technol. B* 24(6), 3205-3208 (2006)

In this section, I will describe alternative nanoscale fabrication methods that can be adapted for high precision and low cost process. The following two novel processes would enable the precise control of nanowire growth position for further applications.

## 8.1. Critical energy Electron Beam Lithography

Electron beam (e-beam) lithography is a powerful tool for nanoscale fabrication, but its applicability to insulating substrates is often limited because of surface charging effects. Unlike patterning on conducting substrates that dissipate excess charge as the beam passes through the resist, charge is trapped near the surface when the substrate is insulating. This charging causes an unbalanced surface potential of the resist [153-157] that deflects the beam and causes severe pattern distortion [158-162]. Several methods have been employed to prevent the pattern distortion, most commonly the use of a conductive layer above the resist [163-165] that requires additional processing steps, and the use of conducting polymers as the resist itself [166-168]. A third approach, known as environmental SEM (ESEM), delivers gas molecules into the chamber that are ionized upon e-beam impact and neutralize surface charging [169-173], but it requires a differentially pumped electron beam column and a sophisticated gas delivery system.

Critical Energy Electron Beam Lithography (CEEBL) [174] was developed to e-beam patterning on nanoscale features directly on non conducting substrates. In CEEBL, the e-beam lithography is operated at the critical energy ($E_2$) of the resist on the insulator, which is the energy that has a dynamic charge balance between incoming electrons and outgoing electrons, thereby leaving the surface charges neutral (Figure 8.1). Therefore, insulators such as glass or large bandgap materials can be directly patterned without pattern distortion by surface charging.

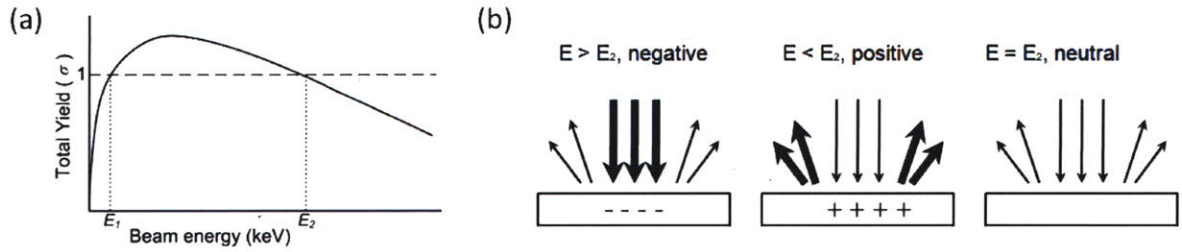


Figure 8.1. Principles of Critical Energy Electron Beam Lithography. (a) Total electron yield ($\boldsymbol{\sigma}$) versus beam energy for a typical polymer resist. The substrate is negatively charged when $\boldsymbol{\sigma} < 1$, positively charged when $\boldsymbol{\sigma} > 1$. The dynamic charge of the substrate is zero at the critical energy ($E_1$, $E_2$) when $\boldsymbol{\sigma}$ is unity. (b) Schematic of charging at different beam energies.

Figure 8.2 shows how CEEBL can effectively minimize pattern distortion induced by charging effects. When the feature was patterned at critical energy (1.3 keV with 65 nm PMMA on glass), almost no pattern distortion was observed compared to other beam energies that has a noticeable pattern shift that can be detrimental for many device applications.

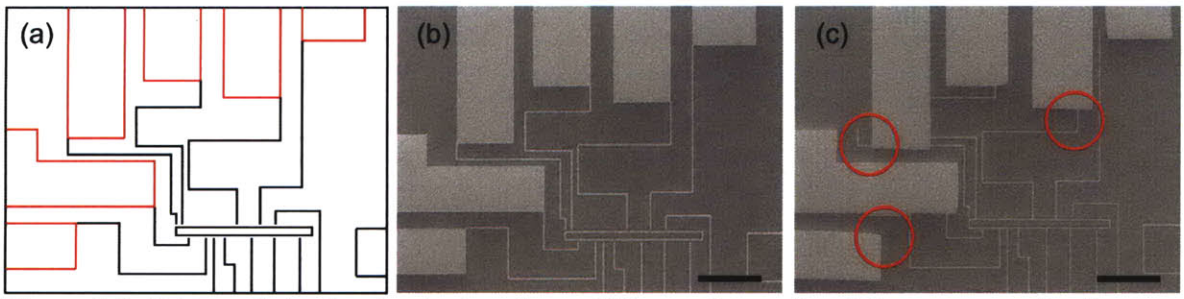


Figure 8.2. Pattern distortion in electron beam lithography on insulators as a result of surface charging. (a) Design of the desired pattern. SEM images of 10 nm thick Au electrodes on glass after lift-off of PMMA patterned at (b) 1.3 keV ($E_2$) and (c) 5 keV. Charge induced pattern distortions are prominent at 5 keV (circled). Scale bar = 10 μm.

Beam deflection at various voltages was measured by a method previously reported by Craighead and co-workers-workers [158] to quantify the CEEBL performance. Briefly, two reference single pass lines were first patterned, then large charge pads with at 30 $\mu C/cm^2$ were patterned. Finally, a third single pass was patterned

between two reference lines. Deflection of the last line was measured by SEM after PMMA development followed by 5 nm Au deposition. As can be seen from Figure 8.3(b), deflection is practically eliminated at critical energy compared to other energies which showed largely deflection either by positive (at $E < E_2$) or negative ($E > E_2$) charging.

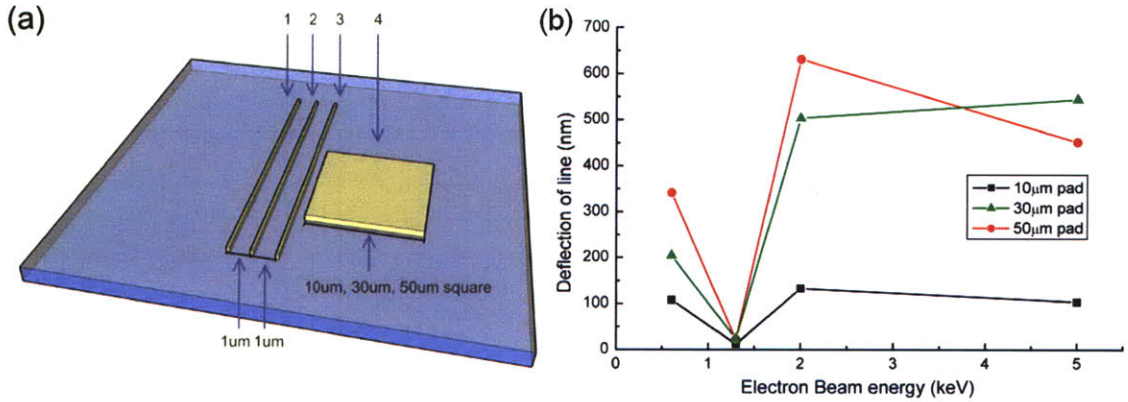


Figure 8.3. Beam deflection at various voltages. Two parallel single-pass reference (1 and 3) lines were first patterned with a 2 μm gap, followed by charge pads (4) written at 30 $\mu C/cm^2$ Finally, a third single-pass line was patterned between the pad and the reference line. 5 nm Au was evaporated after developing the PMMA and imaged under SEM to determine the line deflection. The deflection was virtually eliminated at $E_2$ = 1.3 keV, whereas the beam was largely deflected due to positive surface charging below $E_2$ and negative charging above it.

To demonstrate potential applications of CEEBL, we created binary chemical patterns for selective protein adhesion for high-density arrays that do not quench fluorescence [175]. Briefly, the developed areas of patterned PMMA on thermal oxide were first silanized with 0.5 % octadecyltrichlorosilane (OTS, Aldrich) in carbon tetrachloride, which is a PMMA non-solvent. The long alkyl chains of the OTS self-assembled monolayer (SAM) promote protein adhesion. After stripping the PMMA in methylene chloride, the remaining unsilanized areas were passivated with 1 % PEG-silane (Gelest) in tetrahydrofuran to prevent protein fouling or non-specific adsorption.

Figure 8.4 shows a confocal fluorescence image (Zeiss LSM Pascal) of immobilized Alexa-Fluor 546 / streptavidin conjugate (Molecular Probes) in an array of 400 nm spots on a 2400 nm pitch after soaking for one hour at room temperature (2 μg / mL in PBS buffer).

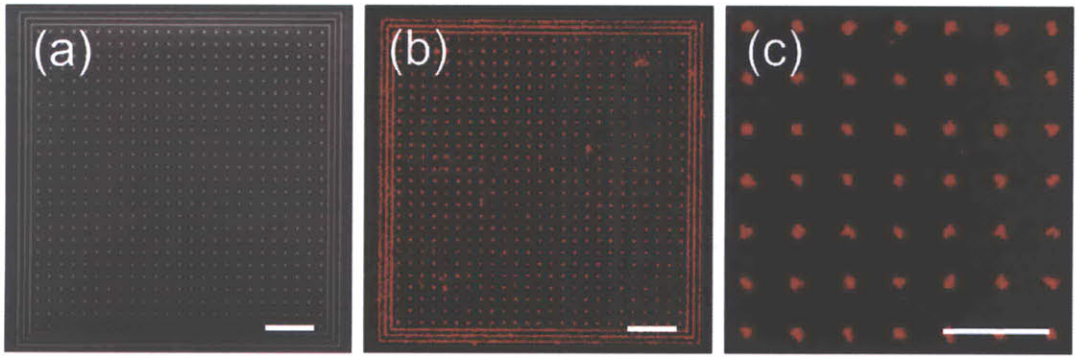


Figure 8.4. (a) PMMA pattern on a thermal oxide with 400 nm spots on a 2.4 um pitch by CEEBL process (b,c) Confocal fluorescence image of an array of AlexaFluor-546 / streptavidin conjugate. A binary chemical pattern for selective protein adhesion was created by first modifying the developed areas of patterned PMMA on thermal oxide with octadecyltrichlorosilane to promote protein adhesion, and then PEG-silane after stripping the resist to prevent non-specific adsorption. (a,b) Scale bar = 10 μm. (c) Scale bar = 5μm.

We also developed a novel method to fabricate nanoimprint mold using CEEBL lithography [176]. HSQ was used as a part of direct UV nanoimprint mold, and directly patterned to quartz substrate to form UV nanoimprint templates.

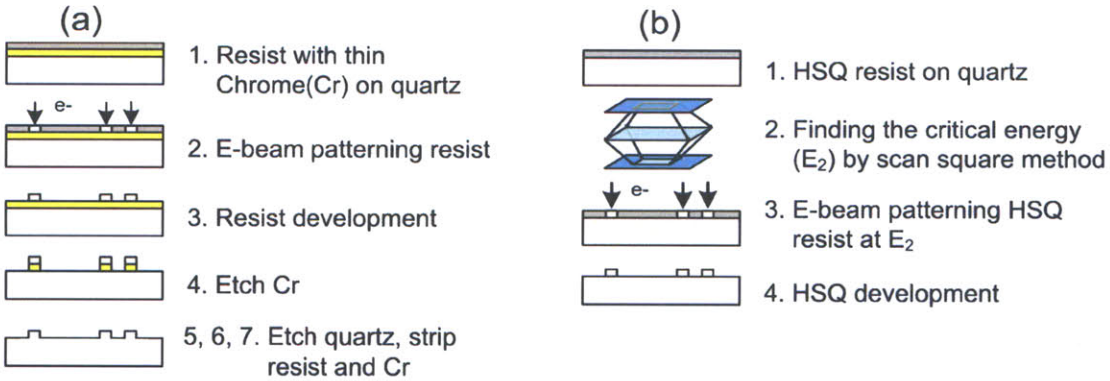


Figure 8.5. Comparison of process flows between a conventional chrome based template (a) and a CE-EBL based template (b). The template fabrication process is simplified by CE-EBL with HSQ additive processing.

High precision imprinting was observed using this simple UV nanoimprint template with SU-8 (Microchem) UV curable resin (Figure 8.6). The imprinted structure shows the high replication fidelity. Even after several UV imprinting steps, the HSQ which is a part of the mold showed no apparent damage by SEM analysis.

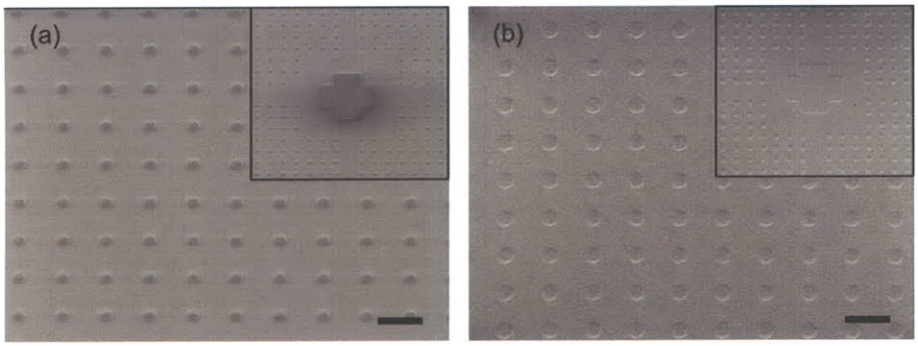


Figure 8.6. High imprinting fidelity with CE-EBL based UV-NIL templates. 30 degree tilted low voltage SEM images of UV-NIL templates with 500 nm diameter spots on a 2 μm pitch (a) and the replicated structure of SU-8 on 1 μm thermal oxide (b). Scale bar = 2 μm.

In conclusion, we have demonstrated the use of CEEBL to pattern nanostructures on insulating substrates. The pattern distortion from surface charging was minimized by the precise control of the electron beam energy, eliminating the need for additional charge dissipation layers or sophisticated gas delivery systems. This method of nanoscale patterning on insulators and wide band gap materials has potential applications in position controlled nanowire synthesis, high-density biochips, flexible polymeric electronics, and optoelectronics.

## 8.2. Ultrafast patterning of nanoparticles by electrostatic Lithography

Nanoscale building blocks such as nanoparticles, nanowires, and carbon nanotubes have been of great interest recently because of their special material properties [177-179]. In order to assemble nanoparticles into functional devices, many researchers

have used several approaches such as structural templates [180], DNA hybridization [181-182], and electrostatic interactions [183-190]. Patterning via electrostatic interaction is a particularly simple process. When a non-conducting substrate has a charge pattern on it, nanoparticles with opposite charges are attracted to the charge patterned area. Jacobs *et al.* [191] successfully demonstrated patterning charges on silicon oxide by using Atomic Force Microscopy (AFM) tips, but AFM is a serial process and may be too slow for fabricating functional devices with nanoparticles. To overcome yield and throughput issues, researchers have used metal coated polydimethylsiloxane (PDMS) stamps [189] to generate surface charges on the contacted area. However, making uniform contact over large areas when printing and embossing fine features can be difficult. Fudouzi *et al.* have used electron beams [185, 190] and ion beams [187, 192] to generate charge patterns on calcium titanate ($CaTiO_3$) to attract pre-charged or polarizable nanoparticle suspensions with ~20 μm resolution.

In order to better the resolution of electron beam (e-beam) generated charge patterns, we incorporated a Low Voltage Scanning Electron Beam Microscopy (LVSEM) [156, 193-194] method to find an e-beam energy that balances charge pattern resolution with throughput. Moreover, we introduced an electrospray technique [195-196], which is commonly used in mass spectroscopy for generating charged nanoparticles of any type. In electrospray, an aerosol of charged droplets is created by biasing a solution at a large potential. As the droplets evaporate, the charge per unit volume reaches a critical point, and each droplet explodes into smaller droplets that can be nanometers in diameter. In effect, almost any nano-material can be delivered as a charged species regardless of its intrinsic polarizability or charge, thereby vastly increasing the set of materials that can be

patterned by electrostatic lithography. By coupling e-beam charge patterning with electrospray, we successfully patterned inherently neutral silver nanoparticles at area doses as low as 50 nC/cm$^2$ [197].

Schematic process of the process is shown in Figure 8.7. The critical energy of the thick PMMA on the Si substrate was measured by variable magnification scanning method [156, 198] with a FEI-XL30 ESEM in standard operating mode. After $E_2$ was measured, a "latent" negative charge pattern on the substrate was generated by e-beam irradiation at 2 keV, which is higher than $E_2$, with a dose of 50 nC/cm$^2$ using Nabity NPGS pattern generator. Positively charged silver nanoparticles were generated by an electrospray technique in which a 10 % solution of silver nanoparticle colloids in hexane was sprayed through a 15 μm diameter silica capillary tip (New Objective, Inc.) with a flow rate of 40 μL/hr at an applied potential of 4.5 kV. The electrospray apparatus and the charged substrate were spaced by 5cm to ensure the fine droplet generation and the attractive force between the droplets and the charged area. Patterned nanoparticles on the substrate were observed by SEM operating at $E_2$.

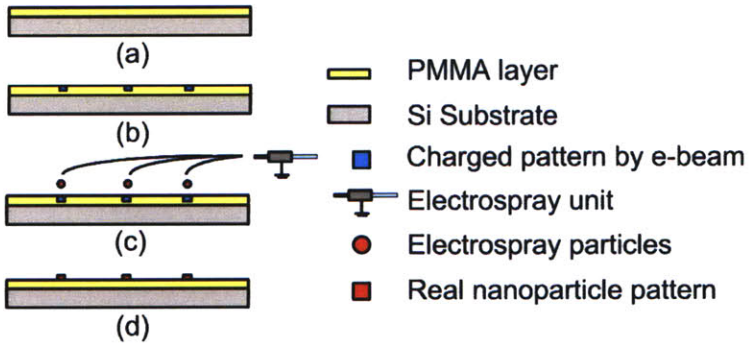


Figure 8.7. Schematic process of electrostatic lithography. (a) The PMMA layer (2.3 μm) was spin coated and hard baked, (b) Charge patterns were generated with a 2 keV electron beam with a dose of 50 nC/cm$^2$, (c) positively charged droplets of neutral silver nanoparticles were generated and deposited to the "latent" charge pattern image by electrospray, (d) a real pattern is generated by electrostatic attraction.

Figure 8.8 shows the AFM surface topography and KPM surface potential of the same area after charge pattern generation at 2 keV with a dose of 50 nC/cm$^2$. As can be seen in Figure 8.8(a), almost no surface damage was observed after e-beam irradiation. The measured height difference due to irradiation was ~0.26 nm. When the dose was increased up to 1 μC/cm$^2$, a much more significant height difference (~56 nm) was measured, indicating a large amount of beam-induced surface damage. To eliminate any physical effects rather than electrostatic interactions, such as selective nanoparticle adhesion to damaged areas, the charge pattern dose was fixed at 50 nC/cm$^2$. As shown in Figure 8.8(b), Negative surface charge patterns generated by 2 keV e-beam were clearly measured by with full width at half maximum (FWHM) of ~900 nm.

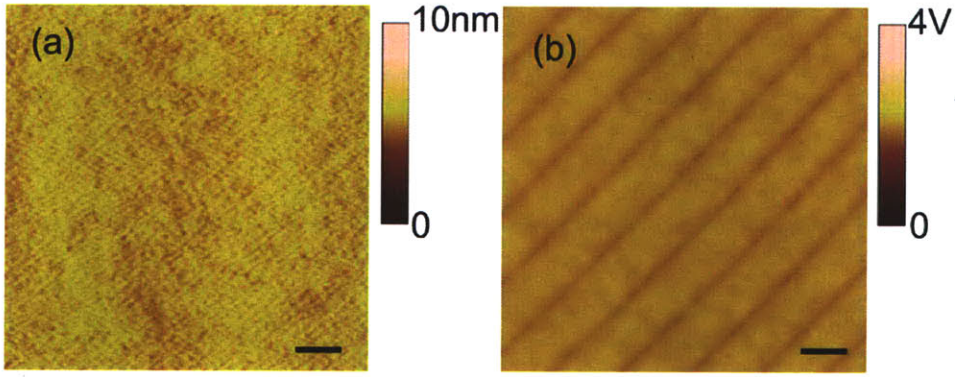


Figure 8.8. AFM topography image (a) and KPM surface potential image (b) of the same area after e-beam irradiation at 2 keV with a dose of 50 nC/cm$^2$. Lines of negative surface potential with ~900nm width were generated without any apparent damage to the surface. Scale bar = 5 μm.

Using the defined charge patterns, silver nanoparticles were deposited to the charged pattern area using custom built electrospray apparatus. Arbitrary nested patterns with 700 nm width were fabricated by electrostatic lithography. As seen from the Figure 8.9, a large overall area can be uniformly covered by electrospray within seconds.

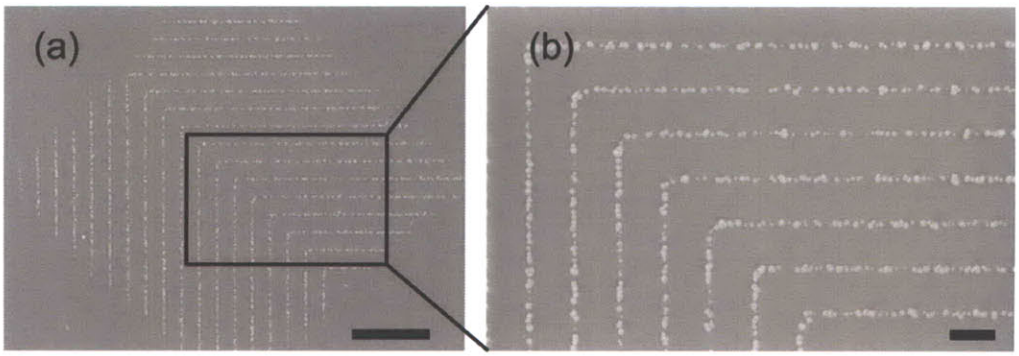


Figure 8.9. SEM images after positively charged silver nanoparticles were sprayed on to the negatively charged e-beam pattern. 0.7 μm thick lines were generated over a large area with doses as low as 50 $nC/cm^2$, showing the feasibility of ultrafast patterning by electrostatic lithography. (a) Scale bar = 50 μm. (b) Scale bar = 10 μm.

Since the dose (50 $nC/cm^2$) used for patterning was several orders of magnitude lower than typical e-beam resist doses, electrostatic lithography has great potential in the rapid patterning of nanoparticles, carbon nanotubes, or nanowires at large scales. Also, this ultrafast nanoparticle deposition method will lead toward the massive parallel nanowire synthesis with defined positions by forming local catalyst for the VLS nanowire growth.

# Chapter 9 : Summary and Future work

In this section, I will conclude my thesis work by summarizing what have been investigated and suggesting possible works for the future research directions.

## 9.1. Summary

Based on the fundamental understanding that crystal growth happens under supersaturation condition, we tested whether hydrothermal ZnO nanowire growth follows thermodynamic heterogeneous nucleation and growth process. Solubility with three different parameters was calculated based on possible chemical reactions in the solution, and parametric experiments were performed to find relationship between the growth rate and the calculated supersaturation value. Within experiment conditions, we observed that all empirical data fits to the supersaturation dependent heterogeneous growth. Optical and crystalline properties of ZnO nanowires were also measured.

To tune the morphologies of ZnO nanostructure synthesis in a hydrothermal condition, we evaluated the effect of additional cations during synthesis. Dramatic morphology and aspect ratio change were observed when additional cations were introduced in hydrothermal process. Using more complex chemical reactions, we calculated multiple charged ion complex distributions and developed an electrostatic competing ion model to explain how the growth morphology changes with different cation addition. Orientation dependent ZnO surface polarities were measured to support the validity of the suggested model using AFM and XPS analysis.

Spacing control of hydrothermal nanowire synthesis was tested using self assembled block copolymer templates. PS-b-PMMA block copolymer was self assembled to form cylindrical PMMA dots in PS matrix, and selective etching was performed to expose bottom ZnO seed layer. ZnO nanowires were grown only at PMMA etched

region, indicating usefulness of self assembly in spatial control of nanowires. However, the nanowire alignment was poorer than the sample without PS matrix. More thorough experiments would be necessary to optimize the spacing and thickness of block copolymer to solve nanowire alignment issue.

Fluidic control of nanowire synthesis was tested by applying microfluidics in a hydrothermal system. Dynamic flow of chemical reactants gave different growth behavior from the static bulk nanowire synthesis. Growth rate was enhanced by factor of ten or more compared to the static condition, and also growth rate gradient was observed with respect to the distance from the inlet. Finite element modeling simulation was used to fit the experimental results, and nanowire synthesis with more complex geometry was demonstrated.

Based on the rational understanding of hydrothermal ZnO nanowire synthesis, we developed several different devices. Field emission devices were tested using several different aspect ratio nanowires, and highest aspect nanowire device showed threshold field values similar to CNT field emission devices. Field enhanced electron emission was pronounced with higher aspect ratio device as expected. We also developed a novel nanowire embedded alternative current electroluminescent device. Instead of flat dielectric, we inserted ZnO nanowires to improve ZnS:Mn phosphor light emission efficiency by field enhanced electron transport and impact ionization. Higher aspect ratio nanowire embedded devices shows decrease in turn on voltage at least hundred volts, and energy efficiency was improved by factor of ten or more. Metal/insulator/semiconductor LED device using ZnO nanowire as active light emission layer was developed also. Using spin on glass as a thin insulator for electron block layer, we showed successful

light emission from the device. Depending on the insulator thickness, threshold voltage and current density changed. The optimization of annealing and deposition condition is still required for further improvement. Using self assembled block copolymer templates, we developed a cost effective full oxide photovoltaic device with $Cu_2O$/ZnO nanowires. Nanowires were used to maximize light absorption and minimize exciton diffusion length. We successfully demonstrated photocurrent, but conversion efficiency was lower than Si based photovoltaics. Optimization of ZnO spacing, doping, and $Cu_2O$ doping and annealing would be necessary to enhance the performance of the solar cell.

Finally, alternative novel nanoscale fabrication techniques were demonstrated. By adjusting electron beam energies, nanostructures were successfully fabricated on non conducting substrates without charge dissipation layers. As a new assembly method, nanoparticles were electrostatically attracted to the charge patterns generated by electron beams. These two techniques may lead to precise position control of nanowire growth for new applications.

## 9.2. Future work

Although thermodynamic supersaturation model and electrostatic competing ion model were successful to describe the morphology controlled ZnO nanowire synthesis in hydrothermal reaction, many other works have been still left as open questions. The following sections describe possible applications and researches which this thesis work may be related and useful for further improvement.

### 9.2.1. Materials development

Based on the fundamental understanding of hydrothermal ZnO nanowire synthesis, other important nanowire materials can be evaluated. We believe that similar

approach of supersaturation calculation and competing ion model would be still valid with other oxide materials including $TiO_2$, CuO, and MgO. As a test experiment, we tried synthesizing $TiO_2$ nanowires in highly acidic solution with hydrothermal process. Figure 9.1 shows $TiO_2$ nanowires synthesized in hydrothermal process with 1 mL titanium isopropoxide (TTIP) in 30 mL DI water, and 30 mL 35 wt% HCl for 27 hrs at 90 C. Similar to ZnO seed layer, this time the seed layer was thin layer of Ti (60 nm) on Si substrate by RF sputtering. XRD data shows several peaks of rutile structure $TiO_2$. More various chemical compositions, seed layer control, and thermodynamic analysis may give similar rational controllability of $TiO_2$ nanostructures useful for improving current $TiO_2$ applications such as photocatalysis, dye sensitized solar cell, UV absorbant, and others. Moreover, rational control of several different materials with hydrothermal process in the future may lead to the development of various new applications as we demonstrated using ZnO nanowires.

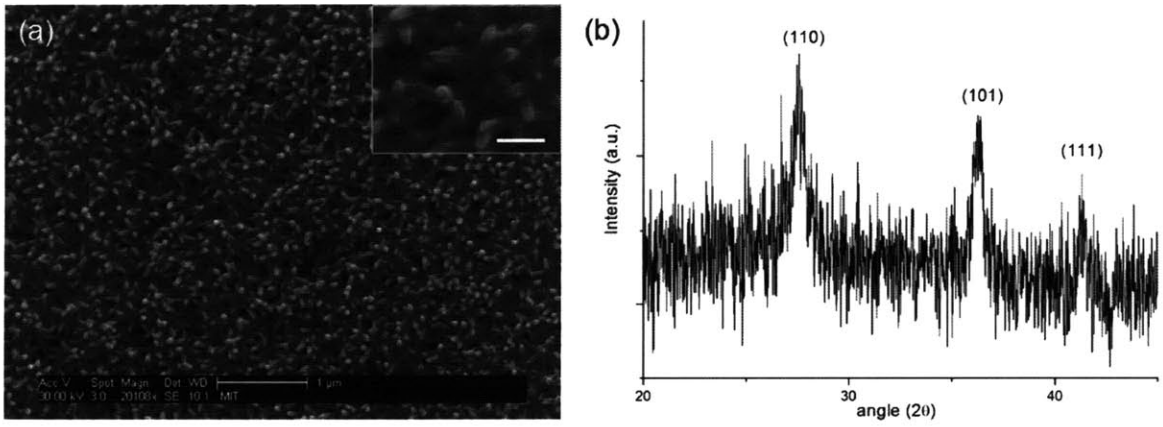


Figure 9.1. (a) SEM images of $TiO_2$ nanowires hydrothermally grown on Ti deposited Si substrate. Inset scale bar = 200 nm. (b) XRD data of nanowires grown on Si substrate indicating rutile $TiO_2$ crystalline phase.

### 9.2.2. Processing Development

There are several improvements to be made in terms of processing of nanowire synthesis in a hydrothermal system.

Position controlled synthesis is one of the key aspects, and we demonstrated block copolymer self assembly as a template positioning specific seed layer locations. Only preliminary result with fixed spacing was demonstrated in this thesis, but varying the spacing in a larger/smaller scale would give more control over performance in real applications. For example, nanowire based solar cell need specific spacing between nanowires to effectively increase light absorption efficiency and decrease charge carrier diffusion length. As an alternative, massively parallel nanoimprint process, local catalyst deposition by electrostatic system, or polymer dewetting may be an option to create regular array with defined spacing in low cost device system. UV nanoimprint mold using CEEBL system and nanoparticle patterning with electrospray system may be applicable for the fast and parallel control of nanowire spacing. In case of polymer dewetting, since the exposed area would be inversed pattern instead of holes, another step to deposit a growth blocking layer, and etching dewetted polymers would be required. Chemical stability of polymers and other layers under chemical reaction condition need to be evaluated also.

More thorough experiments of microfluidic nanowire synthesis would lead to an important understanding of chemical reaction coupling with fluid dynamics. Even though we were able to analyze a nanowire growth in a simple linear microfluidic channel system, it is still unclear how it behaves under complex geometry fluidic system. More detailed work may lead to the development of real programmable nanowire growth with specific locations. By applying this microfluidic growth, new interesting

applications such as position sensor with gradient control of nanowire in linear scale, analog particle sorting, two dimensional UV photo detectors, and others may be developed.

### 9.2.3. Applications Development

There are several new applications that might be benefit from the rational control of nanostructures with hydrothermal system.

Nanowire ACEL device showed possibility of nanostructures to be adapted into real industry market. Optimizing the phosphor and dielectric deposition conditions, nanowire height and spacing, and device assembly are still necessary to match the current commercial ACEL devices. High temperature and moisture durability, and low fabrication cost of nanowire ACEL device would be useful for robust display for military, car display, and information display at harsh environment with extreme temperature changes.

Hydrothermally synthesized nanowire based photovoltaic system may lead to the development of low cost, environment friendly fabrication for alternative energy sources. Even though ZnO nanowire was used at this thesis work, other nanowire materials would improve efficiency of solar cell because ZnO itself only absorbs UV regime light. $Cu_2O$ nanowire is one of the possible candidates for its abundance in earth, and huge absorption in solar spectrum light.

Rechargeable zinc air battery may be a future research that may be related to morphology controlled ZnO nanowire synthesis. New battery development has been a great issue recently, and researchers and companies started to look into different materials other than lithium ion battery. Zinc air battery has been in the market for a

while, mainly used for hearing aids. It consists of zinc, electrolytes, and holes for oxygen exchange. It has many advantages over conventional batteries including high energy density (~442Wh/kg, twice than $Li^+$ battery), flat discharge profile, excellent shelf life, and intrinsically safe. However, it has a rechargeability issue, so it is generally disposed after one time usage. When discharge happens, zinc transforms into zinc hydroxide, then zinc oxide and release electrons. Problem occurs when recharging occurs, because zinc oxide turns into zinc dendrite, thereby forming short circuits and decrease active zinc around the reaction surface. Some companies[199] and patents described that adding calcium zincate salts minimize this problem, and we expect that it is analogous to ZnO growth with different cation addition. Zinc air battery rechargeability issue may be solved by semi-empirical approach with fundamental understanding of solubility of zinc oxide and dissolution within competing ions.

# Chapter 10 : Appendix

## 10.1. Matlab codes for thermodynamic calculations

### 10.1.1. ZnO solubility plot code

```
%Main code

clear;
close all
tic

global OH Kzh1 Kzh2 Kzh3 Kzh4 Kzn1 Kzn2 Kzn3 Kzn4 Kzhn Kzox Cn

%values definition
Kzh1=5.0;
Kzh2=11.1;
Kzh3=13.6;
Kzh4=14.8;
Kzn1=2.21;
Kzn2=4.5;
Kzn3=6.86;
Kzn4=8.89;
Kzhn=4.39;
Kzox=-15.52;
number=100;
Cn=-0.1;
Rmax=5; % Nitrogen concent change numbers
step=14/(number-1); %internal variable
k=0:step:step*(number-1);

% allocate storage space
Z = zeros(number,Rmax);
ZOH1 = zeros(number,Rmax);
ZOH2 = zeros(number,Rmax);
ZOH3 = zeros(number,Rmax);
ZOH4 = zeros(number,Rmax);
ZN1 = zeros(number,Rmax);
ZN2 = zeros(number,Rmax);
ZN3 = zeros(number,Rmax);
ZN4 = zeros(number,Rmax);
NH3 = zeros(number,Rmax);
Ztot = zeros(number,Rmax);

NZ = zeros(number,Rmax);
NZOH1 = zeros(number,Rmax);
NZOH2 = zeros(number,Rmax);
NZOH3 = zeros(number,Rmax);
NZOH4 = zeros(number,Rmax);
NZN1 = zeros(number,Rmax);
NZN2 = zeros(number,Rmax);
NZN3 = zeros(number,Rmax);
NZN4 = zeros(number,Rmax);
NZChP = zeros(number,Rmax);
NZChN = zeros(number,Rmax);
NZNonCh = zeros(number,Rmax);
```

```
for j=1:Rmax
    Cn=Cn+0.1;  % Total N change step
    for i=1:number
        pH=step*(i-1);
        OH=10^-(14-pH);

        %solver
        x0 = 0;
        options = optimset('Display',
'off','NonlEqnAlgorithm','dogleg','LargeScale','off', 'MaxFunEvals',
5000, 'MaxIter', 500, 'TolFun', 1e-9, 'TolX', 1e-4);
        [S, fval, exitflag, output]
=fsolve(@nle_revisit,x0,options);      % S(1)-> NH3

        switch exitflag
            case 0
                disp('Number of iternation, evaluation exceeded');
            case -1
                disp('Algorithm terminated by output function');
            case -2
                disp('Algorithm appears to be converging a noon-root
point.');
            case -3
                disp('Trust radius became too small.');
            case -4
                disp('Line search error.');
        end

        %result
        Z(i,j) = (OH^-2)*(10^Kzox);  % [Zn2+]
        NH3(i,j) = S(1); % [NH3]
        ZOH1(i,j)=Z(i,j)*OH*10^Kzh1;          % [Zn(OH)+]
        ZOH2(i,j)=Z(i,j)*(OH)^2*10^Kzh2;    % [Zn(OH)2]
        ZOH3(i,j)=Z(i,j)*(OH)^3*10^Kzh3;     % [Zn(OH)3 -]
        ZOH4(i,j)=Z(i,j)*(OH)^4*10^Kzh4;     % [Zn(OH)4 2-]
        ZN1(i,j)=Z(i,j)*(NH3(i,j))*10^Kzn1;  % [Zn(NH3) 2+]
        ZN2(i,j)=Z(i,j)*(NH3(i,j))^2*10^Kzn2;    % [Zn(NH3)2 2+]
        ZN3(i,j)=Z(i,j)*(NH3(i,j))^3*10^Kzn3;   % [Zn(NH3)3 2+]
        ZN4(i,j)=Z(i,j)*(NH3(i,j))^4*10^Kzn4;   % [Zn(NH3)4 2+]

Ztot(i,j)=log10(Z(i,j)+ZOH1(i,j)+ZOH2(i,j)+ZOH3(i,j)+ZOH4(i,j)+ZN1(i,j)
+ZN2(i,j)+ZN3(i,j)+ZN4(i,j));

        NZ(i,j) = Z(i,j)/[10^Ztot(i,j)];
        NZOH1(i,j) = ZOH1(i,j)/[10^Ztot(i,j)];
        NZOH2(i,j) = ZOH2(i,j)/[10^Ztot(i,j)];
        NZOH3(i,j) = ZOH3(i,j)/[10^Ztot(i,j)];
        NZOH4(i,j) = ZOH4(i,j)/[10^Ztot(i,j)];
        NZN1(i,j) = ZN1(i,j)/[10^Ztot(i,j)];
        NZN2(i,j) = ZN2(i,j)/[10^Ztot(i,j)];
        NZN3(i,j) = ZN3(i,j)/[10^Ztot(i,j)];
        NZN4(i,j) = ZN4(i,j)/[10^Ztot(i,j)];
        NZChP(i,j) =
NZ(i,j)+NZOH1(i,j)+NZN1(i,j)+NZN2(i,j)+NZN3(i,j)+NZN4(i,j);
```

```
        NZChN(i,j) = NZOH3(i,j)+NZOH4(i,j);
        NZNonCh(i,j) = NZOH2(i,j);
    end


plot(k,NZ(:,j),k,NZOH1(:,j)',k,NZOH2(:,j)',k,NZOH3(:,j)',k,NZOH4(:,j)',
k,NZN1(:,j)',k,NZN2(:,j)',k,NZN3(:,j)',k,NZN4(:,j)');
    xlabel('pH')
    ylabel('Normailzed Zn ion complexes')
    title('Zn ion complexs distribution ')
    figure

    plot(k,NZChP(:,j),k,NZChN(:,j),k,NZNonCh(:,j)');
    xlabel('pH')
    ylabel('charge/non charge complexes')
    title('Zn ion complexs distribution ')
    figure

end

for j=1:Rmax
    plot(k,Ztot(:,j))
    xlabel('pH')
    ylabel('Total [Zn]')
    title('Zn solubility plot')
    hold on
end

toc;


%Sub function code

function F=nle_revisit(x)
% x(1) : NH3
global OH Kzh1 Kzh2 Kzh3 Kzh4 Kzn1 Kzn2 Kzn3 Kzn4 Kzhn Kzox Cn

    Z=(OH^-2)*(10^Kzox);

    %equations
    NH4=x(1)*(1/OH)*(10^-Kzhn);
    ZN1=Z*(x(1))*(10^Kzn1);
    ZN2=Z*((x(1))^2)*(10^Kzn2);
    ZN3=Z*((x(1))^3)*(10^Kzn3);
    ZN4=Z*((x(1))^4)*(10^Kzn4);

    F(1)=NH4+x(1)+ZN1+2*ZN2+3*ZN3+4*ZN4-Cn;      % Total NH3 to be
setup
```

### 10.1.2. ZnO/CdO mixed condition solubility plot code

```
% Main Code
```

```
clear;
close all
tic

global OH Kzhn Cn Kzh1 Kzh2 Kzh3 Kzh4 Kzn1 Kzn2 Kzn3 Kzn4 Kzox Kcdh1
Kcdh2 Kcdh3 Kcdh4 Kcd2h1 Kcd4h4 Kcdn1 Kcdn2 Kcdn3 Kcdn4 Kcdn5 Kcdox

%values definition
Kzh1=5.0;
Kzh2=11.1;
Kzh3=13.6;
Kzh4=14.8;
Kzn1=2.21;
Kzn2=4.5;
Kzn3=6.86;
Kzn4=8.89;
Kzox=-15.52;

Kcdh1=4.1;
Kcdh2=7.7;
Kcdh3=10.3;
Kcdh4=12.0;
Kcd2h1=4.6;
Kcd4h4=23.2;
Kcdn1=2.62;
Kcdn2=4.79;
Kcdn3=6.16;
Kcdn4=7.1;
Kcdn5=6.9;
Kcdox=-14.29;

Kzhn=4.39;
number=100;
Cn=-0.02;
Rmax=3; % Nitrogen concent change numbers
step=14/(number-1); %internal variable
k=0:step:step*(number-1);

% allocate storage space
NH3 = zeros(number,Rmax);

Z = zeros(number,Rmax);
ZOH1 = zeros(number,Rmax);
ZOH2 = zeros(number,Rmax);
ZOH3 = zeros(number,Rmax);
ZOH4 = zeros(number,Rmax);
ZN1 = zeros(number,Rmax);
ZN2 = zeros(number,Rmax);
ZN3 = zeros(number,Rmax);
ZN4 = zeros(number,Rmax);
Ztot = zeros(number,Rmax);

NZ = zeros(number,Rmax);
NZOH1 = zeros(number,Rmax);
NZOH2 = zeros(number,Rmax);
```

```
NZOH3 = zeros(number,Rmax);
NZOH4 = zeros(number,Rmax);
NZN1 = zeros(number,Rmax);
NZN2 = zeros(number,Rmax);
NZN3 = zeros(number,Rmax);
NZN4 = zeros(number,Rmax);
NZChP = zeros(number,Rmax);
NZChN = zeros(number,Rmax);
NZNonCh = zeros(number,Rmax);

Cd = zeros(number,Rmax);
CdOH1 = zeros(number,Rmax);
CdOH2 = zeros(number,Rmax);
CdOH3 = zeros(number,Rmax);
CdOH4 = zeros(number,Rmax);
Cd2OH1 = zeros(number,Rmax);
Cd4OH4 = zeros(number,Rmax);
CdN1 = zeros(number,Rmax);
CdN2 = zeros(number,Rmax);
CdN3 = zeros(number,Rmax);
CdN4 = zeros(number,Rmax);
CdN5 = zeros(number,Rmax);
Cdtot = zeros(number,Rmax);

NCd = zeros(number,Rmax);
NCdOH1 = zeros(number,Rmax);
NCdOH2 = zeros(number,Rmax);
NCdOH3 = zeros(number,Rmax);
NCdOH4 = zeros(number,Rmax);
NCd2OH1 = zeros(number,Rmax);
NCd4OH4 = zeros(number,Rmax);
NCdN1 = zeros(number,Rmax);
NCdN2 = zeros(number,Rmax);
NCdN3 = zeros(number,Rmax);
NCdN4 = zeros(number,Rmax);
NCdN5 = zeros(number,Rmax);
NCdChP = zeros(number,Rmax);
NCdChN = zeros(number,Rmax);
NCdNonCh = zeros(number,Rmax);

for j=1:Rmax
    Cn=Cn+0.02;  % Total N change step
    for i=1:number
        pH=step*(i-1);
        OH=10^-(14-pH);

        %solver
        x0 = 0;
        options = optimset('Display',
'off','NonlEqnAlgorithm','dogleg','LargeScale','off', 'MaxFunEvals',
5000, 'MaxIter', 500, 'TolFun', 1e-9, 'TolX', 1e-4);
        [S, fval, exitflag, output]
=fsolve(@nle_revisit_Cd,x0,options);      % S(1)-> NH3

        switch exitflag
            case 0
```

```
                disp('Number of iternation, evaluation exceeded');
            case -1
                disp('Algorithm terminated by output function');
            case -2
                disp('Algorithm appears to be converging a noon-root
point.');
            case -3
                disp('Trust radius became too small.');
            case -4
                disp('Line search error.');
        end

        %result
        Z(i,j) = (OH^-2)*(10^Kzox);  % [Zn2+]
        NH3(i,j) = S(1); % [NH3]
        ZOH1(i,j)=Z(i,j)*OH*10^Kzh1;          % [Zn(OH)+]
        ZOH2(i,j)=Z(i,j)*(OH)^2*10^Kzh2;     % [Zn(OH)2]
        ZOH3(i,j)=Z(i,j)*(OH)^3*10^Kzh3;      % [Zn(OH)3 -]
        ZOH4(i,j)=Z(i,j)*(OH)^4*10^Kzh4;      % [Zn(OH)4 2-]
        ZN1(i,j)=Z(i,j)*(NH3(i,j))*10^Kzn1;  % [Zn(NH3) 2+]
        ZN2(i,j)=Z(i,j)*(NH3(i,j))^2*10^Kzn2;     % [Zn(NH3)2 2+]
        ZN3(i,j)=Z(i,j)*(NH3(i,j))^3*10^Kzn3;    % [Zn(NH3)3 2+]
        ZN4(i,j)=Z(i,j)*(NH3(i,j))^4*10^Kzn4;    % [Zn(NH3)4 2+]

Ztot(i,j)=log10(Z(i,j)+ZOH1(i,j)+ZOH2(i,j)+ZOH3(i,j)+ZOH4(i,j)+ZN1(i,j)
+ZN2(i,j)+ZN3(i,j)+ZN4(i,j));

        NZ(i,j) = Z(i,j)/[10^Ztot(i,j)];
        NZOH1(i,j) = ZOH1(i,j)/[10^Ztot(i,j)];
        NZOH2(i,j) = ZOH2(i,j)/[10^Ztot(i,j)];
        NZOH3(i,j) = ZOH3(i,j)/[10^Ztot(i,j)];
        NZOH4(i,j) = ZOH4(i,j)/[10^Ztot(i,j)];
        NZN1(i,j) = ZN1(i,j)/[10^Ztot(i,j)];
        NZN2(i,j) = ZN2(i,j)/[10^Ztot(i,j)];
        NZN3(i,j) = ZN3(i,j)/[10^Ztot(i,j)];
        NZN4(i,j) = ZN4(i,j)/[10^Ztot(i,j)];
        NZChP(i,j) =
NZ(i,j)+NZOH1(i,j)+NZN1(i,j)+NZN2(i,j)+NZN3(i,j)+NZN4(i,j);
        NZChN(i,j) = NZOH3(i,j)+NZOH4(i,j);
        NZNonCh(i,j) = NZOH2(i,j);


        Cd(i,j) = (OH^-2)*(10^Kcdox);
        CdOH1(i,j)=Cd(i,j)*OH*10^Kcdh1;
        CdOH2(i,j)=Cd(i,j)*(OH)^2*10^Kcdh2;
        CdOH3(i,j)=Cd(i,j)*(OH)^3*10^Kcdh3;
        CdOH4(i,j)=Cd(i,j)*(OH)^4*10^Kcdh4;
        Cd2OH1(i,j)=(Cd(i,j)^2)*(OH)*10^Kcd2h1;
        Cd4OH4(i,j)=(Cd(i,j)^4)*(OH)^4*10^Kcd4h4;
        CdN1(i,j)=Cd(i,j)*(NH3(i,j))*10^Kcdn1;
        CdN2(i,j)=Cd(i,j)*(NH3(i,j))^2*10^Kcdn2;
        CdN3(i,j)=Cd(i,j)*(NH3(i,j))^3*10^Kcdn3;
        CdN4(i,j)=Cd(i,j)*(NH3(i,j))^4*10^Kcdn4;
        CdN5(i,j)=Cd(i,j)*(NH3(i,j))^5*10^Kcdn5;

Cdtot(i,j)=log10(Cd(i,j)+CdOH1(i,j)+CdOH2(i,j)+CdOH3(i,j)+CdOH4(i,j)+2*
```

```
Cd2OH1(i,j)+4*Cd4OH4(i,j)+CdN1(i,j)+CdN2(i,j)+CdN3(i,j)+CdN4(i,j)+CdN5(
i,j));

        NCd(i,j) = Cd(i,j)/[10^Cdtot(i,j)];
        NCdOH1(i,j) = CdOH1(i,j)/[10^Cdtot(i,j)];
        NCdOH2(i,j) = CdOH2(i,j)/[10^Cdtot(i,j)];
        NCdOH3(i,j) = CdOH3(i,j)/[10^Cdtot(i,j)];
        NCdOH4(i,j) = CdOH4(i,j)/[10^Cdtot(i,j)];
        NCd2OH1(i,j) = 2*Cd2OH1(i,j)/[10^Cdtot(i,j)];
        NCd4OH4(i,j) = 4*Cd4OH4(i,j)/[10^Cdtot(i,j)];
        NCdN1(i,j) = CdN1(i,j)/[10^Cdtot(i,j)];
        NCdN2(i,j) = CdN2(i,j)/[10^Cdtot(i,j)];
        NCdN3(i,j) = CdN3(i,j)/[10^Cdtot(i,j)];
        NCdN4(i,j) = CdN4(i,j)/[10^Cdtot(i,j)];
        NCdN5(i,j) = CdN5(i,j)/[10^Cdtot(i,j)];
        NCdChP(i,j) =
NCd(i,j)+NCdOH1(i,j)+NCdN1(i,j)+NCdN2(i,j)+NCdN3(i,j)+NCdN4(i,j)+NCd2OH
1(i,j)+NCd4OH4(i,j)+NCdN5(i,j);
        NCdChN(i,j) = NCdOH3(i,j)+NCdOH4(i,j);
        NCdNonCh(i,j) = NCdOH2(i,j);
    end


plot(k,NZ(:,j),k,NZOH1(:,j)',k,NZOH2(:,j)',k,NZOH3(:,j)',k,NZOH4(:,j)',
k,NZN1(:,j)',k,NZN2(:,j)',k,NZN3(:,j)',k,NZN4(:,j)');
    xlabel('pH')
    ylabel('Normailzed Zn ion complexes')
    title('Zn ion complexs distribution ')
    figure

    plot(k,NZChP(:,j),k,NZChN(:,j),k,NZNonCh(:,j)');
    xlabel('pH')
    ylabel('charge/non charge complexes')
    title('Zn ion complexs distribution ')
    figure


plot(k,NCd(:,j),k,NCdOH1(:,j)',k,NCdOH2(:,j)',k,NCdOH3(:,j)',k,NCdOH4(:
,j)',k,NCd2OH1(:,j)',k,NCd4OH4(:,j)',k,NCdN1(:,j)',k,NCdN2(:,j)',k,NCdN
3(:,j)',k,NCdN4(:,j)',k,NCdN5(:,j)');
    xlabel('pH')
    ylabel('Normailzed Cd ion complexes')
    title('Cd ion complexs distribution ')
    figure

    plot(k,NCdChP(:,j),k,NCdChN(:,j),k,NCdNonCh(:,j)');
    xlabel('pH')
    ylabel('charge/non charge complexes')
    title('Cd ion complexs distribution ')
    figure


end

for j=1:Rmax
```

```
    plot(k,Ztot(:,j))
    xlabel('pH')
    ylabel('Total [Zn],[Cd]')
    title('Zn(blue), Cd(red) solubility plot')
    hold on
end



for j=1:Rmax
    plot(k,Cdtot(:,j),'color',[1 0 0])
    xlabel('pH')
    ylabel('Total [Zn],[Cd]')
    title('Zn(blue), Cd(red) solubility plot')
    hold on
end
toc;

% Sub function code

function F=nle_revisit_Cd(x)
% x(1) : NH3
global OH Kzhn Cn Kzh1 Kzh2 Kzh3 Kzh4 Kzn1 Kzn2 Kzn3 Kzn4 Kzox Kcdh1
Kcdh2 Kcdh3 Kcdh4 Kcdn1 Kcdn2 Kcdn3 Kcdn4 Kcdn5 Kcdox

    Z=(OH^-2)*(10^Kzox);
    Cd=(OH^-2)*(10^Kcdox);

    %equations
    NH4=x(1)*(1/OH)*(10^-Kzhn);
    ZN1=Z*(x(1))*(10^Kzn1);
    ZN2=Z*((x(1))^2)*(10^Kzn2);
    ZN3=Z*((x(1))^3)*(10^Kzn3);
    ZN4=Z*((x(1))^4)*(10^Kzn4);
    CdN1=Cd*(x(1))*(10^Kcdn1);
    CdN2=Cd*((x(1))^2)*(10^Kcdn2);
    CdN3=Cd*((x(1))^3)*(10^Kcdn3);
    CdN4=Cd*((x(1))^4)*(10^Kcdn4);
    CdN5=Cd*((x(1))^5)*(10^Kcdn5);


F(1)=NH4+x(1)+ZN1+2*ZN2+3*ZN3+4*ZN4+CdN1+2*CdN2+3*CdN3+4*CdN4+5*CdN5-
Cn;      % Total NH3 to be setup
```

### 10.1.3. $ZnO/Al_2O_3$ mixed condition solubility plot code

```
% Main Code

clear;
close all
tic
```

```
global OH Kzhn Cn Kzh1 Kzh2 Kzh3 Kzh4 Kzn1 Kzn2 Kzn3 Kzn4 Kzox Kalh1
Kalh2 Kalh3 Kalh4 Kal2h2 Kal3h4 Kalox

%values definition
Kzh1=5.0;
Kzh2=11.1;
Kzh3=13.6;
Kzh4=14.8;
Kzn1=2.21;
Kzn2=4.5;
Kzn3=6.86;
Kzn4=8.89;
Kzox=-15.52;

Kalh1=9.01;
Kalh2=18.7;
Kalh3=27;
Kalh4=33;
Kal2h2=20.3;
Kal3h4=42.1;
Kalox=-33.5;

Kzhn=4.39;
number=100;
Cn=0;
Rmax=1; % Nitrogen concent change numbers
step=14/(number-1); %internal variable
k=0:step:step*(number-1);

% allocate storage space
NH3 = zeros(number,Rmax);

Z = zeros(number,Rmax);
ZOH1 = zeros(number,Rmax);
ZOH2 = zeros(number,Rmax);
ZOH3 = zeros(number,Rmax);
ZOH4 = zeros(number,Rmax);
ZN1 = zeros(number,Rmax);
ZN2 = zeros(number,Rmax);
ZN3 = zeros(number,Rmax);
ZN4 = zeros(number,Rmax);
Ztot = zeros(number,Rmax);

NZ = zeros(number,Rmax);
NZOH1 = zeros(number,Rmax);
NZOH2 = zeros(number,Rmax);
NZOH3 = zeros(number,Rmax);
NZOH4 = zeros(number,Rmax);
NZN1 = zeros(number,Rmax);
NZN2 = zeros(number,Rmax);
NZN3 = zeros(number,Rmax);
NZN4 = zeros(number,Rmax);
NZChP = zeros(number,Rmax);
NZChN = zeros(number,Rmax);
```

```
NZNonCh = zeros(number,Rmax);

Al = zeros(number,Rmax);
AlOH1 = zeros(number,Rmax);
AlOH2 = zeros(number,Rmax);
AlOH3 = zeros(number,Rmax);
AlOH4 = zeros(number,Rmax);
Al2OH2 = zeros(number,Rmax);
Al3OH4 = zeros(number,Rmax);
Altot = zeros(number,Rmax);

NAl = zeros(number,Rmax);
NAlOH1 = zeros(number,Rmax);
NAlOH2 = zeros(number,Rmax);
NAlOH3 = zeros(number,Rmax);
NAlOH4 = zeros(number,Rmax);
NAl2OH2 = zeros(number,Rmax);
NAl3OH4 = zeros(number,Rmax);
NAlChP = zeros(number,Rmax);
NAlChN = zeros(number,Rmax);
NAlNonCh = zeros(number,Rmax);


for j=1:Rmax
    Cn=Cn+0.3;  % Total N change step
    for i=1:number
        pH=step*(i-1);
        OH=10^-(14-pH);

        %solver
        x0 = 0;
        options = optimset('Display',
'off','NonlEqnAlgorithm','dogleg','LargeScale','off', 'MaxFunEvals',
5000, 'MaxIter', 500, 'TolFun', 1e-9, 'TolX', 1e-4);
        [S, fval, exitflag, output]
=fsolve(@nle_revisit_Al,x0,options);      % S(1)-> NH3

        switch exitflag
            case 0
                disp('Number of iternation, evaluation exceeded');
            case -1
                disp('Algorithm terminated by output function');
            case -2
                disp('Algorithm appears to be converging a noon-root
point.');
            case -3
                disp('Trust radius became too small.');
            case -4
                disp('Line search error.');
        end

        %result
        Z(i,j) = (OH^-2)*(10^Kzox);  % [Zn2+]
        NH3(i,j) = S(1); % [NH3]
        ZOH1(i,j)=Z(i,j)*OH*10^Kzh1;          % [Zn(OH)+]
```

```
        ZOH2(i,j)=Z(i,j)*(OH)^2*10^Kzh2;     % [Zn(OH)2]
        ZOH3(i,j)=Z(i,j)*(OH)^3*10^Kzh3;      % [Zn(OH)3 -]
        ZOH4(i,j)=Z(i,j)*(OH)^4*10^Kzh4;      % [Zn(OH)4 2-]
        ZN1(i,j)=Z(i,j)*(NH3(i,j))*10^Kzn1;  % [Zn(NH3) 2+]
        ZN2(i,j)=Z(i,j)*(NH3(i,j))^2*10^Kzn2;     % [Zn(NH3)2 2+]
        ZN3(i,j)=Z(i,j)*(NH3(i,j))^3*10^Kzn3;    % [Zn(NH3)3 2+]
        ZN4(i,j)=Z(i,j)*(NH3(i,j))^4*10^Kzn4;    % [Zn(NH3)4 2+]

Ztot(i,j)=log10(Z(i,j)+ZOH1(i,j)+ZOH2(i,j)+ZOH3(i,j)+ZOH4(i,j)+ZN1(i,j)
+ZN2(i,j)+ZN3(i,j)+ZN4(i,j));

        NZ(i,j) = Z(i,j)/[10^Ztot(i,j)];
        NZOH1(i,j) = ZOH1(i,j)/[10^Ztot(i,j)];
        NZOH2(i,j) = ZOH2(i,j)/[10^Ztot(i,j)];
        NZOH3(i,j) = ZOH3(i,j)/[10^Ztot(i,j)];
        NZOH4(i,j) = ZOH4(i,j)/[10^Ztot(i,j)];
        NZN1(i,j) = ZN1(i,j)/[10^Ztot(i,j)];
        NZN2(i,j) = ZN2(i,j)/[10^Ztot(i,j)];
        NZN3(i,j) = ZN3(i,j)/[10^Ztot(i,j)];
        NZN4(i,j) = ZN4(i,j)/[10^Ztot(i,j)];
        NZChP(i,j) =
NZ(i,j)+NZOH1(i,j)+NZN1(i,j)+NZN2(i,j)+NZN3(i,j)+NZN4(i,j);
        NZChN(i,j) = NZOH3(i,j)+NZOH4(i,j);
        NZNonCh(i,j) = NZOH2(i,j);

        Al(i,j) = (OH^-3)*(10^Kalox);  % [Al3+]
        AlOH1(i,j)=Al(i,j)*OH*10^Kalh1;          % [Al(OH)]
        AlOH2(i,j)=Al(i,j)*(OH^2)*10^Kalh2;          % [Al(OH)2]
        AlOH3(i,j)=Al(i,j)*(OH^3)*10^Kalh3;          % [Al(OH)3]
        AlOH4(i,j)=Al(i,j)*(OH^4)*10^Kalh4;          % [Al(OH)4]
        Al2OH2(i,j)=(Al(i,j)*OH)^2*10^Kal2h2;          % [Al2(OH)2]
        Al3OH4(i,j)=(Al(i,j))^3*(OH^4)^2*10^Kal3h4;          % [Al3(OH)4]

Altot(i,j)=log10(Al(i,j)+AlOH1(i,j)+AlOH2(i,j)+AlOH3(i,j)+AlOH4(i,j)+2*
Al2OH2(i,j)+3*Al3OH4(i,j));

        NAl(i,j) = Al(i,j)/[10^Altot(i,j)];
        NAlOH1(i,j) = AlOH1(i,j)/[10^Altot(i,j)];
        NAlOH2(i,j) = AlOH2(i,j)/[10^Altot(i,j)];
        NAlOH3(i,j) = AlOH3(i,j)/[10^Altot(i,j)];
        NAlOH4(i,j) = AlOH4(i,j)/[10^Altot(i,j)];
        NAl2OH2(i,j) = 2*Al2OH2(i,j)/[10^Altot(i,j)];
        NAl3OH4(i,j) = 3*Al3OH4(i,j)/[10^Altot(i,j)];
        NAlChP(i,j) =
NAl(i,j)+NAlOH1(i,j)+NAlOH2(i,j)+NAl2OH2(i,j)+NAl3OH4(i,j);
        NAlChN(i,j) = NAlOH4(i,j);
        NAlNonCh(i,j) = NAlOH3(i,j);

    end


plot(k,NZ(:,j),k,NZOH1(:,j)',k,NZOH2(:,j)',k,NZOH3(:,j)',k,NZOH4(:,j)',
k,NZN1(:,j)',k,NZN2(:,j)',k,NZN3(:,j)',k,NZN4(:,j)');
    xlabel('pH')
    ylabel('Normailzed Zn ion complexes')
    title('Zn ion complexs distribution ')
```

```
    figure

    plot(k,NZChP(:,j),k,NZChN(:,j),k,NZNonCh(:,j)');
    xlabel('pH')
    ylabel('charge/non charge complexes')
    title('Zn ion complexs distribution ')
    figure


plot(k,NAl(:,j),k,NAlOH1(:,j)',k,NAlOH2(:,j)',k,NAlOH3(:,j)',k,NAlOH4(:
,j)',k,NAl2OH2(:,j)',k,NAl3OH4(:,j)');
    xlabel('pH')
    ylabel('Normailzed Al ion complexes')
    title('Al ion complexs distribution ')
    figure

    plot(k,NAlChP(:,j),k,NAlChN(:,j),k,NAlNonCh(:,j)');
    xlabel('pH')
    ylabel('charge/non charge complexes')
    title('Al ion complexs distribution ')
    figure

end

for j=1:Rmax
    plot(k,Ztot(:,j))
    xlabel('pH')
    ylabel('Total [Zn],[Al]')
    title('Zn(blue), Al(red) solubility plot')
    hold on
end



for j=1:Rmax
    plot(k,Altot(:,j),'color',[1 0 0])
    xlabel('pH')
    ylabel('Total [Zn],[Al]')
    title('Zn(blue), Al(red) solubility plot')
    hold on
end
toc;


% Sub function code

function F=nle_revisit_Al(x)
% x(1) : NH3
global OH Kzhn Cn Kzh1 Kzh2 Kzh3 Kzh4 Kzn1 Kzn2 Kzn3 Kzn4 Kzox Kalh1
Kalh2 Kalh3 Kalh4 Kal2h2 Kal3h4 Kalox

    Z=(OH^-2)*(10^Kzox);
    Al=(OH^-3)*(10^Kalox);
```

```
    %equations
    NH4=x(1)*(1/OH)*(10^-Kzhn);
    ZN1=Z*(x(1))*(10^Kzn1);
    ZN2=Z*((x(1))^2)*(10^Kzn2);
    ZN3=Z*((x(1))^3)*(10^Kzn3);
    ZN4=Z*((x(1))^4)*(10^Kzn4);

    F(1)=NH4+x(1)+ZN1+2*ZN2+3*ZN3+4*ZN4-Cn;      % Total NH3 to be
setup
```

## 10.2. Chemical reaction constants used for calculations

| Chemical Reaction | Log K |
|---|---|
| **Ammonia** | |
| $NH_4^+ + OH^- \leftrightarrow NH_3 + H_2O$ | 4.39 |
| **Zn ion** | |
| $Zn^{2+} + OH^- \leftrightarrow Zn(OH)^+$ | 5.0 |
| $Zn^{2+} + 2OH^- \leftrightarrow Zn(OH)_2\ (aq)$ | 11.1 |
| $Zn^{2+} + 3OH^- \leftrightarrow Zn(OH)_3^-$ | 13.6 |
| $Zn^{2+} + 4OH^- \leftrightarrow Zn(OH)_4^{2-}$ | 14.8 |
| $Zn^{2+} + NH_3 \leftrightarrow Zn(NH_3)^{2+}$ | 2.21 |
| $Zn^{2+} + 2NH_3 \leftrightarrow Zn(NH_3)_2^{2+}$ | 4.5 |
| $Zn^{2+} + 3NH_3 \leftrightarrow Zn(NH_3)_3^{2+}$ | 6.86 |
| $Zn^{2+} + 4NH_3 \leftrightarrow Zn(NH_3)_4^{2+}$ | 8.89 |
| $Zn^{2+} + 2OH^- \leftrightarrow ZnO(s) + H_2O$ | 15.52 |
| **Al ion** | |
| $Al^{3+} + OH^- \leftrightarrow Al(OH)^{2+}$ | 9.01 |
| $Al^{3+} + 2OH^- \leftrightarrow Al(OH)_2^+$ | 18.7 |
| $Al^{3+} + 3OH^- \leftrightarrow Al(OH)_3\ (aq)$ | 27.0 |
| $Al^{3+} + 4OH^- \leftrightarrow Al(OH)_4^-$ | 33.0 |
| $2Al^{3+} + 2OH^- \leftrightarrow Al_2(OH)_2^{2+}$ | 20.3 |
| $3Al^{3+} + 4OH^- \leftrightarrow Al_3(OH)_4^{5+}$ | 42.1 |
| $Al^{3+} + 3OH^- \leftrightarrow Al(OH)_3\ (s)$ | 33.5 |
| **In ion** | |
| $In^{3+} + OH^- \leftrightarrow In(OH)^{2+}$ | 10 |
| $In^{3+} + 2OH^- \leftrightarrow In(OH)_2^+$ | 20.2 |
| $In^{3+} + 3OH^- \leftrightarrow In(OH)_3\ (aq)$ | 29.6 |
| $In^{3+} + 4OH^- \leftrightarrow In(OH)_4^-$ | 33.9 |
| $3In^{3+} + 4OH^- \leftrightarrow In_3(OH)_4^{5+}$ | 50.2 |
| $In^{3+} + 3OH^- \leftrightarrow In(OH)_3\ (s)$ | 36.9 |
| **Ga ion** | |
| $Ga^{3+} + OH^- \leftrightarrow Ga(OH)^{2+}$ | 11.4 |
| $Ga^{3+} + 2OH^- \leftrightarrow Ga(OH)_2^+$ | 22.1 |
| $Ga^{3+} + 3OH^- \leftrightarrow Ga(OH)_3\ (aq)$ | 31.7 |
| $Ga^{3+} + 4OH^- \leftrightarrow Ga(OH)_4^-$ | 39.4 |
| $Ga^{3+} + 3OH^- \leftrightarrow Ga(OH)_3\ (s)$ | 37 |
| **Sr ion** | |
| $Sr^{2+} + OH^- \leftrightarrow Sr(OH)^+$ | 0.8 |
| $Sr^{2+} + 2OH^- \leftrightarrow Sr(OH)_2\ (s)$ | 3.15 |

| Chemical Reaction | Log K |
|---|---|
| **Ca ion** | |
| $Ca^{2+} + OH^- \leftrightarrow Ca(OH)^+$ | 1.3 |
| $Ca^{2+} + NH_3 \leftrightarrow Zn(NH_3)^{2+}$ | -0.2 |
| $Ca^{2+} + 2NH_3 \leftrightarrow Zn(NH_3)_2^{2+}$ | -0.8 |
| $Ca^{2+} + 2OH^- \leftrightarrow Ca(OH)_2\ (s)$ | 5.19 |
| **Mg ion** | |
| $Mg^{2+} + OH^- \leftrightarrow Mg(OH)^+$ | 2.58 |
| $4Mg^{2+} + 4OH^- \leftrightarrow Mg_4(OH)_4^{4+}$ | 16.3 |
| $Mg^{2+} + NH_3 \leftrightarrow Mg(NH_3)^{2+}$ | 0.23 |
| $Mg^{2+} + 2NH_3 \leftrightarrow Mg(NH_3)_2^{2+}$ | 0.08 |
| $Mg^{2+} + 3NH_3 \leftrightarrow Mg(NH_3)_3^{2+}$ | -0.3 |
| $Mg^{2+} + 2OH^- \leftrightarrow Mg(OH)_2\ (s)$ | 11.15 |
| **Cu ion** | |
| $Cu^{2+} + OH^- \leftrightarrow Cu(OH)^+$ | 6.3 |
| $Cu^{2+} + 2OH^- \leftrightarrow Cu(OH)_2\ (aq)$ | 12.8 |
| $Cu^{2+} + 3OH^- \leftrightarrow Cu(OH)_3^-$ | 14.5 |
| $Cu^{2+} + 4OH^- \leftrightarrow Cu(OH)_4^{2-}$ | 15.6 |
| $2Cu^{2+} + 2OH^- \leftrightarrow Cu_2(OH)_2^{2+}$ | 17.7 |
| $Cu^{2+} + NH_3 \leftrightarrow Cu(NH_3)^{2+}$ | 4.04 |
| $Cu^{2+} + 2NH_3 \leftrightarrow Cu(NH_3)_2^{2+}$ | 7.47 |
| $Cu^{2+} + 3NH_3 \leftrightarrow Cu(NH_3)_3^{2+}$ | 10.27 |
| $Cu^{2+} + 4NH_3 \leftrightarrow Cu(NH_3)_4^{2+}$ | 11.75 |
| $Cu^{2+} + 5NH_3 \leftrightarrow Cu(NH_3)_5^{2+}$ | 12.43 |
| $Cu^{2+} + 2OH^- \leftrightarrow Cu(OH)_2\ (s)$ | 19.32 |
| **Cd ion** | |
| $Cd^{2+} + OH^- \leftrightarrow Cd(OH)^+$ | 4.1 |
| $Cd^{2+} + 2OH^- \leftrightarrow Cd(OH)_2\ (aq)$ | 7.7 |
| $Cd^{2+} + 3OH^- \leftrightarrow Cd(OH)_3^-$ | 10.3 |
| $Cd^{2+} + 4OH^- \leftrightarrow Cd(OH)_4^{2-}$ | 12.0 |
| $2Cd^{2+} + OH^- \leftrightarrow Cd_2(OH)^{3+}$ | 4.6 |
| $4Cd^{2+} + 4OH^- \leftrightarrow Cd_4(OH)_4^{4+}$ | 23.2 |
| $Cd^{2+} + NH_3 \leftrightarrow Cd(NH_3)^{2+}$ | 2.62 |
| $Cd^{2+} + 2NH_3 \leftrightarrow Cd(NH_3)_2^{2+}$ | 4.79 |
| $Cd^{2+} + 3NH_3 \leftrightarrow Cd(NH_3)_3^{2+}$ | 6.16 |
| $Cd^{2+} + 4NH_3 \leftrightarrow Cd(NH_3)_4^{2+}$ | 7.1 |
| $Cd^{2+} + 5NH_3 \leftrightarrow Cd(NH_3)_5^{2+}$ | 6.9 |
| $Cd^{2+} + 2OH^- \leftrightarrow Cd(OH)_2\ (s)$ | 14.29 |

# Bibliography


[1] L. Vayssieres, "Growth of arrayed nanorods and nanowires of ZnO from aqueous solutions," *Advanced Materials,* vol. 15, pp. 464-466, 2003.

[2] F. Lu, *et al.*, "Well-aligned zinc sulfide nanobelt arrays: Excellent field emitters," *Applied Physics Letters,* vol. 89, 2006.

[3] V. R. Shinde, *et al.*, "A Solution Chemistry Approach for the Selective Formation of Ultralong Nanowire Bundles of Crystalline $Cd(OH)_2$ on Substrates," *Advanced Materials,* vol. 20, pp. 1008-1012, 2008.

[4] Y. Li, *et al.*, "Nanowire electronic and optoelectronic devices," *Materials Today,* vol. 9, pp. 18-27, 2006.

[5] U. Ozgur, *et al.*, "A comprehensive review of ZnO materials and devices," *Journal of Applied Physics,* vol. 98, 2005.

[6] M. P. Julia, *et al.*, "Zinc-indium-oxide: A high conductivity transparent conducting oxide," *Applied Physics Letters,* vol. 67, pp. 2246-2248, 1995.

[7] L. Vayssieres, *et al.*, "Purpose-built anisotropic metal oxide material: 3D highly oriented microrod array of ZnO," *J. Phys. Chem. B,* vol. 105, pp. 3350-3352, 2001.

[8] C. J. Lee, *et al.*, "Field emission from well-aligned zinc oxide nanowires grown at low temperature," *Applied Physics Letters,* vol. 81, pp. 3648-3650, 2002.

[9] M. Law, *et al.*, "Nanowire dye-sensitized solar cells," *Nature Materials,* vol. 4, pp. 455-459, 2005.

[10] Z. L. Wang and J. Song, "Piezoelectric Nanogenerators Based on Zinc Oxide Nanowire Arrays," *Science,* vol. 312, pp. 242-246, April 14, 2006 2006.

[11] R. Konenkamp, *et al.*, "Vertical nanowire light-emitting diode," *Applied Physics Letters,* vol. 85, pp. 6004-6006, 2004.

[12] R. S. Wagner and W. C. Ellis, " Vapor-Liquid-Solid Mechanism of Single Crystal Growth," *Applied Physics Letters,* vol. 4, pp. 89-90, 1964.

[13] E. M. Chan, *et al.*, "Size-controlled growth of CdSe nanocrystals in microfluidic reactors," *Nano Letters,* vol. 3, pp. 199-201, 2003.

[14] E. M. Chan, *et al.*, "High-temperature microfluidic synthesis of CdSe nanocrystals in nanoliter droplets," *Journal of the American Chemical Society,* vol. 127, pp. 13854-13861, 2005.

[15] Y. J. Song, *et al.*, "Microfluidic synthesis of nanomaterials," *Small,* vol. 4, pp. 698-711, Jun 2008.

[16] S. A. Khan, *et al.*, "Microfluidic synthesis of colloidal silica," *Langmuir,* vol. 20, pp. 8604-8611, Sep 2004.

[17] D. Shalom, *et al.*, "Synthesis of thiol functionalized gold nanoparticles using a continuous flow microfluidic reactor," *Materials Letters,* vol. 61, pp. 1146-1150, Feb 2007.

[18] Y. J. Song, *et al.*, "Microfluidic synthesis of cobalt nanoparticles," *Chemistry of Materials,* vol. 18, pp. 2817-2827, Jun 2006.

[19] P. J. A. Kenis, *et al.*, "Microfabrication inside capillaries using multiphase laminar flow patterning," *Science,* vol. 285, pp. 83-85, Jul 1999.

[20] P. J. A. Kenis, *et al.*, "Fabrication inside microchannels using fluid flow,"

*Accounts of Chemical Research,* vol. 33, pp. 841-847, 2000.
[21] C. Klingshirn, "ZnO: From basics towards applications," *Physica Status Solidi B-Basic Solid State Physics,* vol. 244, pp. 3027-3073, 2007.
[22] K. M. Zhang, *et al.*, "Piezoelectricity of ZnO films prepared by sol-gel method," *Chinese Journal of Chemical Physics,* vol. 20, pp. 721-726, 2007.
[23] B. D. Yuhas and P. Yang, "Nanowire-Based All-Oxide Solar Cells," *Journal of the American Chemical Society,* vol. 131, pp. 3756-3761, 2009.
[24] Z. Zhang, *et al.*, "DNA immobilization and SAW response in ZnO nanotips grown on LiNbO3 substrates," *Ieee Transactions on Ultrasonics Ferroelectrics and Frequency Control,* vol. 53, pp. 786-792, 2006.
[25] L. Vayssieres, *et al.*, "Three-dimensional array of highly oriented crystalline ZnO microtubes," *Chem. Mater,* vol. 13, pp. 4395-4398, 2001.
[26] J. X. Wang, *et al.*, "Hydrothermally grown oriented ZnO nanorod arrays for gas sensing applications," *Nanotechnology,* vol. 17, p. 4995, 2006.
[27] M. Kreye, *et al.*, "Aqueous chemical growth and patterning of ZnO nanopillars on different substrate materials," *physica status solidi (c),* vol. 3, 2006.
[28] S. Yamabi and H. Imai, "Growth conditions for wurtzite zinc oxide films in aqueous solutions," *Journal of Materials Chemistry,* vol. 12, pp. 3773-3778, 2002.
[29] M. Liu, *et al.*, "Point defects and luminescence centres in zinc oxide and zinc oxide doped with manganese," *Journal of Luminescence,* vol. 54, pp. 35-42, 1992.
[30] L. E. Greene, *et al.*, "Low-temperature wafer-scale production of ZnO nanowire arrays," *Angewandte Chemie-International Edition,* vol. 42, pp. 3031-3034, 2003.
[31] M. J. Zheng, *et al.*, "Fabrication and optical properties of large-scale uniform zinc oxide nanowire arrays by one-step electrochemical deposition technique," *Chemical Physics Letters,* vol. 363, pp. 123-128, 2002.
[32] S. A. Studenikin, *et al.*, "Fabrication of green and orange photoluminescent, undoped ZnO films using spray pyrolysis," *Journal of Applied Physics,* vol. 84, pp. 2287-2294, 1998.
[33] K. Yu, *et al.*, "Shape alterations of ZnO nanocrystal arrays fabricated from NH3 center dot H2O solutions," *Applied Surface Science,* vol. 253, pp. 4072-4078, 2007.
[34] M. Wang, *et al.*, "Solvent-controlled crystallization of zinc oxide nano (micro)disks," *Journal of Crystal Growth,* vol. 310, pp. 1213-1219, 2008.
[35] Z. L. Wang, "Zinc oxide nanostructures: growth, properties and applications," *Journal of Physics Condensed Matter,* vol. 16, pp. 829-858, 2004.
[36] J. Goniakowski, *et al.*, "Polarity of oxide surfaces and nanostructures," *Reports on Progress in Physics,* vol. 71, 2008.
[37] R. Ferro, *et al.*, "Mixed $(ZnO)_x(CdO)_{1-X}$ policrystalline oxide films deposited by spray pyrolysis from metal nitrate solutions," *Journal of Materials Science Letters,* vol. 21, pp. 1939-1941, 2002.
[38] T. Ghoshal, *et al.*, "Synthesis of nano and micro crystals of $Cd(OH)_2$ and CdO in the shape of hexagonal sheets and rods," *Applied Surface Science,* vol. 253, pp. 7578-7584, 2007.
[39] W. Zaleszczyk, *et al.*, "Photoluminescence properties of ZnO and ZnCdO nanowires," *Acta Physica Polonica A,* vol. 112, pp. 357-362, 2007.

[40] Y. Z. Zhu, *et al.*, "Electronic structure and phase stability of MgO, ZnO, CdO, and related ternary alloys," *Physical Review B,* vol. 77, 2008.
[41] L. L. Chai, *et al.*, "Synthesis of wurtzite ZnS nanowire bundles using a solvothermal technique," *Journal of Physical Chemistry C,* vol. 111, pp. 12658-12662, 2007.
[42] J. Y. Lee, *et al.*, "Chemical conversion reaction between CdS nanobelts and ZnS nanobelts by vapor transport," *Chemistry of Materials,* vol. 19, pp. 4663-4669, 2007.
[43] S. L. Xiong, *et al.*, "A precursor-based route to ZnSe nanowire bundles," *Advanced Functional Materials,* vol. 15, pp. 1787-1792, 2005.
[44] G. H. Yue, *et al.*, "Hydrothermal synthesis of single-crystal ZnS nanowires," *Applied Physics a-Materials Science & Processing,* vol. 84, pp. 409-412, 2006.
[45] H. C. Hsu, *et al.*, "Band gap engineering and stimulated emission of ZnMgO nanowires," *Applied Physics Letters,* vol. 89, 2006.
[46] J. G. Lu, *et al.*, "Rational synthesis and tunable optical properties of quasialigned ZnMgO nanorods," *Applied Physics Letters,* vol. 91, p. 193108, 2007.
[47] V. F. Puntes, *et al.*, "Colloidal Nanocrystal Shape and Size Control: The Case of Cobalt," *Science,* vol. 291, pp. 2115-2117, March 16, 2001 2001.
[48] X. Peng, *et al.*, "Shape control of CdSe nanocrystals," *Nature,* vol. 404, pp. 59-61, 2000.
[49] X. Peng, "Mechanisms for the Shape-Control and Shape-Evolution of Colloidal Semiconductor Nanocrystals," *Advanced Materials,* vol. 15, pp. 459-463, 2003.
[50] S. P. Garcia and S. Semancik, "Controlling the morphology of zinc oxide nanorods crystallized from aqueous solutions: The effect of crystal growth modifiers on aspect ratio," *Chemistry of Materials,* vol. 19, pp. 4016-4022, 2007.
[51] M. Oner, *et al.*, "Control of ZnO crystallization by a PEO-b-PMAA diblock copolymer," *Chemistry of Materials,* vol. 10, pp. 460, 1998.
[52] L. E. Greene, *et al.*, "Solution-grown zinc oxide nanowires," *Inorganic Chemistry,* vol. 45, pp. 7535-7543, 2006.
[53] J. Zhang, *et al.*, "Control of ZnO morphology via a simple solution route," *Chemistry of Materials,* vol. 14, pp. 4172-4177, 2002.
[54] C. D. Bain, *et al.*, "Formation of monolayer films by the spontaneous assembly of organic thiols from solution onto gold," *Journal of the American Chemical Society,* vol. 111, pp. 321-335, 1989.
[55] M. Valtiner, *et al.*, "Stabilization and Acidic Dissolution Mechanism of Single-Crystalline ZnO(0001) Surfaces in Electrolytes Studied by In-Situ AFM Imaging and Ex-Situ LEED," *Langmuir,* vol. 24, pp. 5350-5358, 2008.
[56] J. W. Bullard and M. J. Cima, "Orientation dependence of the isoelectric point of TiO2 (rutile) surfaces," *Langmuir,* vol. 22, pp. 10264-10271, 2006.
[57] N. Kallay and T. Preocanin, "Measurement of the surface potential of individual crystal planes of hematite," *Journal of Colloid and Interface Science,* vol. 318, pp. 290-295, Feb 2008.
[58] R. J. Kershner, *et al.*, "Zeta potential orientation dependence of sapphire substrates," *Langmuir,* vol. 20, pp. 4101-4108, May 2004.
[59] R. Schweiss, *et al.*, "Dissociation of Surface Functional Groups and Preferential Adsorption of Ions on Self-Assembled Monolayers Assessed by Streaming

Potential and Streaming Current Measurements," *Langmuir,* vol. 17, pp. 4304-4311, 2001.
[60] *http://www.ifm.liu.se/applphys/ftir/samsfig2.jpg*
[61] D. Pradhan, *et al.*, "Fabrication of ZnO Nanospikes and Nanopillars on ITO Glass by Templateless Seed-Layer-Free Electrodeposition and Their Field-Emission Properties," *ACS Applied Materials & Interfaces,* vol. 1, pp. 789-796, 2009.
[62] W.-J. Li, *et al.*, "Growth mechanism and growth habit of oxide crystals," *Journal of Crystal Growth,* vol. 203, pp. 186-196, 1999.
[63] Z. Zhang and J. Mu, "Hydrothermal synthesis of ZnO nanobundles controlled by PEO-PPO-PEO block copolymers," *Journal of Colloid and Interface Science,* vol. 307, pp. 79-82, 2007.
[64] T. Song, *et al.*, "Surface Polarity and Shape-Controlled Synthesis of ZnO Nanostructures on GaN Thin Films Based on Catalyst-Free Metalorganic Vapor Phase Epitaxy," *Advanced Materials,* vol. 20, pp. 4464-4469, Dec 2008.
[65] G. Mu, *et al.*, "Tilted Epitaxial ZnO Nanospears on Si(001) by Chemical Bath Deposition," *Chemistry of Materials,* vol. 21, pp. 3960-3964, 2009.
[66] Z. Wang, *et al.*, "Aqueous solution fabrication of large-scale arrayed obelisk-like zinc oxide nanorods with high efficiency," *Journal of Solid State Chemistry,* vol. 177, pp. 2144-2149, 2004.
[67] P. Li, *et al.*, "Controllable growth of ZnO nanowhiskers by a simple solution route," *Materials Chemistry and Physics,* vol. 112, pp. 393-397, 2008.
[68] P. Li, *et al.*, "A simple low-temperature growth of ZnO nanowhiskers directly from aqueous solution containing Zn(OH)42- ions," *Chemical Communications,* pp. 2856-2857, 2004.
[69] R. A. LAUDISE, *et al.*, "Hydrothermal Growth of Large Sound Crystals of Zinc Oxide," *Journal of the American Ceramic Society,* vol. 47, pp. 9-12, 1964.
[70] S. Xu, *et al.*, "Patterned Growth of Vertically Aligned ZnO Nanowire Arrays on Inorganic Substrates at Low Temperature without Catalyst," *Journal of the American Chemical Society,* vol. 130, pp. 14958-14959, 2008.
[71] A. Knoll, *et al.*, "Phase Behavior in Thin Films of Cylinder-Forming Block Copolymers," *Physical Review Letters,* vol. 89, p. 035501, 2002.
[72] M. D. James D. Plummer, Peter B. Griffin., *Silicon VLSI technology : fundamentals, practice and modeling* Upper Saddle River, NJ : Prentice Hall, c2000., 2000.
[73] W. Li, *et al.*, "EXAFS studies on adsorption irreversibility of Zn(II) on TiO2: Temperature dependence," *Journal of Colloid and Interface Science,* vol. 319, pp. 385-391, Mar 2008.
[74] C. J. Easley, *et al.*, "Quantitative measurement of zinc secretion from pancreatic islets with high temporal resolution using droplet-based microfluidics," *Anal Chem,* vol. 81, pp. 9086-95, 2009 Nov 2009.
[75] R. H. Fowler and L. Nordheim, "Electron Emission in Intense Electric Fields," *Proceedings of the Royal Society of London. Series A, Containing Papers of a Mathematical and Physical Character,* vol. 119, pp. 173-181, 1928.
[76] *http://spie.org/x8847.xml?highlight=x2400&ArticleID=x8847*
[77] *http://groups.csail.mit.edu/graphics/classes/6.837/F01/Lecture01/Slide20.html*
[78] J. Y. Huang, *et al.*, "Giant field enhancement at carbon nanotube tips induced by

multistage effect," *Applied Physics Letters,* vol. 87, 2005.
[79] C. A. Spindt, *et al.*, "Physical properties of thin-film field emission cathodes with molybdenum cones," *Journal of Applied Physics,* vol. 47, pp. 5248-5263, 1976.
[80] W. B. Choi, *et al.*, "Fully sealed, high-brightness carbon-nanotube field-emission display," *Applied Physics Letters,* vol. 75, pp. 3129-3131, 1999.
[81] X. Fang, *et al.*, "Inorganic semiconductor nanostructures and their field-emission applications," *Journal of Materials Chemistry,* vol. 18, pp. 509-522, 2008.
[82] Y. W. Zhu, *et al.*, "Efficient field emission from ZnO nanoneedle arrays," *Applied Physics Letters,* vol. 83, pp. 144-146, 2003.
[83] Z. H. Chen, *et al.*, "ZnO nanowire arrays grown on Al:ZnO buffer layers and their enhanced electron field emission," *Journal of Applied Physics,* vol. 106, Sep 2009.
[84] Y. K. Tseng, *et al.*, "Characterization and field-emission properties of needle-like zinc oxide nanowires grown vertically on conductive zinc oxide films," *Advanced Functional Materials,* vol. 13, pp. 811-814, Oct 2003.
[85] Y. H. Yang, *et al.*, "Field emission of one-dimensional micro- and nanostructures of zinc oxide," *Applied Physics Letters,* vol. 89, Jul 2006.
[86] C. A. Aguilar, *et al.*, "Probing Electronic Properties of Molecular Engineered Zinc Oxide Nanowires with Photoelectron Spectroscopy," *Acs Nano,* vol. 3, pp. 3057-3062, 2009.
[87] K. Besocke, *et al.*, "Dipole moments associated with edge atoms; A comparative study on stepped Pt, Au and W surfaces," *Surface Science,* vol. 68, pp. 39-46, 1977.
[88] S. Chhoker, *et al.*, *Field emission properties of carbon nanostructures: A review.* New York: Ieee, 2007.
[89] S. H. Jo, *et al.*, "Field emission of carbon nanotubes grown on carbon cloth," *Journal of Vacuum Science & Technology B: Microelectronics and Nanometer Structures,* vol. 23, pp. 2363-2368, 2005.
[90] J. Bae, *et al.*, "Superior field emission properties of ZnO nanocones synthesized by pulsed laser deposition," *Chemical Physics Letters,* vol. 475, pp. 260-263, 2009.
[91] D. Banerjee, *et al.*, "Enhanced Field Emission of ZnO Nanowires," *Advanced Materials,* vol. 16, pp. 2028-2032, 2004.
[92] S. H. Jo, *et al.*, "Field emission of carbon nanotubes grown on carbon cloth," *Applied Physics Letters,* vol. 85, pp. 810-812, 2004.
[93] Q. H. Wang, *et al.*, "Field emission from nanotube bundle emitters at low fields," *Applied Physics Letters,* vol. 70, pp. 3308-3310, 1997.
[94] Y. J. Chen, *et al.*, "Field-emission from long SnO[sub 2] nanobelt arrays," *Applied Physics Letters,* vol. 85, pp. 5682-5684, 2004.
[95] H. Y. Yang and et al., "Field emission from zinc oxide nanoneedles on plastic substrates," *Nanotechnology,* vol. 16, p. 1300, 2005.
[96] Y. B. Tang, *et al.*, "Field emission from AlN nanorod array," *Applied Physics Letters,* vol. 86, p. 153104, 2005.
[97] G. Z. Yue, *et al.*, "Generation of continuous and pulsed diagnostic imaging x-ray radiation using a carbon-nanotube-based field-emission cathode," *Applied Physics Letters,* vol. 81, pp. 355-357, 2002.

[98] H. Sugie, *et al.*, "Carbon nanotubes as electron source in an x-ray tube," *Applied Physics Letters,* vol. 78, pp. 2578-2580, Apr 2001.
[99] E. Kratschmer, *et al.*, "An electron-beam microcolumn with improved resolution, beam current, and stability," *Journal of Vacuum Science & Technology B,* vol. 13, pp. 2498-2503, Nov-Dec 1995.
[100] J. Y. Park, *et al.*, "Characterization of two by two electron-beam microcolumn array aligned with field emission array," *Journal of Vacuum Science & Technology B,* vol. 16, pp. 826-828, Mar-Apr 1998.
[101] *http://www.planarembedded.com/electroluminescent-display/electroluminescent-glass/*
[102] R. H. Bube, "Electronic Transitions in the Luminescence of Zinc Sulfide Phosphors," *Physical Review,* vol. 90, p. 70, 1953.
[103] H. Sasakura, *et al.*, "The dependences of electroluminescent characteristics of ZnS:Mn thin films upon their device parameters," *Journal of Applied Physics,* vol. 52, pp. 6901-6906, 1981.
[104] J. Hurd and C. King, "Physical and electrical characterization of co-deposited Zns:Mn electroluminescent thin film structures," *Journal of Electronic Materials,* vol. 8, pp. 879-891, 1979.
[105] A. J. Warren, *et al.*, "The effect of Mn concentration on the photoluminescence of ZnS: Mn," *Journal of Physics D: Applied Physics,* vol. 16, pp. 225-232, 1983.
[106] D. Theis, "Selected Analytical Tools Yield a Better Insight into Electroluminescent Thin Films)," *physica status solidi (a),* vol. 81, pp. 647-655, 1984.
[107] J. Tauc, *Amorphous and Liquid Semiconductor*: Plenum press, New York, 1974.
[108] S. M. Sze, *Physics of Semiconductor Devices*: John Wiley, 1969.
[109] A. Ubale, *et al.*, "Size dependent optical characteristics of chemically deposited nanostructured ZnS thin films," *Bulletin of Materials Science,* vol. 30, pp. 147-151, 2007.
[110] R. Maity and K. K. Chattopadhyay, "Synthesis and optical characterization of ZnS and ZnS:Mn nanocrystalline thin films by chemical route," *Nanotechnology,* vol. 15, p. 812, 2004.
[111] A. N. Krasnov, "Selection of dielectrics for alternating-current thin-film electroluminescent device," *Thin Solid Films,* vol. 347, pp. 1-13, Jun 1999.
[112] P. H. Fang and W. S. Brower, "Temperature Dependence of the Breakdown Field of Barium Titanate," *Physical Review,* vol. 113, p. 456, 1959.
[113] M. Wang, *et al.*, "Field-enhancement factor for carbon nanotube array," *Journal of Applied Physics,* vol. 98, p. 014315, 2005.
[114] X. Q. Wang, *et al.*, "Modeling and calculation of field emission enhancement factor for carbon nanotubes array," *Ultramicroscopy,* vol. 102, pp. 181-187, 2005.
[115] F. H. Read and N. J. Bowring, "Field enhancement factors of random arrays of carbon nanotubes," *Nuclear Instruments and Methods in Physics Research Section A: Accelerators, Spectrometers, Detectors and Associated Equipment,* vol. 519, pp. 305-314, 2004.
[116] J. S. Suh, *et al.*, "Study of the field-screening effect of highly ordered carbon nanotube arrays," *Applied Physics Letters,* vol. 80, pp. 2392-2394, 2002.
[117] T. Minami, *et al.*, "High-luminance thin-film electroluminescent devices using

((Y2O3)(0.6)-(GeO2)(0.4)): Mn phosphors," *Japanese Journal of Applied Physics Part 2-Letters,* vol. 41, pp. L577-L579, May 2002.
[118] T. Minami, *et al.*, "High-luminance multicolor-emitting thin-film electroluminescent devices using (Y2O3-Ga2O3): Mn phosphors," *Japanese Journal of Applied Physics Part 2-Letters,* vol. 42, pp. L1018-L1020, Aug 2003.
[119] T. R. N. Kutty, "Effect of deposition conditions on the aging of a.c. thin film electroluminescent devices," *Thin Solid Films,* vol. 127, pp. 223-232, 1985.
[120] H. Nanto, *et al.*, " Low-voltage-driven ZnS-Mn thin film electroluminescent devices using insulating dielectric ceramic sheets," *Thin Solid Films,* vol. 164, pp. 363-367, Oct 1988.
[121] *http://worldoflcd.com/backlight_units_ccfl_tubes.htm*
[122] Y. C. Kim and E. H. Yoo, "Printed carbon nanotube field emitters for backlight applications," *Japanese Journal of Applied Physics Part 2-Letters & Express Letters,* vol. 44, pp. L454-L456, 2005.
[123] *http://www.cree.com/*
[124] S. Reineke, *et al.*, "White organic light-emitting diodes with fluorescent tube efficiency," *Nature,* vol. 459, pp. 234-U116, May 2009.
[125] P. L. Chen, *et al.*, "Fairly pure ultraviolet electroluminescence from ZnO-based light-emitting devices," *Applied Physics Letters,* vol. 89, 2006.
[126] J. M. Bian, *et al.*, "Properties of undoped n-type ZnO film and N-In codoped p-type ZnO film deposited by ultrasonic spray pyrolysis," *Chemical Physics Letters,* vol. 393, pp. 256-259, 2004.
[127] J. G. Lu, *et al.*, "Roles of hydrogen and nitrogen in p-type doping of ZnO," *Chemical Physics Letters,* vol. 441, pp. 68-71, 2007.
[128] C. H. Park, *et al.*, "Origin of p-type doping difficulty in ZnO: The impurity perspective," *Physical Review B,* vol. 66, 2002.
[129] Y. R. Ryu, *et al.*, "Fabrication of homostructural ZnO p-n junctions and ohmic contacts to arsenic-doped p-type ZnO," *Applied Physics Letters,* vol. 83, pp. 4032-4034, 2003.
[130] S. Shet, *et al.*, "Carrier concentration tuning of bandgap-reduced p-type ZnO films by codoping of Cu and Ga for improving photoelectrochemical response," *Journal of Applied Physics,* vol. 103, 2008.
[131] A. Tsukazaki, *et al.*, "Repeated temperature modulation epitaxy for p-type doping and light-emitting diode based on ZnO," *Nature Materials,* vol. 4, pp. 42-46, 2005.
[132] Y. I. Alivov, *et al.*, "Fabrication and characterization of n-ZnO/p-AlGaN heterojunction light-emitting diodes on 6H-SiC substrates," *Applied Physics Letters,* vol. 83, pp. 4719-4721, 2003.
[133] Y. I. Alivov, *et al.*, "Observation of 430 nm electroluminescence from ZnO/GaN heterojunction light-emitting diodes," *Applied Physics Letters,* vol. 83, p. 2943, 2003.
[134] M. C. Jeong, *et al.*, "ZnO-Nanowire-Inserted GaN/ZnO heterojunction light-emitting diodes," *Small,* vol. 3, pp. 568-572, 2007.
[135] M. C. Jeong, *et al.*, "Electroluminescence from ZnO nanowires in n-ZnO film/ZnO nanowire array/p-GaN film heterojunction light-emitting diodes," *Applied Physics Letters,* vol. 88, 2006.

[136] W. I. Park and G. C. Yi, "Electroluminescence in n-ZnO nanorod arrays vertically grown on p-GaN," *Advanced Materials,* vol. 16, pp. 87, 2004.
[137] A. C. Siegel, *et al.*, "Microsolidics: Fabrication of Three-Dimensional Metallic Microstructures in Poly(dimethylsiloxane)," *Advanced Materials,* vol. 19, pp. 727-733, 2007.
[138] L. Zhao, *et al.*, "A new approach to white light emitting diodes of p-GaN/i-ZnO/n-ZnO heterojunctions," *Applied Physics B-Lasers and Optics,* vol. 92, pp. 185-188, 2008.
[139] G. T. Du, *et al.*, "Room temperature defect related electroluminescence from ZnO homojunctions grown by ultrasonic spray pyrolysis," *Applied Physics Letters,* vol. 89, p. 052113, 2006.
[140] T. C. Chen, *et al.*, "Light emission from Al/$HfO_2$/silicon diodes," *Journal of Applied Physics,* vol. 95, pp. 6486-6488, 2004.
[141] B. Tian, *et al.*, "Coaxial silicon nanowires as solar cells and nanoelectronic power sources," *Nature,* vol. 449, pp. 885-889, 2007.
[142] B. M. Kayes, *et al.*, "Comparison of the device physics principles of planar and radial p-n junction nanorod solar cells," *Journal of Applied Physics,* vol. 97, p. 114302, 2005.
[143] A. Nadarajah, *et al.*, "Flexible inorganic nanowire light-emitting diode," *Nano Letters,* vol. 8, pp. 534-537, 2008.
[144] M. Izaki, *et al.*, "Electrochemically constructed p-$Cu_2O$/n-ZnO heterojunction diode for photovoltaic device," *Journal of Physics D-Applied Physics,* vol. 40, pp. 3326-3329, Jun 2007.
[145] S. Ishizuka, *et al.*, *Polycrystalline n-ZnO/p-$CU_2O$ heterojunctions grown by RF-magnetron sputtering*. New York: Wiley-Vch, Inc, 2004.
[146] J. Cui and U. J. Gibson, "A Simple Two-Step Electrodeposition of $Cu_2O$/ZnO Nanopillar Solar Cells," *The Journal of Physical Chemistry C,* 2010.
[147] A. E. Rakhshani, "Preparation, characteristics and photovoltaic properties of cuprous oxide - a reviw," *Solid-State Electronics,* vol. 29, pp. 7-17, Jan 1986.
[148] C. Y. Ting, *et al.*, "Study of planarized sputter-deposited $SiO_2$," *Journal of Vacuum Science and Technology,* vol. 15, pp. 1105-1112, 1978.
[149] S. Kawakami, *et al.*, "Mechanism of shape formation of three-dimensional periodic nanostructures by bias sputtering," *Applied Physics Letters,* vol. 74, pp. 463-465, 1999.
[150] K. Akiba, *et al.*, "Fabrication of silica-based optical waveguides with smooth side walls by RF-bias sputtering," *Electronics and Communications in Japan (Part II: Electronics),* vol. 78, pp. 31-39, 1995.
[151] H. Tanaka, *et al.*, "Effect of AZO film deposition conditions on the photovoltaic properties of AZO-$Cu_2O$ heterojunctions," *Applied Surface Science,* vol. 244, pp. 568-572, 2005.
[152] A. I. Hochbaum and P. D. Yang, "Semiconductor Nanowires for Energy Conversion," *Chemical Reviews,* vol. 110, pp. 527-546, Jan 2010.
[153] B. Gross, in *Electrets*. vol. 33, G. M. Sessler, Ed., ed New York, NY: Springer-Verlag, 1980, pp. 230-252.
[154] L. Reimer, *et al.*, "Charging of Bulk Specimens, Insulating Layers and Free-Supporting Films in Scanning Electron-Microscopy," *Optik,* vol. 92, pp. 14-22,

Nov 1992.
[155] L. Reimer, *Image formation in low-voltage scanning electron microscopy.* Bellingham, Wash., USA: SPIE Optical Engineering Press, 1993.
[156] D. C. Joy and C. S. Joy, "Low voltage scanning electron microscopy," *Micron,* vol. 27, pp. 247-263, Jun-Aug 1996.
[157] C. K. Ong, *et al.*, "Dynamics aspects of the charging behaviour of polymers under focused electron beam irradiation," *Journal of Physics: Condensed Matter,* vol. 9, p. 9289, 1997.
[158] K. M. Satyalakshmi, *et al.*, "Charge induced pattern distortion in low energy electron beam lithography," *Journal of Vacuum Science & Technology B,* vol. 18, pp. 3122-3125, Nov-Dec 2000.
[159] K. D. Cummings, "A Study of Deposited Charge from Electron-Beam Lithography," *Journal of Vacuum Science & Technology B,* vol. 8, pp. 1786-1788, Nov-Dec 1990.
[160] H. Itoh, *et al.*, "Investigation of the Charging Effect on Thin Sio2 Layers with the Electron-Beam Lithography System," *Journal of Vacuum Science & Technology B,* vol. 7, pp. 1532-1535, Nov-Dec 1989.
[161] W. Liu, *et al.*, "Resist Charging in Electron-Beam Lithography," *Journal of Vacuum Science & Technology B,* vol. 13, pp. 1979-1983, Sep-Oct 1995.
[162] M. Bai, *et al.*, "Charging and discharging of electron beam resist films," *Journal of Vacuum Science & Technology B,* vol. 17, pp. 2893-2896, Nov-Dec 1999.
[163] D. R. S. Cumming, *et al.*, "Efficient diffractive optics made by single-step electron beam lithography in solid PMMA," *Journal of Vacuum Science & Technology B,* vol. 15, pp. 2859-2863, Nov-Dec 1997.
[164] R. Steingruber, *et al.*, "Micro-optical elements fabricated by electron-beam lithography and dry etching technique using top conductive coatings," *Microelectronic Engineering,* vol. 57-8, pp. 285-289, Sep 2001.
[165] E. A. Dobisz, *et al.*, "Electroless metal discharge layers for electron beam lithography," *Applied Physics Letters,* vol. 82, pp. 478-480, Jan 2003.
[166] M. Angelopoulos, *et al.*, "Conducting Polyanilines - Discharge Layers for Electron-Beam Lithography," *Journal of Vacuum Science & Technology B,* vol. 7, pp. 1519-1523, Nov-Dec 1989.
[167] M. Angelopoulos, "Conducting polymers in microelectronics," *IBM Journal of Research and Development,* vol. 45, pp. 57-75, Jan 2001.
[168] M. A. Z. Hupcey and C. K. Ober, "Copolymer approach to charge-dissipating electron-beam resists," *Journal of Vacuum Science & Technology B,* vol. 16, pp. 3701-3704, Nov-Dec 1998.
[169] B. D. Myers and V. P. Dravid, "Variable Pressure Electron Beam Lithography (VP-eBL): A New Tool for Direct Patterning of Nanometer-Scale Features on Substrates with Low Electrical Conductivity," *Nano Letters,* vol. 6, pp. 963-968, May 10, 2006 2006.
[170] G. D. Danilatos, "Foundations of Environmental Scanning Electron-Microscopy," *Advances in Electronics and Electron Physics,* vol. 71, pp. 109-250, 1988.
[171] M. Toth, *et al.*, "Electron imaging of dielectrics under simultaneous electron-ion irradiation," *Journal of Applied Physics,* vol. 91, pp. 4479-4491, Apr 2002.
[172] R. Durkin and J. S. Shah, "Amplification and Noise in High-Pressure Scanning

Electron-Microscopy," *Journal of Microscopy-Oxford,* vol. 169, pp. 33-51, Jan 1993.
[173] B. L. Thiel and M. Toth, "Secondary electron contrast in low-vacuum/environmental scanning electron microscopy of dielectrics," *Journal of Applied Physics,* vol. 97, Mar 2005.
[174] J. Joo, *et al.*, "Nanoscale patterning on insulating substrates by critical energy electron beam lithography," *Nano Letters,* vol. 6, pp. 2021-2025, Sep 2006.
[175] J. W. Lussi, *et al.*, "Selective molecular assembly patterning at the nanoscale: a novel platform for producing protein patterns by electron-beam lithography on SiO2/indium tin oxide-coated glass substrates," *Nanotechnology,* vol. 16, pp. 1781-1786, Sep 2005.
[176] J. Joo, *et al.*, "Simple fabrication of UV nanoimprint templates using critical energy electron beam lithography," *Journal of Vacuum Science & Technology B,* vol. 25, pp. 2407-2411, Nov 2007.
[177] P. Avouris, *et al.*, "Carbon nanotube electronics," *Proceedings of the IEEE,* vol. 91, pp. 1772-1784, Nov 2003.
[178] Y. Cui and C. M. Lieber, "Functional nanoscale electronic devices assembled using silicon nanowire building blocks," *Science,* vol. 291, pp. 851-853, Feb 2001.
[179] A. N. Shipway, *et al.*, "Nanoparticle arrays on surfaces for electronic, optical, and sensor applications," *Chemphyschem,* vol. 1, pp. 18-52, Aug 2000.
[180] D. J. Norris and Y. A. Vlasov, "Chemical approaches to three-dimensional semiconductor photonic crystals," *Advanced Materials,* vol. 13, pp. 371-376, Mar 2001.
[181] E. Braun, *et al.*, "DNA-templated assembly and electrode attachment of a conducting silver wire," *Nature,* vol. 391, pp. 775-778, Feb 1998.
[182] C. A. Mirkin, *et al.*, "A DNA-based method for rationally assembling nanoparticles into macroscopic materials," *Nature,* vol. 382, pp. 607-609, Aug 1996.
[183] C. R. Barry, *et al.*, "Charging process and coulomb-force-directed printing of nanoparticles with sub-100-nm lateral resolution," *Nano Letters,* vol. 5, pp. 2078-2084, Oct 2005.
[184] C. R. Barry, *et al.*, "Printing nanoparticle building blocks from the gas phase using nanoxerography," *Applied Physics Letters,* vol. 83, pp. 5527-5529, Dec 2003.
[185] H. Fudouzi, *et al.*, "An arrangement of micrometer-sized powder particles by electron beam drawing," *Advanced Powder Technology,* vol. 8, pp. 251-262, 1997.
[186] H. Fudouzi, *et al.*, "Assembling 100 mn scale particles by an electrostatic potential field," *Journal of Nanoparticle Research,* vol. 3, pp. 193-200, Jun 2001.
[187] H. Fudouzi, *et al.*, "Site-controlled deposition of microsized particles using an electrostatic assembly," *Advanced Materials,* vol. 14, pp. 1649-1652, Nov 2002.
[188] H. O. Jacobs, *et al.*, "Approaching nanoxerography: The use of electrostatic forces to position nanoparticles with 100 nm scale resolution," *Advanced Materials,* vol. 14, pp. 1553-1557, Nov 2002.
[189] H. O. Jacobs and G. M. Whitesides, "Submicrometer patterning of charge in thin-

film electrets," *Science,* vol. 291, pp. 1763-1766, Mar 2001.
[190] M. Kobayashi, *et al.*, "Assemblage of particles for intelligent materials," *Smart Materials & Structures,* vol. 7, pp. 496-501, Aug 1998.
[191] H. O. Jacobs and A. Stemmer, "Measuring and modifying the electric surface potential distribution on a nanometre scale: A powerful tool in science and technology," *Surface and Interface Analysis,* vol. 27, pp. 361-367, May-Jun 1999.
[192] H. Fudouzi, *et al.*, "Formation of electrified images using electron and ion beams," *Journal of Electrostatics,* vol. 42, pp. 43-49, Oct 1997.
[193] L. Reimer, *Scanning electron microscopy : physics of image formation and microanalysis*. Berlin ; New York: Springer-Verlag, 1985.
[194] J. H. Butler, *et al.*, "Low-Voltage Scanning Electron-Microscopy of Polymers," *Polymer,* vol. 36, pp. 1781-1790, Apr 1995.
[195] J. B. Fenn, *et al.*, "Electrospray Ionization-Principles and Practice," *Mass Spectrometry Reviews,* vol. 9, pp. 37-70, Jan 1990.
[196] P. Kebarle and L. Tang, "From Ions in Solution to Ions in the Gas-Phase - the Mechanism of Electrospray Mass-Spectrometry," *Analytical Chemistry,* vol. 65, pp. A972-A986, Nov 1993.
[197] J. Joo, *et al.*, "Ultrafast patterning of nanoparticles by electrostatic lithography," *Journal of Vacuum Science & Technology B,* vol. 24, pp. 3205-3208, Nov-Dec 2006.
[198] D. C. Joy and C. S. Joy, "Study of the dependence of $E_2$ energies on sample chemistry," *Microscopy and Microanalysis,* vol. 4, pp. 475-480, Sep-Oct 1998.
[199] *http://www.revolttechnology.com/*